Collisional Cascade Caclulations for Irregular Satellite Swarms in Fomalhaut b

Scott J. Kenyon

Smithsonian Astrophysical Observatory, 60 Garden Street, Cambridge, MA 02138

e-mail: skenyon@cfa.harvard.edu

Benjamin C. Bromley

Department of Physics & Astronomy, University of Utah, 201 JFB, Salt Lake City, UT 84112

e-mail: bromley@physics.utah.edu

ABSTRACT

We describe an extensive suite of numerical calculations for the collisional evolution of irregular satellite swarms around 1–300 $M_\oplus$ planets orbiting at 120 AU in the Fomalhaut system. For 10–100 $M_\oplus$ planets, swarms with initial masses of roughly 1% of the planet mass have cross-sectional areas comparable to the observed cross-sectional area of Fomalhaut b. Among 30–300 $M_\oplus$ planets, our calculations yield optically thick swarms of satellites for ages of 1–10 Myr. Observations with HST and ground-based AO instruments can constrain the frequency of these systems around stars in the β Pic moving group and possibly other nearby associations of young stars.

Subject headings: planetary systems – planets and satellites: formation – protoplanetary disks – stars: formation – zodiacal dust – circumstellar matter

1. INTRODUCTION

Fomalhaut b is a planet candidate on an eccentric orbit at a distance of ~ 120 AU from the A-type star Fomalhaut (e.g., Kalas et al. 2008; Currie et al. 2012; Galicher et al. 2013; Kalas et al. 2013; Beust et al. 2014). The optical colors and lack of detections beyond 1 μm suggest emission from a cloud of dust instead of a planetary photosphere (e.g., Marengo et al. 2009; Janson et al. 2012; Currie et al. 2012; Kalas et al. 2013; Janson et al. 2015). The observed level of optical emission requires grains with a total cross-sectional area of roughly 10^{23} cm^2 (e.g., Kalas et al. 2008; Currie et al. 2012; Galicher et al. 2013; Kalas et al. 2013).

Two types of collision models can produce a clump of dust emission at large distances from an A-type star. In the simplest picture, two objects with radii of roughly 100 km collide at high velocity and generate an expanding cloud of small particles (e.g., Kalas et al. 2008; Galicher et al. 2013; Kenyon et al. 2014; Lawler et al. 2015). Clouds expanding at the escape velocity of a pair of 100 km objects are unresolved on 50–100 yr time scales (e.g., Galicher et al. 2013; Kenyon et al. 2014; Lawler et al. 2015). Smaller ejected particles with larger optical depth generally expand more rapidly (e.g., Gault et al. 1963; Housen & Holsapple 2003). If these particles contain a reasonable amount of mass, HST or JWST images should resolve Fomalhaut b within the next decade (e.g., Tamayo 2013; Kenyon et al. 2014). When expanding clouds have an internal velocity dispersion, differential motion shears the cloud into a ring (Kenyon & Bromley 2005; Kenyon et al. 2014). Over the next decade, HST or JWST observations can also test this prediction.

Alternative models posit a disk-shaped or a semi-spherical swarm of irregular satellites orbiting a super-Earth mass planet (Kalas et al. 2008; Kennedy & Wyatt 2011; Kenyon et al. 2014). In this approach, a collisional cascade among particles with radii $r \lesssim$ 500–1000 km maintains a large population of dust grains over the 200–400 Myr age of Fomalhaut. Analytic results for the long-term evolution favor particles with a power-law size distribution in swarms with masses of roughly 0.1 $M_\oplus$ around planets with masses $M_p \approx 10\ M_\oplus$. However, the radius of the largest object in the cascade (r_{max}) depends on the slope q of the power-law size distribution, where smaller q requires larger r_{max}. Large r_{max} requires very massive satellite swarms.

Observational tests of this model are possible but more complicated (e.g., Kenyon et al. 2014). Radiation pressure from the central star prevents small particles with $r \lesssim 100$ μm from remaining bound to the planet. Ejection of these particles produces a distinct trail along the planet's orbit. Simple estimates suggest the density of small particles ejected from massive planets is detectable (Kenyon et al. 2014). Testing this aspect of the model requires more detailed analyses of the dust ejected from the satellite swarm.

To explore this picture in more detail, we examine a suite of numerical simulations for spherical swarms of satellites orbiting super-Earth mass planets. Aside from deriving the evolution of dust clouds as a function of the mass of the planet and the surrounding satellite system, we consider how the amount of dust orbiting the planet depends on the initial radius of the largest satellite, the bulk strength of satellites, and the recipe for distributing the debris from a collision into lower mass objects. For a standard model, swarms with initial masses $M_d = 0.01\ M_p$ and $r_{max} \approx$ 200–400 km orbiting planets with masses $M_p =$ 10–100 $M_\oplus$ match the observed cross-sectional area of Fomalhaut b. Calculations with weaker satellites allow lower mass swarms to match the data.

For planets with $M_p \approx 30$–$300\ M_\oplus$, $a \approx 100$ AU, and ages of 1–10 Myr, satellite swarms have large optical depth $\tau \approx 0.1$–1. Relative to the central star, predicted contrast ratios of $10^{-6} - 10^{-7}$ are at least a factor of 100 larger than observed in Fomalhaut b. Observations with ground-based AO systems (e.g., Biller et al. 2013) or HST (e.g., Schneider et al. 2014) can place limits on the frequency of optically thick satellite swarms around planets orbiting nearby young stars.

To connect our results with previous analytic work, we begin our discussion with the derivation of a simple analytic model (§2). After summarizing the numerical approach (§3), we describe the outcomes of simulations as a function of various input parameters (§4). The paper concludes with a brief discussion (§5) and a summary of the major results (§6).

2. ANALYTIC MODEL

To interpret observations of debris disks c. 2000, Wyatt & Dent (2002) and Dominik & Decin (2003) developed an analytic model for the long-term evolution of a swarm of large solid objects in a circumstellar disk. Kennedy & Wyatt (2011) later extended this approach to spherical swarms of satellites orbiting a massive planet (see also Kennedy et al. 2011). In a swarm of satellites, objects with radius r, mass m, and mass density ρ orbit within a spherical shell with width δa centered at a distance a from a planet with mass M_p and radius R_p. The planet orbits with semimajor axis a_p from a central star with mass $M_\star$ and luminosity $L_\star$. Destructive collisions between satellites produce a collisional cascade which slowly grinds solids into smaller and smaller objects. Defining an upper mass limit m_{max} for solids participating in the cascade, the analytic model yields a simple formula for $N_{max}(t)$, the number of these large objects as a function of time. If radiation pressure sets m_{min}, a lower mass limit for solids with stable orbits around the planet, then the cascade produces a power-law size distribution between m_{min} and m_{max} (e.g., Dohnanyi 1969; Williams & Wetherill 1994; O'Brien & Greenberg 2003; Kobayashi & Tanaka 2010). Setting the slope of this size distribution yields another simple formula for the time evolution of the surface area of the dust cloud $A_d(t)$. Adopting optical properties for solids in the cloud yields the dust luminosity $L_d(t)$.

2.1. Time evolution

To derive expressions for $N_{max}(t)$ and $A_d(t)$, Wyatt & Dent (2002), Dominik & Decin (2003), and Kennedy & Wyatt (2011) adopt the particle-in-a-box model, where kinetic the-

ory sets the collision rate $\dot{N}$. Defining V as the volume of the spherical shell, σ as the geometric cross-section, and v as the relative particle velocity, each particle has a collision time $t_c \approx N_0^{-1}(V/2\sigma v)$ where N_0 is the initial number of particles[1]. If all collisions between particles are destructive, the number of large particles declines at a rate $\dot{N}_{max} \approx -N_{max}^2/N_0 t_c$. Solving for $N_{max}(t)$:

$$N_{max}(t) = \frac{N_{max,0}}{1 + t/t_c} \ , \tag{1}$$

where $N_{max,0}$ is the number of large objects at $t = 0$.

With $N_{max}(t)$ known, the total cross-sectional area and dust luminosity follow. For any power-law size distribution with $N(r) \propto r^{-q}$, the total mass M_d and cross-sectional area A_d of the swarm are simple functions of the minimum size, the maximum size, and the slope q (e.g., Wyatt & Dent 2002; Dominik & Decin 2003). The stellar energy intercepted by the solids is $L_d = A_d/4\pi a_p^2$. If m_{min}, m_{max}, and q never change, the cross-sectional area $A_{d,0}$ and the initial dust luminosity $L_{d,0}$ are simple functions of N_{max} and the parameters of the size distribution. Thus,

$$A_d(t) = \frac{A_{d,0}}{1 + t/t_c} \ . \tag{2}$$

and

$$L_d(t) = \frac{L_{d,0}}{1 + t/t_c} \ . \tag{3}$$

At early times ($t \ll t_c$), the cross-sectional area, dust luminosity and total mass in the disk are roughly constant. At late times ($t \gg t_c$), the area, luminosity, and mass decline as t^{-1} (Wyatt & Dent 2002; Dominik & Decin 2003).

2.2. Destructive Collisions

The simple relations in eqs. (1)–(3) hinge on maintaining a power-law size distribution with an invariant slope for particles with $m_{min} \lesssim m \lesssim m_{max}$. This outcome requires destructive collisions among equal mass objects. Collision outcomes depend on the ratio $Q_c/Q_D^\star$, where $Q_D^\star$ is the collision energy per unit mass needed to eject half the mass of a pair of colliding planetesimals to infinity and Q_c is the center of mass collision energy per unit mass (see also Wetherill & Stewart 1993; Williams & Wetherill 1994; Tanaka et al. 1996; Stern & Colwell 1997; Kenyon & Luu 1999; O'Brien & Greenberg 2003; Kobayashi & Tanaka 2010). For impact velocity v, $Q_c = \mu v^2/2(m_1 + m_2)$, where $\mu =$

[1] Formally, collisions destroy two identical particles on the time scale $2t_c$; t_c is then the time scale to destroy a single particle.

$m_1 m_2/(m_1 + m_2)$ is the reduced mass for a pair of colliding planetesimals with masses m_1 and m_2. For equal mass objects, $Q_c = v^2/8$.

Following standard practice,

$$Q_D^\star = Q_b r_c^{\beta_b} + Q_g \rho_p r_c^{\beta_g} \tag{4}$$

where $Q_b r_c^{\beta_b}$ is the bulk component of the binding energy, $Q_g \rho_g r_c^{\beta_g}$ is the gravity component of the binding energy, and r_c is the radius of a merged pair of planetesimals (e.g., Benz & Asphaug 1999; Leinhardt et al. 2008; Leinhardt & Stewart 2009). For icy objects, we adopt parameters – $Q_b \approx 10^5$ erg g^{-1} cm$^{-\beta_b}$, $\beta_b \approx -0.40$, $Q_g \approx 0.11$ erg g^{-2} cm$^{3-\beta_g}$, and $\beta_g \approx 1.3$ – which are broadly consistent with analytic estimates, laboratory experiments, and numerical simulations (see also Davis et al. 1985; Holsapple 1994; Love & Ahrens 1996; Housen & Holsapple 1999; Ryan et al. 1999; Arakawa et al. 2002; Giblin et al. 2004; Burchell et al. 2005).

Setting $Q_c \approx Q_D^\star$ establishes constraints on the particles destroyed by an adopted collision velocity. Among large particles with $r \gtrsim 1$ km, the collision energy must overcome the gravitational component of the binding energy: $r_{max} = (v^2/8Q_g\rho)^{0.77}$. When two particles with $r \lesssim 1$ cm collide, the impact kinetic energy must exceed the strength component of the binding energy: $r_{min} = (8Q_b/v^2)^{0.4}$. In between these two limits, $Q_D^\star$ is always smaller than Q_c. Thus, collisions with velocity v destroy particles with $r_{min} \leq r \leq r_{max}$. Because the debris from these collisions produces an equilibrium size distribution between r_{min} and r_{max}, continued destructive collisions maintain this size distribution.

To relate these constraints to the properties of the planet and the central star, it is convenient to use the Hill radius,

$$R_H = \left(\frac{M_p}{3M_\star}\right)^{1/3} a_p \ , \tag{5}$$

which establishes a volume where the gravity from the planet overcomes the gravity from the central star. For particles orbiting with random inclination in a spherical shell surrounding the planet, the collision velocity is a simple function of the orbital velocity v_K, $v = f_v v_K$ (Kennedy & Wyatt 2011). For a shell with $a = \eta_1 R_H$, $v = 3^{1/6}(G/\eta_1)^{1/2} f_v M_p^{1/3} M_\star^{1/6} a_p^{-1/2}$.

For Fomalhaut b, we adopt a set of fiducial parameters to evaluate the collision velocity and other aspects of the collisional cascade (see also Kennedy & Wyatt 2011). A 10 $M_\oplus$ planet orbits a 1.9 $M_\odot$ star at $a_p \approx 120$ AU. Satellites with $\rho = 1$ g cm^{-3} and $r \approx 100$ km lie in a spherical shell with $\eta_1 = 0.2$ and $\eta_2 = 0.5$. Orbits with much larger η_1 (≈ 0.3–1) are unstable (e.g., Hamilton & Burns 1992; Hamilton & Krivov 1997; Toth 1999; Shen & Tremaine 2008; Martin & Lubow 2011); more compact configurations evolve too quickly. Clouds with (i)

typical mass $x_d = M_d/M_p = 0.01$ and (ii) collision velocities slightly larger than Keplerian, $f_v = 1.25$ (Kennedy & Wyatt 2011), then have orbital velocity

$$v \approx 0.32 \left(\frac{f_v}{1.25}\right) \left(\frac{\eta_1}{0.2}\right)^{-1/2} \left(\frac{M_p}{10\ M_\oplus}\right)^{1/3} \left(\frac{M_\star}{1.9\ M_\odot}\right)^{1/6} \left(\frac{a_p}{120\ \mathrm{AU}}\right)^{-1/2}\ \mathrm{km\ s^{-1}}\ . \quad (6)$$

Substituting this velocity into our expressions for r_{min} and r_{max}:

$$r_{max} \approx 100 \left(\frac{f_v}{1.25}\right)^{1.54} \left(\frac{\eta_1}{0.2}\right)^{-0.77} \left(\frac{\rho}{1\ \mathrm{g\ cm^{-3}}}\right)^{-0.77} \left(\frac{Q_g}{0.11\ \mathrm{erg\ g^{-2}\ cm^{1.7}}}\right)^{-0.77} \left(\frac{M_p}{10\ M_\oplus}\right)^{0.51} \left(\frac{M_\star}{1.9\ M_\odot}\right)^{0.255} \left(\frac{a_p}{120\ \mathrm{AU}}\right)^{-0.77}\ \mathrm{km}\ . \quad (7)$$

and

$$r_{min} \approx 1.8 \times 10^{-4} \left(\frac{f_v}{1.25}\right)^{-5} \left(\frac{\eta_1}{0.2}\right)^{5/2} \left(\frac{Q_b}{10^5\ \mathrm{erg\ g^{-1}\ cm^{0.4}}}\right)^{5/2} \left(\frac{M_p}{10\ M_\oplus}\right)^{-5/3} \left(\frac{M_\star}{1.9\ M_\odot}\right)^{-5/6} \left(\frac{a_p}{120\ \mathrm{AU}}\right)^{5/2}\ \mu\mathrm{m}. \quad (8)$$

Objects with intermediate sizes – $r_{min} < r < r_{max}$ – have smaller $Q_D^\star$ than particles with $r = r_{min}$ or $r = r_{max}$. Radiation pressure typically ejects particles with $r \lesssim r_b$, where $r_b \gg r_{min}$. Thus, all particles with $r \lesssim r_{max}$ are either destroyed or ejected.

For simplicity, many analytic models adopt a $Q_D^\star$ which is independent of radius. Eqs. 7–8 justify this assumption: any $Q_D^\star$ which ensures the destruction of objects with some maximum radius guarantees that collisions will also destroy all smaller objects.

2.3. Size Distribution

With r_{max} known as a function of Q_g, deriving $A_{d,0}$ requires values for r_{min} and q. In numerical simulations of collisional cascades, the slope of the equilibrium power-law size distribution is $q \approx 3.5$–3.7 (e.g., Dohnanyi 1969; Williams & Wetherill 1994; O'Brien & Greenberg 2003; Kobayashi & Tanaka 2010). In models where $Q_D^\star$ is constant with particle radius, $q \approx 3.5$. When the bulk strength component of $Q_D^\star$ declines with radius, $q \approx 3.7$. We adopt $q = 3.5$.

In an optically thin swarm of satellites, radiation pressure sets r_{min}. For dust grains orbiting the central star, radiation pressure removes particles smaller than the 'blowout' radius, $r_b \approx (3 L_\star Q_{pr}/8\pi c G \rho M_\star)$, where Q_{pr} is the radiation pressure coefficient which accounts

for absorption and scattering (e.g., Burns et al. 1979). Fomalhaut has $M_\star = 1.9\ M_\odot$ and $L_\star \approx 20\ L_\odot$; thus, $r_b \approx 7\ \mu$m for icy grains with $Q_{pr} = 1$ and $\rho = 1$ g cm^{-3}.

When particles orbit a planet, ejection depends on the orbital velocity of a particle around the planet relative to the orbital velocity of the planet around the star (e.g., Burns et al. 1979). Defining $\beta = F_r/F_g$ as the ratio of the radiative force to the gravitational force, radiation ejects particles orbiting a planet when $\beta \gtrsim \beta_0(v/v_p)$, where v is the orbital velocity of a particle around the planet, v_p is the orbital velocity of the planet around the star, and $\beta_0 \approx 1/3$ to 1. Thus, $r_b \lesssim (3L_\star Q_{pr}/8\pi cG\rho M_\star)(v_p/\beta_0 v)$. In physical units,

$$r_b \lesssim 100 \left(\frac{2/3}{\beta_0}\right) \left(\frac{\eta_1}{0.2}\right)^{1/2} \left(\frac{Q_{pr}}{1}\right) \left(\frac{\rho}{1\ \mathrm{g\ cm^{-3}}}\right)^{-1} \left(\frac{M_p}{10\ M_\oplus}\right)^{-1/3} \left(\frac{M_\star}{1.9\ M_\odot}\right)^{-2/3} \left(\frac{L_\star}{20\ L_\odot}\right)\ \mu\mathrm{m}\ . \quad (9)$$

More massive planets hold onto smaller particles. For particles orbiting at a fixed fraction of the Hill radius, r_b is independent of a_p.

Setting $r_{min} = r_b$ and integrating over a power-law size distribution with $q = 3.5$ yields the initial surface area. For convenience, we separate the linear dependence of $A_{d,0}$ on the cloud mass M_d into a linear dependence on $x_d M_p$:

$$A_{d,0} = 1.4 \times 10^{24} \left(\frac{x_d}{0.01}\right) \left(\frac{M_p}{10\ M_\oplus}\right) \left(\frac{r_{max}}{100\ \mathrm{km}}\right)^{-1/2} \left(\frac{r_{min}}{100\ \mu\mathrm{m}}\right)^{-1/2}\ \mathrm{cm}^2\ . \quad (10)$$

With these parameters, the initial surface area is roughly 10 times the observed surface area of a dust cloud in Fomalhaut b.

2.4. Collision Time

Deriving the long-term evolution of A_d requires a numerical estimate for the collision time. The simplest approaches adopt the lifetime of the largest particle against collisions with identical particles. More elaborate treatments include the impact of collisions with much smaller particles (e.g., Wyatt et al. 2007a,b; Kobayashi & Tanaka 2010; Kennedy & Wyatt 2011; Kennedy et al. 2011). Because the lifetime depends on a variety of relatively unknown parameters, we consider the time scale for destructive collisions among identical particles.

To estimate the collision time, we again consider a spherical shell with semimajor axis $a = \eta_1 R_H$ and thickness $\delta a = \eta_2 a$. The volume of this shell is $V = 4\pi a^2 \delta a = 4\pi\eta_1^3\eta_2 a_p^3 M_p/(3M_\star)$. If the cloud consists of a monodisperse set of particles with mass m,

$N = M_d/m$. To express the mass of the cloud relative to the mass of the planet, we define $x_d = M_d/M_p$ and use $m = 4\pi\rho r_{max}^3/3$. Then, $N = 3x_d M_p/4\pi\rho r_{max}^3$. For mono-disperse particles, the collisional cross-section is $\sigma = 4\pi r_{max}^2$. Thus, $N\sigma = 3x_d M_p/2\rho r_{max}$. Combining all of these relations and defining $t_c = V/(2N_0\sigma v)$,

$$t_c = \left(\frac{2\pi\ \eta_1^{7/2}\ \eta_2\ \rho\ r_{max}\ a_p^{7/2}}{3^{13/6}\ G^{1/2}\ f_v\ x_d\ M_\star^{7/6} M_p^{1/3}} \right) \ . \tag{11}$$

When the cascade contains substantial mass in particles with sizes smaller than r_{max}, the collision time is different from the t_c in eq. 11 (e.g., Wyatt et al. 2007a,b; Kobayashi & Tanaka 2010; Kennedy & Wyatt 2011; Kennedy et al. 2011). For the fragmentation parameters used in eq. 4 and the collision velocity from eq. 6, collisions between one object with $r \approx r_{max}$ and another object with $r \gtrsim 0.1\ r_{max}$ destroy both objects. Cratering collisions with a much smaller object, $r \ll r_{max}$, eject roughly 2.7 times the mass of the smaller object. Thus, every collision removes mass from the largest object. Accounting for cratering collisions and a broader range of catastrophic collisions (i) allows larger objects to participate in the cascade, increasing r_{max}, and (ii) increases the rate large objects lose mass, shortening t_c.

Deriving the impact of these additional collisions requires integrating the collision rate over the size distribution. However, the range of sizes included in the integration depends on the collision rate. Although it is possible to construct an iterative solution, most investigators simply set r_{max} as a free parameter and derive the collision time for an r_{min} set by the blowout radius r_b. The revised collision time is then ~ 0.01–$4\ t_c$ (Wyatt et al. 2007a; Kobayashi & Tanaka 2010; Kennedy & Wyatt 2011). However, this factor depends on v, $Q_D^\star$, r_{min}, and the details of the size distribution. For simplicity, we add a multiplicative parameter α (≤ 4) to our expression for the collision time. In §4.5, comparisons between this analytic model and our numerical results allow us to infer α for irregular satellite systems in Fomalhaut b.

Converting the parameters in eq. 11 to physical units, the collision time is:

$$\begin{aligned} t_c \ = \ & 4.3 \times 10^6 \left(\frac{\alpha}{1}\right) \left(\frac{\eta_1}{0.2}\right)^{7/2} \left(\frac{\eta_2}{0.5}\right) \left(\frac{f_v}{1.25}\right)^{-1} \left(\frac{x_d}{0.01}\right)^{-1} \left(\frac{M_p}{10\ M_\oplus}\right)^{-1/3} \left(\frac{M_\star}{1.9\ M_\odot}\right)^{-7/6} \\ & \left(\frac{\rho}{1\ \mathrm{g\ cm^{-3}}}\right) \left(\frac{r}{100\ \mathrm{km}}\right) \left(\frac{a_p}{120\ \mathrm{AU}}\right)^{7/2}\ \mathrm{yr}\ . \end{aligned} \tag{12}$$

More massive clouds, planets, and central stars shorten the collision time. Clouds consisting of larger, denser satellites orbiting planets with larger semimajor axes lengthen the collision time. Collisional cascades remove $\sim 90\%$ of the initial mass in ~ 10 collision times. Thus, the lifetime of the cascade is a significant fraction of the lifetime of an A-type star like Fomalhaut.

2.5. Example

To illustrate the analytic model, we consider a simple example. With standard parameters, $M_\star = 1.9\ M_\odot$, $L_\star = 20\ L_\odot$, $a_p = 120$ AU, $\eta_1 = 0.2$, $\eta_2 = 0.5$, $\rho = 1$ g cm^{-3}, $Q_b = 10^{-5}$ erg g^{-1} cm$^{0.4}$, $f_v = 1.25$, and $r_{max} = 100$ km, eqs. (2) and (10) yield the time evolution of the surface area. To compare with observations of Fomalhaut b, we adopt nominal values and uncertainties for the surface area, $A_b \approx 1^{+1}_{-0.5} \times 10^{23}$ cm^2 and age, $t_b \approx 200^{+200}_{-100}$ Myr (e.g., Mamajek 2012; Kenyon et al. 2014, and references therein). The relative surface area of a model satellite swarm is then $A_d(t)/A_b$. For satellite swarms with $x_d = 0.01$ and a range of masses for the central planet, Figure 1 compares the time evolution of the relative surface area evolves with observations of Fomalhaut b.

For the adopted parameters, satellite swarms around super-Earths with $M_p = 30$–$100\ M_\oplus$ match the data. Models with $M_p = 10\ M_\oplus$ and $M_p = 300\ M_\oplus$ almost match the data. Satellite evolution around lower mass or more massive planets do not match the data.

Adopting other parameters leads to similar conclusions. Factor of two (ten) changes in r_{max} (x_d) modify the relative surface area by $\sim 25\%$ at ages of 100–400 Myr. A modest, 20% increase in η_1 increases t_c by a factor of two at the expense of a 5% reduction in $A_{d,0}$. This change yields a better match to the data for models with $M_p = 10\ M_\oplus$, at the cost of worse matches for models with $M_p = 100\ M_\oplus$.

2.6. Advantages and Limitations

The analytic model has several clear advantages. It is conceptually simple, easy to modify, and straightforward to calculate. The observable quantities A_d and L_d have obvious relationships to the physical parameters. Generating ensembles of debris clouds for plausible variations in the physical parameters allows robust comparisons with large sets of data. Comparisons between data and models yield important insights into the evolution of circumstellar debris disks and swarms of circumplanetary satellite systems (e.g., Wyatt 2008; Kennedy & Wyatt 2010, 2011; Kennedy et al. 2011; Matthews et al. 2014, and references therein).

Despite its broad success, the model does not address several interesting issues in the time evolution of irregular satellites. In current theory, planets capture material from a circumstellar disk to supply the circumplanetary swarm (e.g., Koch & Hansen 2011; Quillen et al. 2012; Gaspar et al. 2013; Nesvorný et al. 2014). If some captured objects have $r > r_{max}$, these objects may accrete material from the swarm and reduce the lifetime of smaller particles

considerably. Dynamical interactions among growing large objects could lead to significant scattering of particles within the swarm and interactions with larger satellites closer to the planet.

The analytic model also does not allow time variations in r_{min}, r_{max}, and the slope of the power law size distribution. In a real collisional cascade, small particles gradually chip away at the larger objects. Significant reductions in r_{max} shorten the lifetime of the cascade. Among smaller particles with $r \approx r_{min}$, the typical collision time of $10^2 - 10^4$ yr (for $A_d \approx 10^{25} - 10^{23}$ cm^2) is not much longer than the typical orbital period of $\sim$ 100 yr. Radiation pressure typically takes many orbital periods to eject small particles (e.g., Poppe & Horányi 2011, and references therein). Thus, r_{min} might be significantly smaller than r_b at early times, enabling a larger initial surface area which declines more rapidly with time. In between r_{min} and r_{max}, it takes many collision times to establish a power law size distribution with $q = 3.5$. If the initial size distribution is far from equilibrium, the early evolution of A_d might differ significantly from predictions of the analytic model.

Addressing these issues requires numerical simulations. For a satellite swarm where the orbital elements are fixed in time, it is straightforward to conduct a suite of coagulation calculations to learn how time variations in r_{min}, r_{max}, q, and other physical parameters impact the long term evolution of the satellite swarm. We describe our numerical approach in §3 and then discuss the results of the simulations in §4.

3. NUMERICAL MODEL

To perform numerical calculations of the collisional evolution of an irregular satellite system, we use *Orchestra*, an ensemble of computer codes for the formation and evolution of planetary systems. *Orchestra* includes a multiannulus coagulation code which derives the time evolution of a swarm of solid objects orbiting a central mass (Kenyon & Bromley 2004, 2008, 2012). Although this code was originally designed to follow solids within a circumstellar disk, it is straightforward to modify the algorithms to track solids orbiting within a spherical shell. *Orchestra* also includes an n-body code which follows the trajectories and dynamical interactions of large objects (Bromley & Kenyon 2006, 2011, 2013). In these calculations, we disable dynamical interactions between coagulation particles and the n-bodies mediated by tracer particles.

3.1. Numerical Grid

We conduct coagulation calculations of particles orbiting with semimajor axis a inside a spherical shell of width δa around a planet with mass M_p. Within this shell, there are M mass batches with characteristic mass m_k and radius r_k (Wetherill & Stewart 1993; Kenyon & Luu 1998). Batches are logarithmically spaced in mass, with mass ratio $\delta \equiv m_{k+1}/m_k$. Each mass batch contains N_k particles with total mass M_k and average mass $\bar{m}_k = M_k/N_k$. Particle numbers $N_k < 10^{15}$ are always integers. Throughout the calculation, the average mass is used to calculate the average physical radius $\bar{r}_k$, collision cross-section, collision energy, and other necessary physical variables. As mass is added and removed from each batch, the average mass changes (Wetherill & Stewart 1993).

Numerical calculations with $\delta \gtrsim 1$ lag the result of an ideal calculation with infinite mass resolution (see the Appendix). Simulations with $\delta = 1.05$–1.19 yield somewhat better solutions to the evolution of 10–100 km objects than calculations with $\delta = 1.41$–2.00. However, the evolution of the cross-sectional area of a swarm of solids is fairly independent of δ. To track the evolution of the size distribution reasonably well, we consider a suite of calculations with $\delta = 1.19$ $(= 2^{1/4})$.

In these calculations, we follow particles with sizes ranging from a minimum size r_{min} to the maximum size r_{max}. The algorithm for assigning material to the mass bins extends the maximum size as needed to accommodate the largest particles. When collisions produce objects with radii $r < r_{min}$, this material is lost to the grid.

When the average mass in a bin exceeds a pre-set promotion mass m_{pro}, the code creates a set of n-bodies with masses equal to the average mass in the bin. In these calculations, $m_{pro} = 10^{24}$ g ($r_{max} \approx 600$ km). Promoted objects are assigned a random semi-major axis, a_{pro}, in the range $(a - \delta a, a + \delta a)$, a random inclination sin i, a random orbital phase, and orbital eccentricity $e = 0$. For this first exploration of the evolution, we include the gravity of the central planet but ignore gravitational forces of nearby stars.

3.2. Initial Conditions

All calculations begin with a swarm of planetesimals with initial maximum size $\mathring{0}$ and mass density $\rho = 1$ g cm^{-3}. These particles have initial number density n_0 and total mass M_0. For the simulations in this paper, we consider two different initial size distributions for the planetesimals. To follow the analytic model as closely as possible, one set of calculations begins with a power law size distribution, $n(r) \propto r^{-q}$ and $q = 3.5$. To study whether our calculations produce this equilibrium size distribution, we begin a second set of calculations

with a mono-disperse set of planetesimals.

3.3. Evolution

The mass distribution of the planetesimals evolves in time due to inelastic collisions. All planetesimals have the same collision velocity, which is fixed at the start of each calculation. As summarized in Kenyon & Bromley (2004, 2008), we solve a coupled set of coagulation equations which treats the outcomes of mutual collisions between particles in every mass bin. We adopt the particle-in-a-box algorithm, where the physical collision rate is $n\sigma v f_g$, n is the number density of objects, σ is the geometric cross-section, v is the relative velocity from eq. 6, and f_g is the gravitational focusing factor (Wetherill & Stewart 1993; Kenyon & Luu 1998). The collision algorithm treats collisions in the dispersion regime – where relative velocities are large – and in the shear regime – where relative velocities are small (Kenyon & Luu 1998; Kenyon & Bromley 2014).

For swarms of satellites, all collisions are in the dispersion regime, where we adopt a variant of the piecewise analytic approximation of Spaute et al. (1991, see also Kenyon & Luu 1998; Kenyon & Bromley 2012). When collisions involve particles with $r \lesssim 300$ km, $f_g \lesssim 3$–4. As satellites reach sizes of 1000–2000 km, $f_g \lesssim 50$. Compared to simulations where $f_g \gtrsim 10^3 - 10^4$ (e.g., Kenyon & Bromley 2008), gravitational focusing has a modest impact on the evolution.

For each pair of colliding planetesimals and the collision energies Q_c and $Q_D^\star$ defined in §2, the mass of the merged planetesimal is

$$m = m_1 + m_2 - m_{esc} \ , \tag{13}$$

where the mass of debris ejected in a collision is

$$m_{esc} = 0.5 \ (m_1 + m_2) \left(\frac{Q_c}{Q_D^*} \right)^{b_d} \ . \tag{14}$$

The exponent b_d is a constant of order unity (e.g., Davis et al. 1985; Wetherill & Stewart 1993; Kenyon & Luu 1999; Benz & Asphaug 1999; O'Brien & Greenberg 2003; Kobayashi & Tanaka 2010; Leinhardt & Stewart 2012). Here, we consider $b_d = 1$.

To place the debris in the grid of mass bins, we set the mass of the largest collision fragment as

$$m_{max,d} = m_{L,0} \ \left(\frac{Q_c}{Q_D^*} \right)^{-b_L} \ m_{esc} \ . \tag{15}$$

To explore the sensitivity of the evolution to this algorithm, we set $m_{L,0} = 0.2$ and $b_L = 0$ or 1 (Kenyon & Bromley 2008; Kobayashi & Tanaka 2010; Weidenschilling 2010). Lower mass objects have a differential size distribution $n(r) \propto r^{-q}$. After placing a single object with mass $m_{max,d}$ in an appropriate bin, we place material in successively smaller mass bins until (i) the mass is exhausted or (ii) mass is placed in the smallest mass bin. Any material left over is removed from the grid (see also Kenyon & Bromley 2015).

4. CALCULATIONS

To examine the long-term evolution of satellite swarms, we consider a baseline model where the central star has mass 1.90 $M_\odot$ and luminosity 20 $L_\odot$. Planets with M_p = 1, 3, 10, 30, 100, or 300 $M_\oplus$ orbit with a semimajor axis a_p = 120 AU. The spherical cloud has $x_d = 0.01$, $\eta_1 = 0.2$, and $\eta_2 = 0.5$. Particles within the shell have $\rho = 1$ g cm^{-3}, r_{min} = 100 μm and r_{max} = 50, 100, 200, or 400 km. The initial size distribution is a power law with $n(r) \propto r^{-q}$ and $q = 3.5$. To establish collision outcomes, we adopt the fragmentation parameters – Q_b, Q_g, β_b, and β_g – summarized in §2.2. For the largest object in the debris we set $b_L = 0$.

To check the sensitivity of the calculations to these parameters, we vary one parameter and hold others fixed. In turn, we derive results for $x_d = 0.001$ or 0.0001; r_{min} = 10 μm or 1 mm; (Q_b,Q_g) = $(5 \times 10^4, 0.055)$ or $(2.5 \times 10^4, 0.0275)$; and $b_L = 1$. Although we perform these calculations for all combinations of M_p and r_{max} in the baseline model, we focus our discussion primarily on calculations with M_p = 10 $M_\oplus$.

In describing the results of the simulations, we consider the long-term evolution of the size of the largest object (§4.1), the size distribution (§4.2), and the cross-sectional area (§4.3). In many of the simulations, the masses of 2–6 objects reach the promotion mass. After promotion into the n-body portion of *Orchestra*, continued growth leads to strong dynamical interactions among a few n-bodies. Several examples of the long-term actions of the n-bodies illustrate their likely impact on the rest of the swarm and satellites orbiting closer to the planet (§4.4). In §4.5, comparisons with predictions of the analytic model allow us to clarify how the behavior of the swarm differs in the two approaches.

4.1. Evolution of the Size of the Largest Object

4.1.1. Baseline model

In the baseline model, the radius of the largest object r_{max} depends on the mass of the central planet and the initial r_{max} (Figs. 2–3). When M_p = 30–300 $M_\oplus$, the orbital velocity at $0.2R_H$ is sufficient to destroy 100 km objects. Occasional catastrophic collisions among pairs of 100 km objects destroy them completely; the population of these objects gradually diminishes with time. More frequent cratering collisions with much smaller objects chip away at the mass in every large object. The average radius of these objects gradually declines from 100 km at t = 0 to 60–70 km at t = 1 Gyr.

When $M_p = 10\ M_\oplus$, collisions almost shatter pairs of 100 km objects. Barring collisions with smaller objects, these objects grow slowly. However, cratering collisions with other satellites reduce their mass faster than collisions with the largest objects increase their mass. Thus, r_{max} gradually declines with time.

When M_p = 1–3 $M_\oplus$, the orbital velocity is not sufficient to destroy 100 km objects (Fig. 2, lower orange and magenta curves). Cratering collisions are also insufficient to reduce their mass. Although collisions destroy all smaller objects, these objects grow slowly with time. After 1 Gyr, satellites orbiting a 3 $M_\oplus$ planet reach radii of 400 km; satellites orbiting a $1M_\oplus$ planet have $r_{max} \gtrsim 1000$ km. In some cases, these calculations yield several n-bodies which interact dynamically. We discuss several of these outcomes in §4.4.

In calculations with smaller r_{max}, it is easier to destroy the largest planetesimals. Cratering collisions are also more efficient. For M_p = 3–300 $M_\oplus$, r_{max} declines more rapidly with time (Fig. 3). By the end of the calculation at 1 Gyr, the largest satellites have r_{max} = 2.5 km for $M_p = 300\ M_\oplus$ up to r_{max} = 35 km for $M_p = 3\ M_\oplus$. When $M_p = 1\ M_\oplus$, the collision energy is still insufficient to destroy 50 km objects. Thus, these objects grow slowly to $\sim$ 300 km over 1 Gyr.

When r_{max} is initially larger than 100 km, it is easier for large objects to grow over time (Figs. 2–3). Satellites with initial radii of 200 km (400 km) reach radii of 1000–2000 km in 0.3–1 Gyr around 1–10 $M_\oplus$ (1–30 $M_\oplus$) planets. In several calculations, pairs of large satellites promoted into the n-body code scatter one another out of the grid. Scattering leaves behind a few much smaller objects, reducing r_{max} within the grid.

Collisional evolution with larger satellites orbiting more massive planets always reduces the size of the largest objects. For 300 $M_\oplus$ planets, catastrophic and cratering collisions diminish the sizes of the largest satellites by 25% to 40%. The reduction in size is smaller, $\sim$ 10% to 25% for 200–400 km satellites orbiting 100 $M_\oplus$ planets.

4.1.2. Initial cloud mass

Changing the initial mass of the cloud has an obvious impact on the long-term evolution of the largest objects. When the mass of the cloud is smaller, the collision time is longer. Evolution is correspondingly slower. Thus, the sizes of the largest objects remain closer to their initial values.

Fig. 4 illustrates the impact of initial cloud mass on particle size for satellites orbiting 300 $M_\oplus$ planets. When the initial r_{max} is small, differences in the evolution are obvious. When $x_d = 0.01$, it takes only 30 Myr for r_{max} to decline to 20 km. A factor of 10 reduction in the initial cloud mass increases this time scale to 300 Myr. Another factor of ten reduction increases the time sale to 3 Gyr.

As we increase the initial r_{max}, the initial cloud mass has a smaller and smaller impact on the overall evolution. Although reducing the cloud mass increases collision times, large objects already have long collision times. Slow evolution simply becomes slower. Larger objects are also more impervious to collisional destruction; reducing x_d makes them even more impervious.

4.1.3. Size of the smallest particles

Not surprisingly, modifying the initial size of the smallest objects in the grid has little impact on the evolution of the largest objects in the grid (Fig. 5). When $M_p = 10\ M_\oplus$ and the initial r_{max} is 50–100 km, the collisional cascade effectively destroys the largest objects in the grid. Collisions with the smallest particles in the grid remove little mass from the largest objects. Changing r_{min} by a factor of ten has little impact on r_{max}.

When the initial r_{max} is larger, the largest objects grow slowly with time. Large objects accrete little mass from the ensemble of objects with radii close to r_{min}. Changing r_{min} barely modifies the accretion rate.

At late stages in the growth of large satellites, stochastic variations in the collision rate among large satellites produces large changes in r_{max}. As large objects grow, the rate of collisions with other large objects declines and becomes more random. These random collisions produce large fluctuations in the time scale for objects to reach sizes of 1000 km (Fig. 5, top curves). When these objects are promoted into the n-body code, random dynamical interactions then yield random drops (or spikes) in r_{max}.

4.1.4. Mass of the largest object in the debris

How we distribute the debris into smaller mass bins also has modest impact on the evolution of the largest objects (Fig. 6). In our baseline model with $m_{L,0} = 0.2$ and $b_L = 0$, debris tends to fill bins with larger masses than in calculations with $m_{L,0} = 0.2$ and $b_L = 1$. When the cascade destroys large objects, the mass loss rate from the grid depends on the rate collisions transport mass to smaller and smaller objects. Thus, we expect calculations with $b_L = 1$ to lose mass somewhat more rapidly than those with $b_L = 0$. When larger objects grow, cratering collisions are less important; the exponent b_L then has negligible importance.

Our results confirm these expectations. In the top curves of Fig. 6, 200 km and 400 km objects grow with time. Superimposed on a gradual rise in r_{max} with time, stochastic variations produce a few random increases in r_{max}. Later, random dynamical interactions eject objects promoted into the n-body grid. The final radii of large objects is fairly independent of b_L.

In the lower curves of the figure, 50 km and 100 km satellites get smaller and smaller with time. Despite the somewhat larger mass loss of models with $b_L = 1$, the final radii are independent of b_L.

4.1.5. Binding energy

As discussed in §2, $Q_D^\star$ – the binding energy of satellites – sets the size of the largest object destroyed in collisions with fixed impact velocity. Smaller $Q_D^\star$ allows collisions to destroy larger objects.

Fig. 7 illustrates the impact of smaller $Q_D^\star$ on the evolution of 100 km and 400 km satellites orbiting 10 $M_\oplus$ planets. When $r_{max} = 100$ km, the $Q_D^\star$ in our baseline calculations is small compared to the collision energy. Collisions completely shatter these satellites. Although reducing $Q_D^\star$ makes them easier to destroy, the amount of debris lost in a collision is fairly similar. Thus, the evolution of 100 km satellites is independent of $Q_D^\star$.

In our baseline models, 400 km objects grow throughout the calculation. At late times, these objects reach sizes approaching 2000 km. Reducing $Q_D^\star$ has a clear impact on the growth of these objects. A factor of two reduction in $Q_D^\star$ prevents large objects from growing past 1000 km. Collisions among smaller objects are more destructive, removing objects from the grid more rapidly. With fewer objects to accrete, the growth of the largest objects stalls.

Another factor of two reduction in $Q_D^\star$ completely halts the growth of 400 km objects.

Catastrophic and cratering collisions reduce these sizes of these objects by 35% to 40% in 1 Gyr.

4.1.6. Initial size distribution

As a final example in this sequence, we consider the impact of the initial size distribution. When calculations start with a mono-disperse set of satellites, cratering collisions do not occur. If collisions between the large objects are catastrophic, the debris populates smaller size bins. Cratering collisions begin. Continued cratering and catastrophic collisions populate smaller and smaller size bins. Once all of the mass bins have debris, catastrophic and cratering collisions remove mass from all bins in the grid. Compared to our baseline calculations, these calculations have somewhat more mass in larger size bins. For the largest objects, collisions with larger small particles have a larger collision energy than collisions with smaller small particles. Thus, calculations with a mono-disperse set of satellites evolve somewhat faster than our baseline calculations.

If large object collisions promote growth, there is less debris in smaller mass bins. Cratering collisions are less effective in filling smaller mass bins. Collisions between objects in these smaller bins are less frequent; mass loss from the grid is smaller. As these calculations proceed, there is much more mass in large objects (which are stronger) than in small objects (which are weak). The largest objects then grow faster.

Our simulations confirm these expectations (Fig. 8). When the initial r_{max} is 50 km, collisions are destructive. The largest objects get smaller and smaller with time. At late times, the satellites in the mono-disperse calculations are somewhat smaller than those in calculations with an initial power-law size distribution.

When the initial r_{max} is 100 km, the evolution is very sensitive to the initial size distribution. In §2, the analytic model suggests $r_{max} = 100$ km for satellites orbiting a 10 $M_\oplus$ planet. For this initial size, cratering collisions are critical. When they are present, r_{max} declines with time. When they are not present, r_{max} grows with time. The figure shows this dichotomy clearly. With no initial size distribution, 100 km objects grow slowly with time. With the power law initial size distribution, r_{max} gets smaller and smaller with time.

Among larger satellites with $r_{max} = 200$ km or 400 km, the evolution also depends on the initial size distribution. With no cratering collisions among smaller objects in the grid, the cascade in fairly inactive. The mass in the grid is nearly constant in time. With more mass in the grid, the largest objects grow more rapidly. Promotion into the n-body grid occurs earlier; dynamical interactions are more severe. In these calculations, scattering of

n-bodies produced from a mono-disperse set of satellites leaves behind a few small objects which have suffered few collisions and are close to their original sizes.

4.2. Evolution of the Size Distribution

In standard collisional cascade models, destructive collisions generate a roughly constant mass flow from the largest objects to the smallest objects (e.g., Dohnanyi 1969; Williams & Wetherill 1994; O'Brien & Greenberg 2003; Kobayashi & Tanaka 2010). When $r_{min} \approx 0$, catastrophic and cratering collisions maintain a power law cumulative size distribution $n(> r) \propto r^{-q_c}$ with $q_c \approx 2.5$–2.7. When $r_{min} > 0$, cratering collisions between objects with $r < r_{min}$ and those with $r > r_{min}$ do not occur. Fewer collisions reduces the mass flow rate for $r < r_{min}$. Mass then builds up in bins with $r \gtrsim r_{min}$. This excess of particles increases the rate of cratering collisions among larger particles, creating a deficit among these particles. Together, the excess and the deficit produce a 'wave' in the power law size distribution (e.g., Campo Bagatin et al. 1994; O'Brien & Greenberg 2003). Over time, continued collisional evolution tends to produce other waves among particles with larger radii.

Addressing wave production in a numerical simulation requires an artificial extension of the size distribution to much smaller sizes. For an adopted size distribution for $r < r_{min}$, it is possible to calculate the collision rate analytically and to correct the mass flow rate for particles with $r \approx r_{min}$ (e.g., O'Brien & Greenberg 2003). For Fomalhaut b, however, radiation pressure removes particles with $r < r_{min}$ on time scales much smaller than the collisional time. While some of these particles might lie on orbits which occasionally bring them back into the satellite swarm, most never return. Thus, real satellite swarms likely have wavy size distributions.

In the rest of this section, we examine how 'equilibrium' wavy size distributions depend on model parameters. To discuss the time evolution of these size distributions, we derive the relative cumulative size distribution. At each r_k in the grid, the cumulative size distribution $n(> r)$ is the number of objects with radius larger than r. To isolate the waviness about a power law, we define the relative cumulative size distribution

$$n_{c,rel} = n(> r)/n_0 r^{-q_n} \ , \tag{16}$$

where n_0 is a normalization factor. For these calculations, we adopt $q_n = 2$ and normalize the relative cumulative size distribution to 1 at 10 km or at 100 km.

By normalizing every relative cumulative size distribution at 10 km or 100 km, we suppress the natural evolution of n_0 with time. In all calculations, n_0 follows the standard

evolution of the total mass in satellites: roughly constant at early times and then declining linearly with time at later times. In this section, we focus on the evolution of the shape of the size distribution. We return to the long-term evolution of the surface area in §4.3.

4.2.1. Baseline model

In the baseline model, the initial size distribution is a power law from $r_{min} = 100$ μm to $r_{max} = 50$, 100, 200, or 400 km. Large satellites tend to grow. Catastrophic and cratering collisions slowly reduce the sizes of satellites. For the adopted starting conditions, the collision time is 10–100 Myr. We expect the debris from destructive collisions to establish an equilibrium size distribution on this time scale.

Fig. 9 illustrates the evolution of $n_{c,rel}$ for calculations with $M_p = 10$ $M_\oplus$ and $r_{max} = 100$ km. This evolution is very different from standard predictions for a collisional cascade, $n_{c,rel} \propto r^{-q_r}$ and $q_r \approx 0.5$–0.75[2] (e.g., Dohnanyi 1969; Williams & Wetherill 1994; O'Brien & Greenberg 2003; Kobayashi & Tanaka 2010). After only 0.1 Myr, $n_{c,rel}$ develops a characteristic shape, consisting of (i) a steep rise from r_{max} to $r \approx 50$ km, (ii) a gradual rise from 50 km to 0.1 km, (iii) a steep drop from 0.1 km to 30 cm, and (iv) a steep rise from 30 cm to 100 μm. The rise from 50 km to 0.1 km has several distinct large-scale oscillations; other fluctuations are small relative to the overall trend. After 1–10 Myr, $n_{c,rel}$ is independent of time except at large sizes $r \gtrsim$ 10–30 km.

In this calculation, the lack of particles with $r \lesssim 100$ μm produces the pronounced wave in the size distribution from 100 μm to 0.1 km. With no very small particles ($r < r_{min}$), collisions remove objects with $r \approx r_{min}$ at a lower rate, producing the excess of 100–1000 μm satellites. In turn, these objects remove larger particles at a faster rate, creating the large deficit at 1 cm to 10 m. At larger sizes, the waves are due to (i) stochastic collisions among the largest particles, which leads to an intermittent supply of debris among smaller particles and (ii) less frequent destructive collisions among 0.1–10 km particles and 1–100 m particles.

The time scale to set up the equilibrium size distribution is many collision times for the smallest particles. In this example, the collision time for a typical small particle is $vA_d/V \approx 10^4$ yr. The main features of the wavy size distribution develop in just a few collision times, ~ 0.1 Myr. By roughly 1 Myr, $n_{c,rel}$ establishes a distinctive pattern from 100 μm to roughly 10 km, which remains fixed for 1 Gyr. At the largest sizes, fluctuations in the collision rate

[2]In our convention, we have three power law slopes, q (differential power law), q_c (cumulative power law) and q_r (relative cumulative power law). These have a simple relationship: $q \approx q_c + 1 \approx q_r + 3$.

produce a time varying feature which slowly grows with time.

Fig. 10 shows how the depth of the wave depends on the mass of the central planet. In this example, the minimum in $n_{c,rel}$ at 30 μm grows shallower and shifts to smaller sizes with decreasing planet mass. These changes are solely a function of the collision time. With $t_c \propto M_p^{-1/3}$ (eq. 11), a factor of 300 in M_p corresponds to a factor of 6.7 in the collision time. Thus, satellites orbiting a 300 $M_\oplus$ planet experience roughly 7 times as many collisions over a fixed time interval as those orbiting a 1 $M_\oplus$ planet. With fewer collisions, the size distribution of satellites orbiting 1 $M_\oplus$ planets follows the initial power law more closely. Despite the longer collision time, collisions still establish the steep size distribution among the smallest particles and produce clear waves throughout the size distribution.

For any mass of the central planet, the waviness within $n_{c,rel}$ is also sensitive to the cloud mass. Gradually reducing the initial x_d produces the same progression in the depth and position of the deep minimum as in Fig. 10. With $t_c \propto x_d^{-1}$ (eq. 11), factor of 7 reductions in x_d for M_p = 300 $M_\oplus$ yield $n_{c,rel}$ similar to the magenta curve in Fig. 10. With larger reductions, $n_{c,rel}$ more closely resembles the smooth power law of the initial size distribution.

Changing the initial r_{max} has little impact on $n_{c,rel}$ at 0.1–1 Gyr (Fig. 11). For r_{max} = 50–400 km, the normalized size distributions at 100 Myr are essentially identical from 100 μm to 10–20 km. At larger sizes, the deviations from a power law depend on r_{max}.

4.2.2. Size of the smallest particles

For calculations with fixed M_p, x_d, and r_{max}, changing r_{min} has the same impact on $n_{c,rel}$ as changing M_p or x_d (Fig. 12). For the set of parameters in our calculations, collisions between a large particle with radius r_l and a small particle with radius $r_s \ll r_l$ remove 2–3 times the mass of the small particle from the large particle. When r_{min} increases, collisions remove less mass from all remaining particles. Among 0.1 km and larger particles, the smaller mass loss has a fairly small impact on $n_{c,rel}$. However, less mass loss produces a steeper size distribution for particles with $r \approx r_{min}$ and a larger deficit in particles at 10–100 cm. Larger r_{min} also shifts the minimum in $n_{c,rel}$ to larger radii.

When r_{min} decreases, collisions remove somewhat more mass from all particles. The size distribution for the smaller particles becomes less steep and the pronounced minimum at 10–100 cm grows smaller. In our example, calculations with $r_{min} \approx 10$ μm nearly eliminate the deep minimum in $n_{c,rel}$ at 10–100 cm. This example retains the waves in $n_{c,rel}$ for $r \gtrsim$ 1 cm and the steep gradient for $r \lesssim 1$ cm.

4.2.3. Mass of the largest object in the debris

Distributing the mass in the debris differently also has a clear impact on $n_{c,rel}$ at small sizes. In our calculations, all collisions among particles with $r \lesssim$ 1–10 km have $Q_c/Q_D^\star \gtrsim 1$. Both objects shatter. When $b_L \approx 0$, most of the debris is placed in bins with masses close to the mass of the original particles. When $b_L \approx 1$, more debris is distributed among particles with much lower mass. Spreading debris around more mass bins fills in the minimum in $n_{c,rel}$.

Fig. 13 illustrates this point. In calculations with $b_L = 0$, there is a clear minimum in $n_{c,rel}$ at 10–100 cm. When $b_L = 1$, the minimum is less deep; the slope of the size distribution to smaller radii is shallower. At large radii ($r \gtrsim 0.1$ km), b_L has little impact on the $n_{c,rel}$: all relative size distributions are wavy and roughly constant from 0.1–100 km.

In both examples in the figure, the shape of the size distribution is independent of r_{max}. All of the size distributions have small-scale fluctuations about the general trend, but these are small compared to the overall trends as a function of radius.

4.2.4. Binding energy

Reducing $Q_D^\star$ has a similar impact on $n_{c,rel}$ as changing b_L (Fig. 14). Smaller $Q_D^\star$ leads to more ejected mass per collision. More ejected mass enhances the mass excess at the smallest sizes, steepening the size distribution. A larger population of smaller particles enhances the deficit at somewhat larger sizes. As with r_{min}, changing $Q_D^\star$ changes the depth and the location of the deficit. Larger $Q_D^\star$ reduces the deficit and shifts it to smaller sizes. Smaller $Q_D^\star$ adds to the deficit and shifts it to larger sizes.

Reducing $Q_D^\star$ also adds to the waviness of $n_{c,rel}$ at larger sizes. With more mass loss in every collision with much smaller particles, large particles distribute more mass among smaller mass bins. Truncating the size distribution at non-zero r_{min} creates a waviness in this mass loss, which is enhanced as $Q_D^\star$ is reduced.

4.2.5. Initial size distribution

To judge how the size distribution evolves when the calculations start from a monodisperse set of satellites, we consider the baseline model with $r_{min} = 10$ μm instead of 100 μm. The smaller r_{min} give us a better view of the evolution of the population of small particles and yields a good comparison for models with and without an initial size distribution of

particles with radii smaller than r_{max}.

Fig. 15 illustrates the evolution of a baseline model with $M_p = 10\ M_\oplus$ and $r_{max} = 100$ km. At the start of this calculation, collisions between pairs of 100 km objects produce satellites somewhat larger than 100 km and substantial debris. After 0.1 Myr, $n_{c,rel}$ has a clear excess of particles with radii of a few km and some smaller particles. By 1 Myr, the excess has grown considerably; there is a substantial debris tail down to 1 m. In another 9 Myr, the debris populates the full range in allowed particles sizes and establishes a characteristic size distribution which remains fixed for the rest of the calculation.

The equilibrium size distribution in Fig. 15 has the same features as in the baseline model. At small sizes (10 μm to 1 cm), there is a steep and slightly wavy power law with slope $q \approx 4.5$ ($q_c \approx 3.5$; $q_r \approx 1.5$). At larger sizes, the power law slope is closer to $q \approx 2$ with significant waves. Close to r_{max}, the slope again steepens.

Fig. 16 compares snapshots of the size distribution for calculations with ('sd') and without ('no sd') an initial power law size distribution among particles with radii smaller than r_{max}. At 10 Myr, calculations with a mono-disperse set of large particles have more mass. In these calculations, the largest particles lose less mass through collisions with much smaller objects. Thus, they diminish in size less rapidly with time. For particles which are large enough to escape destruction, the extra mass in the largest particles allows them to grow more rapidly.

At 1 Gyr, the $n_{c,rel}$ for 10 μm to 30–50 km particles is independent of the initial size distribution. In the 'no sd' models, the largest objects reach sizes of 200–300 km in 1 Gyr. Satellites in the 'sd' models gradually lose mass and reach sizes of 70 km after 1 Gyr. Despite this difference, smaller debris particles produced in the collisions of the largest objects have an identical size distribution. Thus, the long-term evolution of the smallest objects is independent of the starting point.

4.3. Evolution of the Cross-sectional Area

For Fomalhaut b, observations cannot measure the size of the largest object or discern the size distribution across any range of sizes. Aside from the size and the color of the cloud as a whole, the only observable is the total brightness. For grains with radii $\gtrsim 10$ μm, we relate the brightness to the cross-sectional area (e.g., Currie et al. 2013; Galicher et al. 2013; Kalas et al. 2013; Kenyon et al. 2014). To compare model results with the observations, we rely on the time variation of the cross-sectional area in each calculation relative to the adopted area for Fomalhaut b, $A_d \approx 10^{23}$ cm^2. A successful calculation matches this area at

the adopted age of Fomalhaut, $t_F \sim 200$ Myr. We assign a factor of two uncertainty to A_d and t_F. The model 'target' is then a rectangular box in (t_F, A_d) space (see also Fig. 1).

4.3.1. Baseline model

Fig. 17 illustrates the time variation of A_d for baseline models with initial r_{max} = 400 km. Initially, the surface area – $A_d \propto M_d \propto x_d M_p$ – depends only on the initial cloud mass. Collisions then redistribute mass through the grid and gradually change the relative surface area. From eqs. 11 and 12, the collision time is $t_c \propto M_p^{2/3} M_d^{-1}$. For fixed x_d, swarms around more massive planets have larger cloud masses and shorter t_c. Thus, calculations with M_p = 100–300 $M_\oplus$ evolve more rapidly than those with M_p = 1–3 $M_\oplus$. After a brief re-adjustment where A_d grows substantially, the relative surface area declines from ~ 100 (where the swarm may become optically thick, see the discussion in §5.1.2 below) at 1 Myr to ~ 1 at 1 Gyr. Although the 100 $M_\oplus$ models graze the target box at 400 Myr, these models generally fail to match the observations.

Calculations with M_p = 1–3 $M_\oplus$ also fail. These models begin with relative surface areas close to the target and fairly long collisions times of 20–30 Myr. However, the largest objects in these calculations grow with time, removing small particles from the grid. After 100 Myr of evolution, swarms of satellites orbiting 1–3 $M_\oplus$ planets have relative surface areas at least a factor of two below the observations.

Swarms of satellites around 10–30 $M_\oplus$ planets match the observations throughout the 100–400 Myr target period. In these systems, the initial cross-sectional area is roughly 10–20 times the area of Fomalhaut b. Although the largest objects in these simulations also grow with time, debris from the collisions of smaller objects maintains a large surface area for over 100 Myr. After 400 Myr (1 Gyr), satellites around the 10 $M_\oplus$ (30 $M_\oplus$) planet have a surface area smaller than Fomalhaut b. Thus, there is a substantial cushion between the predicted time evolution and the evolution required to match the observations.

Calculations starting with smaller r_{max} yield smaller cross-sectional area at late times (Fig. 18). With fixed total mass, swarms with smaller initial r_{max} have larger surface area ($A_d \propto r_{max}^{-1/2}$). However, the collision time scales linearly with r_{max} (eq. 11). Thus, destructive collisions remove material more rapidly from swarms with smaller r_{max}. More rapid mass loss results in smaller cross-sectional area. For M_p = 30 $M_\oplus$, simulations with initial r_{max} = 100–200 km still match the observations at 200 Myr. Satellites with initial r_{max} = 50 km fall below the target.

When $r_{max} \lesssim 200$ km, calculations with M_p = 10 $M_\oplus$ also fail to match the observations.

Collisional evolution is too rapid for these models to match the observed surface area at 100–400 Myr. In contrast, models with more massive planets, $M_p = 100$–$300\ M_\oplus$, and $r_{max} =$ 100–200 km, pass through the target. However, swarms with $r_{max} = 50$ km succeed only for $M_p = 100\ M_\oplus$.

4.3.2. Initial cloud mass

The initial cloud mass has a more dramatic impact on the evolution of the surface area than r_{max}. For fixed M_p, the collision time scales inversely with x_d and r_{max}. Smaller x_d and smaller r_{max} lengthen the collision time. However, the initial surface area scales linearly with x_d and as $r_{max}^{-1/2}$. Models with smaller x_d therefore start out with much smaller area and have more trouble matching observations.

Fig. 19 illustrates these points for $M_p = 10\ M_\oplus$ and $r_{max} = 400$ km. The baseline model with $x_d = 0.01$ matches the data for ages of 100–400 Myr. Factor of ten smaller swarms have an initial surface area somewhat larger than Fomalhaut b, but collisions reduce the area by almost a factor of ten after 100 Myr. Another factor of ten reduction in x_d leaves the surface area below observations throughout the evolution of the swarm.

Fig. 20 shows that low mass swarms around massive planets can also match observations. When $M_p = 100\ M_\oplus$, satellites with $x_d = 0.01$ have a surface area that grazes the upper edge of the target box at 300–400 Myr. Reducing the initial mass by a factor of 100 yields a surface area that grazes the lower edge of the target box at 100–200 Myr. Intermediate cloud masses match the data well; models with $x_d = 0.001$ pass through the upper middle of the target box.

4.3.3. Size of the smallest particles

In the analytic model, the surface area of a satellite swarm scales with $r_{min}^{-1/2}$. Changing r_{min} by an order of magnitude thus modifies the initial surface area by a factor of ~ 3. Because r_{min} has little impact on the cloud mass or the collision time, the early evolution of satellites with different r_{min} is nearly identical. Over time, however, the smallest particles shape the size distribution at larger sizes (Fig. 12). When r_{min} is smaller (larger), more (fewer) intermediate particles with $r \approx 10$ cm to 10 m survive the cascade. If these particles contribute much to the total surface area of the swarm, then we expect the surface area at late times to scale more steeply with the minimum particle size.

Fig. 21 demonstrates that transformations to the size distribution have little impact on

the evolution of the surface area. In the baseline model with $M_p = 10\ M_\oplus$, $r_{max} = 200$ km, and $r_{min} = 100\ \mu$m, the evolution of the surface area passes through the lower left corner of the target area. In calculations with $r_{min} = 1$ mm, the surface area is $\sqrt{10}$ smaller and falls well below the target. Factor of ten smaller r_{min} yields a factor of $\sqrt{10}$ larger surface area which lies in the upper half of the target. Thus, the surface area scales exactly as $r_{min}^{-1/2}$.

Despite significant differences in the size distributions of calculations with different r_{min}, these changes have little impact on the evolution of the surface area. Particles with radii of 1 cm to 100 m have a limited fraction of the mass of the larger particles and a negligible surface area compared to much smaller particles. Augmenting (or reducing) the population of these particles by factors of 100–1000 has no observable impact on the total surface area of the cloud.

4.3.4. Mass of the largest object in the debris

In our collision model, we use a simple algorithm to distribute debris into the mass bins. For the baseline model with $b_L = 0$, the largest object in the debris has 20% of the total mass in the debris. In comparison models with $b_L = 1$, larger relative collision energies place more material in lower mass bins. Material leaves the grid more rapidly. Although the distribution of debris has little impact on the evolution of the largest objects (Fig. 6), the relative number of the smallest particles depends on the mass of the largest object in the debris (Fig. 13). In the complete ensemble of calculations, $N(r_{min})$ changes by a factor of 3–5; we expect similar changes in the cross-sectional area.

Fig. 21 confirms this conjecture for calculations with $M_p = 10$–$30\ M_\oplus$, $x_d = 0.01$, r_{max} = 400 km, and $r_{min} = 100\ \mu$m. When $b_L = 0$, the predicted surface area passes through the target box. For $b_L = 1$, calculations with $M_p = 30\ M_\oplus$ pass through the lower edge of the target; models with $M_p = 10\ M_\oplus$ completely miss the target.

Larger b_L allows satellite swarms around more massive planets to match observations at 100–400 Myr. In the baseline model, calculations with $M_p = 100$–$300\ M_\oplus$ and $x_d = 0.01$ have much larger surface area than Fomalhaut b. When $b_L = 1$, satellites orbiting planets with $M_p = 100\ M_\oplus$ ($300\ M_\oplus$) pass through the lower (upper) half of the target box.

4.3.5. Binding energy

In our suite of calculations with different $Q_D^\star$, smaller $Q_D^\star$ prevents the largest objects from growing (Fig. 7). The additional debris produced from collisions between the largest

objects decreases the relative numbers of satellites with radii larger than 1–10 cm (Fig. 15). However, smaller $Q_D^\star$ has little impact on the relative population of the smallest objects which dominate the cross-sectional area. Thus, swarms of satellites with different binding energies have comparable surface areas.

Fig. 22 shows the modest variations in cross-sectional area for calculations with different $Q_D^\star$. In the baseline model, 400 km satellites reach radii of 2000 km on time scales of 100–400 Myr. Large fluctuations in the surface area resulting from stochastic variations in debris production from the collisions of the largest objects begin at 100 Myr and continue beyond 1 Gyr. Lowering $Q_D^\star$ by a factor of two limits the growth of these objects to 1000 km. Slower growth delays the large oscillations in the surface area and minimizes them at later times. Another factor of two reduction in $Q_D^\star$ completely eliminates the growth of the largest objects. Less growth enables more debris and larger surface area at early times. As the calculation proceeds, debris production is somewhat more modest than calculations with larger $Q_D^\star$, resulting in a slightly lower surface area at later times.

In calculations with $b_L = 1$, smaller $Q_D^\star$ speeds up the time evolution of the surface area. When $Q_D^\star$ is smaller and $b_L = 1$, collisions place more debris in smaller mass bins. Placing debris in smaller mass bins allows the cascade to eject mass from the grid more rapidly. Thus, the surface area declines more rapidly with time. For the smallest $Q_D^\star$ considered in our calculations, models with $b_L = 1$ require very large and probably unrealistic initial cloud masses to match the target for Fomalhaut b.

4.3.6. Initial Size Distribution

When calculations begin with an initial power-law size distribution, the initial surface area is substantial (Fig. 17). With a mono-disperse set of large particles, the initial surface area is negligible. For $r_{max} = 100$ km and $r_{min} = 100$ μm, it takes several collision times to populate the low mass end of the size distribution (Fig. 16) and increase the surface area.

Fig. 23 compares the growth of the surface area for swarms of satellites with ('sd') and without ('no sd') an initial power-law distribution of small particles. When $r_{max} = 100$ km, the collision time is rather short. It takes only a few $\times$ 10^6 yr for the surface area to reach the levels of the baseline model. At 10 Myr, the satellite swarm in the mono-disperse model has relatively more small particles than the swarm with the initial power-law size distribution (Fig. 16). Thus, the mono-disperse model has a larger surface area. By $\sim$ 1 Gyr, collisions have erased the starting conditions; the size distributions (and hence the surface areas) are indistinguishable.

When the initial r_{max} is 400 km, the evolution of satellite swarms with and without an initial power law size distribution diverge. In these calculations, the collision time is much longer. Populating the small end of the size distribution takes 30–40 Myr instead of 3–6 Myr. With fewer small objects to chip away at the mass of the largest objects, the largest objects grow more rapidly and contain a larger fraction of the initial mass (Fig. 8). At $\sim$ 100 Myr, these calculations produce more debris than the baseline model. As the evolution proceeds, the larger mass tied up in the largest objects speeds up the decline of the population of small particles. After 400–500 Myr, the surface area in the small particles is a factor of $\gtrsim 2$ smaller than in the baseline model.

4.4. Growth of Very Large Objects in the Swarm

In some calculations, the largest objects in the swarm grow by factors of 10–1000 in mass over 0.1–1 Gyr. As these objects grow, their gravity may stir up smaller objects in the swarm. Small amounts of stirring increase typical collision velocities and enhance the impact of the collisional cascade. Larger amounts can eject material from the swarm. Aside from ejections, dynamical interactions between pairs of very large objects can place satellites on bound orbits closer to the planet. If the planet already has a set of closely bound satellites, a 'new' satellite might disrupt the indigenous satellite system.

To explore the impact of these processes within our simulations, we begin with general principles. When large satellites grow, they try to stir up smaller satellites to their escape velocity. Satellites with radii r_{max} have escape velocity

$$v_{esc} = 0.9 \left(\frac{r_{max}}{10^3 \text{ km}} \right) \text{ km s}^{-1} \quad . \tag{17}$$

For a central planet with $M_p = 10\ M_\oplus$, satellites with $r_{max} \approx$ 350–400 km have an escape velocity, 0.3 km s^{-1}, comparable to the collision velocity of satellites in a spherical swarm. Thus, stirring is a crucial issue for large satellites with radii of 1000–2000 km.

Satellites orbiting the planet have Hill spheres where the gravity of the satellite dominates the gravity of the planet. For satellites orbiting at semimajor axis a, the Hill radius is $R_{H,s} \approx r_s a$ (e.g., eq. 5) where

$$r_s \approx 0.04 \left(\frac{r_{max}}{1000 \text{ km}} \right) \left(\frac{M_p}{10\ M_\oplus} \right)^{-1/3} \quad . \tag{18}$$

Larger satellites around less massive planets have larger Hill radii.

When the semimajor axes of orbiting satellites differ by 3–4 Hill radii or less, they interact dynamically. For simplicity, we define the minimum orbital separation for stability

as $\Delta a \approx 4 r_s a$. In a system of N massive satellites within a spherical shell of width $\delta a = \eta_2 a$, the system is dynamically stable when $4 N r_s a \lesssim \eta_2 a$. Solving for N, the maximum number of non-interacting satellites is

$$N_{max} \approx 3 \left(\frac{\eta_2}{0.5} \right) \left(\frac{r_{max}}{1000 \text{ km}} \right)^{-1} \left(\frac{M_p}{10 \ M_\oplus} \right)^{1/3} \ . \tag{19}$$

When satellites orbit massive planets with $M_p \gtrsim$ 1–300 $M_\oplus$, large-scale dynamical interactions require a few satellites with $r_{max} \gtrsim$ 1000 km. For fixed r_{max}, dynamical interactions are more common around less massive planets.

In our suite of calculations, stirring of smaller satellites by the largest satellites is a relatively minor issue. For objects within the collisional cascade, the initial collision velocities produce shattering. Larger relative velocities produce a little more debris and a somewhat faster decline in the relative surface area of small particles. Larger objects are already immune to the cascade; larger relative collision velocities have little impact on their evolution.

Dynamical interactions among n-bodies are more important. As one example, Fig. 25 tracks the time evolution of the semimajor axes for a set of n-bodies orbiting a 1 $M_\oplus$ planet. In this calculation, the initial set of 400 km objects grows throughout the evolution of the satellite swarm (Fig. 2). At $\sim$ 60 Myr, the coagulation code promotes the first satellite into the n-body code with a circular, but highly inclined, orbit at 0.15 AU. Roughly 10 Myr later, a second n-body appears with an orbit at 0.18 AU. Within another 5 Myr, a third n-body has an orbit at 0.21 AU. At 100 Myr, the separations of these satellites are roughly 3.5 mutual Hill radii. Strong dynamical interactions are inevitable. A scattering event between the outer two satellites places one on a very close orbit with the inner satellite. All develop eccentric orbits. Eventually, the more massive inner satellite ejects the other two satellites and ends up on an eccentric orbit much closer to the planet.

In this suite of calculations, the dynamical evolution of the n-bodies has no impact on satellites remaining in the coagulation code. A few larger objects continue to grow. Promotion of two of these satellites into the n-body code leads to another set of dynamical interactions at 200 Myr, where the two new (and lower mass) n-bodies are ejected and the original massive n-body moves a little closer to the planet. One last satellite promoted into the n-body code at $\sim$ 500 Myr orbits on a circular, highly inclined orbit well away from the inner massive satellite. This system remains stable for the rest of the calculation.

At the end of this calculation, roughly 33% of the initial mass in solids remains in orbit around the planet. Nearly all of this material is in the two large satellites orbiting at 0.05 AU and 0.19 AU. Dynamical interactions (44% $\pm$ 7%) and radiation pressure (56% $\pm$ 6%) eject equal amounts of material. Despite this rough equality in mass, radiation pressure removes

100 μm particles from the grid. Dynamical interactions place four Pluto-mass planets into orbits around the central star.

This evolution of large objects is fairly typical. Roughly half of the simulations with growing n-bodies leave massive satellites orbiting the planet. Nearly 15% of these have satellites orbiting at semimajor axes well inside the initial extent of the satellite swarm. Less than 5% have satellites outside the initial boundary of the swarm. In the rest, 1–2 satellites orbit stably within the swarm.

4.5. Comparing the Analytic and Numerical Models

Compared to the analytic model, the numerical simulations yield several clear differences in the collisional evolution of a satellite swarm. The sizes of the largest objects change considerably in 0.1–1 Gyr. When catastrophic and cratering collisions dominate, r_{max} declines by 30% or more. The largest objects then have roughly 30% of the mass of the largest objects in an analytic model where r_{max} is constant in time.

In some systems, the largest satellites grow substantially. Left unchecked, this growth yields massive objects capable of disrupting the satellite swarm (and perhaps satellite systems closer to the planet). Swarms orbiting lower mass planets are more prone to this evolution than swarms around more massive planets.

The size distribution does not follow a simple power law. Although the numerical simulations roughly follow this power law for satellites with $r \gtrsim 0.1$ km, all of these models produce large (factor of 3–5) waves about the power law. At small sizes, there is a large deficit in 0.1 cm to 10–30 m particles relative to the analytic power-law. In calculations with an initial power-law size distribution, smaller r_{min} and larger b_L reduce the size of the deficit. Calculations starting with a mono-disperse size distribution also yield smaller deficits.

The smallest particles with $r \lesssim 0.1$ cm follow a steep power law with $q \approx 4$–5. In our simulations, the lack of particles with $r < r_{min}$ limits mass loss among larger particles. When these particles lose mass less rapidly, they stay in the grid for longer periods of time, steepening the size distribution.

Despite these differences, the time evolution of the surface area in the baseline model (Fig. 17) is similar to the time evolution of the analytic model (Fig. 1). In the analytic model, satellite swarms orbiting 10 $M_\oplus$ planets evolve through the middle of the target. Swarms around 30 $M_\oplus$ planets have a surface area in the upper half of the target box. Swarms orbiting smaller (3 $M_\oplus$) or larger (30 $M_\oplus$) planets have areas that graze or just miss

the target. In the baseline numerical model, satellites orbiting 10–30 $M_\oplus$ planets match the observations. Swarms around 3 $M_\oplus$ or 100 $M_\oplus$ planets fall below or graze the upper edge of the target. Overall, the numerical simulations require slightly more massive planets to match the observations than the analytical models.

Fig. 26 compares the evolution of the mass in a baseline model with the predictions of the analytic model using three different values for the correction factor α. For $M_p = 10\ M_\oplus$, $x_d = 0.01$, $r_{max} = 100$ km, and $r_{min} = 100\ \mu$m, the mass in the numerical model begins to decline at 0.1 Myr. It takes 40–50 Myr for the mass to reach 10% of the initial mass and 700–800 Myr to reach 1% of the initial mass. At late times, the mass evolves with time as $M(t) \propto t^{-n}$ and $n \approx 0.8$–0.9. Thus, the mass declines somewhat less rapidly than in the analytic model.

In the analytic model, the mass loss rate is initially smaller than in the numerical model. As time proceeds, analytic models with $\alpha = 0.333$ (3.333) decline more rapidly (slowly) than the numerical model. When $\alpha = 1$, the analytic and numerical models match at 20–30 Myr. After this time, the t^{-1} decline of the analytic model results in a faster rate of mass loss than the numerical model.

For comparisons between the analytic model and the complete suite of numerical simulations, the 'best' α depends on the input parameters. For all models with the baseline set of parameters, $\alpha \approx 1$. Changing x_d, r_{min}, $Q_D^\star$, and the initial size distribution has little impact on α. When $b_L \approx 1$, the faster removal of material in the grid leads to more rapid evolution and smaller $\alpha \approx 1/2$ to 1.

5. DISCUSSION

Our suite of simulations paints an interesting picture for the evolution of swarms of satellites orbiting 1–300 $M_\oplus$ planets at 120 AU from a central 1.9 $M_\odot$ star. Depending on M_p, x_d, and r_{max}, the masses of the largest satellites grow or shrink with time. Satellites with large $Q_D^\star$ grow; satellites with small $Q_D^\star$ shrink. Clouds with smaller x_d and larger r_{max} evolve more slowly. Outcomes are insensitive to r_{min}, the shape of the initial size distribution, or the algorithm for distributing debris among the mass bins.

However the largest objects evolve, the cumulative size distribution transforms into a standard shape which is fairly independent of the input parameters. This standard shape has three distinct pieces: (i) a steep power law with $n(> r) \propto r^{-q_c}$ and $q_c \approx 4$ ($q_r \approx 2$) for small particles ($r \lesssim 10$–30 cm), (ii) a flat portion where $q_c \approx 0 - -1$ ($q_r \approx -2$ to -1) for intermediate size particles ($r \approx 30$ cm to 0.1 km), and (iii) a shallow, wavy power law

with $q_c \approx 1$–2 ($q_r \approx -1$ to 0) for large particles ($r \gtrsim 0.1$ km). The development of this standard shape depends on the collision time: swarms with longer collision times take longer to establish this size distribution.

Despite the diverse outcomes, a broad set of satellite swarms produce a cross-sectional area which matches the observed area in Fomalhaut b. For models with the nominal r_{min}, $Q_D^\star$, and b_L, Fig. 27 summarizes these outcomes a function of M_p, r_{max}, and x_d. Swarms orbiting low mass planets always fail. Satellites around more massive planets are often successful. Successful models have a factor of 2–3 range in the initial mass in satellites relative to a 'best' model with an initial mass of $\sim 10^{27}$ g.

Aside from the initial mass, the size of the smallest stable particle orbiting the planet and the mass distribution of debris from a collision establish the ability of a model to match the observed cross-sectional area. If particles with $r_{min} = 10$ μm can stably orbit the planet, smaller initial cloud masses are possible. Larger r_{min} and $b_L > 0$ reduce the grid of successful models.

5.1. Theoretical Issues

In these coagulation calculations, the standard size distribution has several features in common with results for debris disks orbiting main sequence stars. There are also a few major differences. In addition, several uncertain parameters establish whether model satellite swarms have cross-sectional areas at 100–400 Myr comparable to the observed area in Fomalhaut b. Assigning different values for r_{min}, $Q_D^\star$, and b_L allows swarms with different combinations of M_p, x_d, and r_{max} to match the observations. Here, we discuss features of the size distribution and consider the flexibility of the theory in setting the various input parameters and the likely consequences of our choices.

5.1.1. Size Distribution

In Figs. 9–16, the size distributions derived in our calculations are radically different from the smooth power law, $n(r) \propto r^{-q}$ with $q \approx 3.5$–3.7, expected from an equilibrium collisional cascade (Dohnanyi 1969; O'Brien & Greenberg 2003; Kobayashi & Tanaka 2010). The general trend of $n(r)$ is much shallower than this power law. Pronounced waves are superposed on this general trend.

Wavy size distributions are a common feature in numerical calculations of debris disks orbiting 1–3 $M_\odot$ stars (e.g., Campo Bagatin et al. 1994; O'Brien & Greenberg 2003; Thébault et al.

2003; Krivov et al. 2006; Löhne et al. 2008; Gáspár et al. 2012; Kral et al. 2013). These waves have two typical sources: the low mass cutoff of the size distribution and the transition between the bulk strength and gravity regimes in analytic expressions for $Q_D^\star$ (see eq. 4). Although the amplitudes (in $n(r)$) of the waves depend on the radius of the low mass cutoff, the ratio $Q_c/Q_D^\star$, and the parameters in the relation for $Q_D^\star$, typical values are a factor of 10 or smaller.

By typical debris disk standards, the waves in Figs. 9–16 are somewhat extreme. For our calculations, the positions and relative spacing of minima and maxima follow general predictions from analytic models (e.g., O'Brien & Greenberg 2003). Factor of 3–10 amplitudes at 0.1–100 km are also normal. However, the amplitudes of waves at small sizes are 10–1000 times larger than those reported from numerical simulations of debris disks.

The long-term collisional evolution of satellite swarms is responsible for this difference. Compared to debris disks around stars, satellite swarms orbiting planets are much more collisionally evolved (e.g., Bottke et al. 2010). More collisional evolution enhances the excess of particles with $r \approx 1$–$10\ r_{min}$ and the deficit of particles with $r \approx 10$–$100\ r_{min}$. As a result, the amplitude of the wave simply grows larger and larger with time. Fig. 10 clearly shows the impact of longer collisional evolution: massive systems with shorter collision times have much stronger waves than low mass systems with longer collision times.

5.1.2. The minimum particle size

In the baseline model, r_{min} is the blowout radius r_b for a 10 $M_\oplus$ planet. The slow variation of r_b with M_p justifies this assumption for all M_p (eq. 9). However, radiation pressure cannot remove small particles when (i) the collision time is comparable to or shorter than the orbital period around the planet and (ii) the optical depth of the cloud is one or larger. If satellite swarms meet either of these conditions, smaller particles stably orbit the planet.

The optical depth τ of the cloud is roughly the ratio of A_d to the cross-sectional area defined by the physical extent of the swarm $A_s = \pi(\eta_1 R_H)^2$. Setting $\tau = A_d/A_s$ and adopting the nominal parameters,

$$\tau \approx 9 \times 10^{-4} \left(\frac{\eta_1}{0.2}\right)^{-2} \left(\frac{M_p}{10\ M_\oplus}\right)^{-2/3} \left(\frac{M_\star}{2\ M_\odot}\right)^{2/3} \left(\frac{a_p}{120\ \mathrm{AU}}\right)^{-2} \left(\frac{A_d}{10^{23}\ \mathrm{cm}^2}\right) . \qquad (20)$$

For planets with $M_p \lesssim 30\ M_\oplus$, satellite swarms have $A_d \lesssim 10^{25}$ cm^2 throughout their evolution. These swarms are never optically thick. Early in the evolution of swarms orbiting more massive planets, $A_d \gtrsim 10^{26}$ cm^2; these swarms are optically thick.

For a single small particle, it is straightforward to derive the ratio ξ of the collision time to the orbital period. The collision time is roughly $t_c \approx V/vA_d$; the orbital period is $T = 2\pi a/v$. The ratio is then:

$$\xi \approx 1.85 \times 10^2 \left(\frac{\eta_1}{0.2}\right)^2 \left(\frac{\eta_2}{0.5}\right) \left(\frac{M_p}{10\ M_\oplus}\right)^{2/3} \left(\frac{M_\star}{2\ M_\odot}\right)^{-2/3} \left(\frac{a_p}{120\ \mathrm{AU}}\right)^2 \left(\frac{A_d}{10^{23}\ \mathrm{cm}^2}\right)^{-1} \quad . \quad (21)$$

Around low mass planets with $M_p \lesssim 10\ M_\oplus$, the initial cross-sectional area of the swarm is $\lesssim 10^{24}$ cm^2. Radiation pressure removes small particles faster than collisions. Among more massive planets, $A_d \gtrsim 10^{26}$ cm^2 for $t \lesssim 1$ Myr. High speed collisions destroy small particles faster than radiation pressure removes them. The smallest particles in the swarm are then much smaller than 100 μm. Although the cross-sectional area of these swarms is then formally very large, the observed area is limited by the optical depth. With $\tau \approx 1$, the maximum area is roughly 10^{26} cm^2.

This discussion implies that r_{min} is rarely smaller than the nominal blowout size r_b. Early in the evolution of satellite swarms around massive planets, particles with sizes smaller than 10–100 μm remain bound. This phase is short-lived, ~ 1 Myr. As these systems evolve, A_d declines rapidly as r_{min} returns to its nominal value. The evolution then continues as outlined in §4.3.

5.1.3. The particle strength

The binding energy of solid particles establishes collision outcomes. When the collision energy Q_c exceeds the binding energy $Q_D^\star$, more than half of the mass of the colliding pair of particles ends up in debris. In circumstellar disks, collisional damping and gravitational interactions between particles often limit the impact of $Q_D^\star$ on the evolution (e.g., Kenyon & Bromley 2008, 2010). For satellite swarms within a spherical shell, damping and gravitational interactions are minimal. With Q_c solely a function of η_1 and M_p, the growth of the largest particles is a strong function of $Q_D^\star$.

For icy objects with sizes much larger than 1 cm, astronomical observations, laboratory experiments, and numerical simulations paint a disparate picture for $Q_D^\star$. Recent experiments colliding cm-sized icy solids in the lab suggest tensile strengths of roughly 10^6 erg g^{-1} (e.g., Shimaki & Arakawa 2012; Yasui et al. 2014), which agrees with previous results (e.g., Ryan et al. 1999). Numerical simulations of high speed collisions between icy objects are the basis for the expression in eq. 4 (Benz & Asphaug 1999; Leinhardt & Stewart 2009). Typically, $Q_b \approx 10^5 - 10^8$ erg cm$^{0.4}$ g^{-1} and $Q_g = 0.1$–2 erg cm$^{1.65}$ g^{-1}. For $r \approx 1$–10 cm, the simulations suggest a binding energy of roughly 10^6 erg g^{-1}. Experiments and simulations

agree on the strength for small objects.

Observations of comets yield much smaller binding energies. Models for comet D3/1993 F2 (Shoemaker-Levy) and other disrupted comets suggest binding energies of 1–10^3 erg g^{-1} (e.g., Asphaug & Benz 1996; Richardson et al. 2007; Skorov & Blum 2012). Data from Deep Impact imply a strength in the middle of this range (e.g., Holsapple & Housen 2007; A'Hearn 2011). With $r \approx 0.1$–1 km for the nuclei of these comets, the maximum strength of 10^3 erg g^{-1} is a factor of 10 or more smaller than expected from eq. 4 and the results from laboratory and numerical experiments.

Our adopted values for the parameters in $Q_D^\star$ lie intermediate between observations and numerical simulations. Values for $Q_D^\star$ similar to results from the studies of comets preclude the growth of large satellites around planets with $M_p = 1$–$30\ M_\oplus$ (see Fig. 2). More material then participates in the collisional cascade. Although evolution times are somewhat shorter, the evolution of the cross-sectional area is unchanged. Thus, significantly smaller $Q_D^\star$ does not change our conclusions.

Larger values for $Q_D^\star$ enhance the growth of large satellites around all planets. For sufficiently large $Q_D^\star$ as in Benz & Asphaug (1999), the collisional cascade is limited. Few satellite swarms have sufficient surface area to match observations of Fomalhaut b. In these systems, the largest satellites probably grow large enough to disrupt the satellite swarm completely (see §4.4). Then, all models fail: none match observations of Fomalhaut b.

5.1.4. The size of the largest particle in the debris

Theory currently provides limited guidance on $m_{max,d}$, the mass of the largest particles in a cloud of debris ejected during a high velocity collision. For cratering collisions, m_{esc} is a simple function of the collision energy and the gravity of the planet (e.g., Housen & Holsapple 2011; Svetsov 2011). However, there are no direct calculations of $m_{max,d}$. Wetherill & Stewart (1993) examined laboratory data and adopted the simple relation $m_{max,d} = 0.2 m_{esc}$ used in our baseline model. Recent experiments confirm this choice (e.g., Burchell et al. 2005; Poelchau et al. 2014, and references therein).

For catastrophic impacts, numerical simulations provide somewhat conflicting advice for $m_{max,d}$. In Leinhardt & Stewart (2012), collisions of 1–10 km icy objects yield a broad range, $m_{max,d}/m_{esc} \approx 0.001$–1. Power-law fits to the distribution of debris particles require assigning either a lower bound to the size of a debris particle or a slope to the size distribution. Choosing the slope leads to a fixed value $m_{max,d}/m_{esc} \approx 0.026$ independent of $Q_D^\star$.

Durda et al. (2004, 2007) describe numerical simulations of collisions for 10–100 km rocky objects. In these simulations, the mass of the largest object within the debris is 1–2 orders of magnitude smaller and very sensitive to the ratio of Q_c to $Q_D^\star$ (Morbidelli et al. 2009; Bottke et al. 2010). These calculations predict much steeper size distributions than those of Leinhardt & Stewart (2012). However, including these results in coagulation codes requires adopting a shallow slope for small sizes to conserve mass which introduces additional input parameters.

For high velocity collisions of small objects, laboratory experiments suggest the mass in the largest debris particle scales roughly inversely with the ratio of the collision energy to the binding energy (e.g., Arakawa 1999; Arakawa et al. 2002; Shimaki & Arakawa 2012). Available data imply larger particle sizes for collisions between more porous and stronger targets.

Our approach to placing debris in mass bins roughly follows the spirit of Leinhardt & Stewart (2012). In our baseline model, debris from cratering collisions agrees with experimental results; the mass of the largest object in catastrophic collisions is roughly 10 (Leinhardt & Stewart 2012) to 100 (Bottke et al. 2010) times larger than inferred from numerical simulations. Compared to the predictions of numerical collision codes, these calculations probably underestimate the rate of decline for the cross-sectional area around massive planets. In models with $b_L = 1$, catastrophic collisions yield results more similar to Leinhardt & Stewart (2012). Although this treatment of cratering collisions leaves too much mass in large objects, most collisions are catastrophic. Thus, the cratering algorithm has little impact on our results.

Adopting the Bottke et al. (2010) treatment of $m_{max,d}$ speeds up the collisional cascade. When the debris evolves more rapidly, swarms orbiting 10–30 $M_\oplus$ planets cannot match the observed surface area of Fomalhaut b for ages of 100–400 Myr. However, more rapid evolution for swarms around 100–300 $M_\oplus$ planets allows these systems to match the observations.

5.2. Predictions for Fomalhaut b and Other Exoplanetary Systems

Two aspects of our calculations allow tests from existing observations of Fomalhaut b or new observations of other debris disks. All collisional cascade models predict a mass loss rate from the production of particles with sizes less than the size of the smallest stably orbiting particle (e.g., Kobayashi & Tanaka 2010). Most of these particles should lie close to the orbit of the planet around the central star (e.g., Kenyon et al. 2014). Numerical results for this mass loss rate at 100–400 Myr yield an expected surface brightness along the path of Fomalhaut b. For younger systems, the mass loss rate and the cross-sectional area of

the swarm are much larger. For sufficiently large A_d, satellite swarms are detectable around stars with ages of 1–10 Myr.

To quantify our first prediction, we consider baseline models of satellite swarms orbiting 10–100 $M_\oplus$ planets. At 100–200 Myr, the mass loss rate in small particles is $0.6 - 3 \times 10^{18}$ g yr^{-1}. For particle sizes of 100 μm, mass loss leaves behind a trail with a cross-sectional area of roughly 10^{20} cm^2 every year. Fomalhaut b has an orbital period of roughly 1000 yr. Every orbit, mass loss produces a ring of material with a cross-sectional area comparable to the observed A_d of Fomalhaut b.

The total surface area of this ring depends on the long-term evolution of small particles. If the particles have a velocity dispersion similar to their escape velocity from the planet, they have orbits with eccentricity $e \approx 0.1$ around Fomalhaut. Interactions with Fomalhaut b are probably rare. With inclinations $i \approx e/2$, the collision time for a single 100 μm particle is roughly 1 Gyr for $A_d \approx 10^{23}$ and 1 Myr for $A_d \approx 10^{26}$ cm^2. With roughly 1 Myr required to eject particles with $A_d \approx 10^{26}$ cm^2, we envision an approximate steady-state where ejections of 100 μm particles from Fomalhaut b roughly balance particles lost from destructive collisions.

To estimate the surface brightness of this ring, we consider bound orbits along a ring with semimajor axis $a \approx 120$ AU, width $\delta a \approx 0.1\ a$, and $e \approx 0.8$ (e.g., Beust et al. 2014). Along this ring, there are roughly 10^4 resolution elements on HST images (Kenyon et al. 2014). With $A_d \approx 10^{26}$ cm^2, each resolution element has a cross-sectional area of 10^{22} cm^2 in 100 μm particles.

If the orbit of Fomalhaut b is stable on Myr time scales, tracing a ring of dust along this orbit is challenging (e.g., Currie et al. 2012; Galicher et al. 2013; Kalas et al. 2013). However, comparing the average surface brightness of coadded pixels along the orbit with similarly coadded pixels 20–30 AU away should yield a clear measure of the surface brightness along the ring and a strong test of the model.

To make predictions for the brightness of satellite swarms orbiting any star, we consider f_o the observed flux of the swarm relative to $f_\star$ the observed flux from the central star (see also §2.3 of Kenyon et al. 2014). For a swarm with optical depth τ and scattering efficiency Q_s, $f_o/f_\star = Q_s A_d / 4\pi a_p^2$. We set $A_d = \tau A_s = \tau\pi(\eta_1 r_H a_p)^2$ with $\eta_1 = 0.2$. Defining $\Delta m = -2.5 \log (f_o/f_\star)$, the predicted contrast between the satellite swarm and the central star is

$$\Delta m \approx 15.83 - 2.5 \log \tau - 5 \log \left(\frac{\eta_1}{0.2}\right) - 1.67 \log \left(\frac{M_p}{10\ M_\oplus}\right) + 1.67 \log \left(\frac{M_\star}{1\ M_\odot}\right) . \quad (22)$$

Although the contrast depends on τ, η_1, M_p, and $M_\star$, it is formally independent of the

semimajor axis of the planet and the distance to the star. However, swarms with $\tau \approx 0.1$–1 have longer lifetimes at larger a; thus, observations are more likely to detect bright swarms at 100 AU than at 10 AU.

Among nearby associations of young stars, the β Pic moving group provides the best testing ground for this prediction. With ~ 30 members having V $\approx$ 4–9, $d \approx 20$ pc, and ages ~ 20 Myr (Zuckerman et al. 2001; Mamajek & Bell 2014), this association is closer than the somewhat younger TW Hya (60 pc, 10 Myr; Schneider et al. 2012) and the somewhat older Tuc-Hor (40 pc, 30 Myr; Zuckerman et al. 2011) associations. Roughly 30% of the members have luminous debris disks (e.g., Rebull et al. 2008; Nilsson et al. 2009; Riviere-Marichalar et al. 2014); β Pic contains at least one gas giant (Lagrange et al. 2010). From current planet detection statistics, $\gtrsim$ 50%–60% of stars with $M_\star \lesssim 1$–2 $M_\odot$ have at least one planet with $m_p \gtrsim 5$–10 $M_\oplus$ and $a \lesssim 10$–20 AU (e.g., Najita & Kenyon 2014, and references therein). If satellite swarms around massive planets are relatively common, there is a a reasonably high probability of finding at least one satellite swarm within the β Pic moving group.

Although only one planetary mass companion has been detected orbiting members of the β Pic moving group, current detection limits are encouraging. Kasper et al. (2007) derive $\Delta m \approx 9$–10 mag at $0\farcs5$ in the broadband L filter; Biller et al. (2013) report $\Delta m \approx 14$–15 at 1–2$''$ in the broadband H and narrow band CH_4 filters. As the sample sizes grow and the data acquisition/reduction techniques improve, it should be possible to constrain the frequency of luminous satellite swarms around the nearest young stars.

5.3. Predictions for Irregular Satellites in the Solar System

Satellite swarm models for Fomalhaut b are based on the ensemble of irregular satellites orbiting the four gas giants in the solar system (e.g., Kennedy & Wyatt 2011). The ~ 160 known satellites have radii $r \lesssim 100$–200 km and lie on eccentric, high inclination orbits with semimajor axes of 20% to 50% of the Hill radius (e.g., Jewitt & Haghighipour 2007; Brozović et al. 2011; Alexandersen et al. 2012). Among the largest objects with $r \approx 10$–100 km, the cumulative size distribution is shallow and reasonably close to a power law with $n(> r) \propto r^{-q_c}$ and $q_c \approx 1$ (Jewitt & Haghighipour 2007; Bottke et al. 2010). For smaller objects, the size distribution may steepen.

Using a set of coagulation calculations, Bottke et al. (2010) show that several Gyr of collisional evolution naturally produces satellite swarms with shallow size distributions. For model satellites with $r \approx 0.05$–100 km orbiting Jupiter, the slope ranges from $q_c \approx 1.5$ for

$r \lesssim 5$ km to $q_c \lesssim 1$ at $r = 5$–100 km. Swarms with longer collision times orbiting Saturn and Uranus have somewhat steeper power laws.

Our calculations confirm and extend these results. For 0.1–10 km satellites orbiting 100–300 $M_\oplus$ planets, size distributions at 1 Gyr are wavy power laws with $q_c \approx 1$–2; 10–100 km objects have steeper power laws $q_c \sim 2$–3. We extended several of these calculations to 5 Gyr; large objects then have $q_c \sim 1$–2.

Satellites with $r \lesssim 0.1$ km have wavy cumulative size distributions with a broad range of power law slopes (Figs. 9–16). Independent of various input parameters, very small particles with $r \lesssim 1$ cm have steep power laws with $q_c \approx 4$. Intermediate size particles with $r \approx 1$ cm to 100 m have flatter size distributions, $q_c \approx 0$–2. These power laws are sensitive to the size of the smallest particles (Figs. 12–13). Calculations with smaller particles have steeper power laws than calculations with larger particles.

Although recent surveys detect several irregular satellites with $r \approx 1$ km around Jupiter (e.g., Brozović et al. 2011; Alexandersen et al. 2012; Jacobson et al. 2012; Gomes-Júnior et al. 2015), testing our predictions is challenging. With expected optical magnitudes $\gtrsim 28$, irregular satellites with $r \lesssim 0.1$ km are too faint for any current and planned ground-based telescope. However, many of our calculations predict changes in the slope of the size distribution at 0.1–1 km. Extending the discovery space to this size range is feasible and would place interesting constraints on the coagulation models.

6. CONCLUSIONS

We describe results from a large suite of coagulation calculations for irregular satellite swarms orbiting 1–300 $M_\oplus$ planets at $a = 120$ AU from a 1.9 $M_\odot$ central star. The calculations follow the evolution of the size distribution for 10 μm to 3000 km particles for 1 Gyr as a function of the initial mass of the swarm, the size of the smallest particle in the swarm, the initial size distribution of particles, the binding energy of the particles, and the method for distributing debris from a collision into smaller mass bins.

Throughout the evolution, the largest satellites may grow or shrink. Growing satellites may scatter other satellites out of the planet's Hill sphere or into tighter orbits around the planet. Among smaller satellites, the size distribution develops a characteristic shape with a steep power law at small sizes, a flat portion at intermediate sizes, and a shallow power law at larger sizes. The growth (shrinkage) of satellites and the time for the size distribution to develop a standard shape depend on the initial cloud mass, the initial size distribution, the initial r_{min} and r_{max}, and the binding energy of satellites.

In our baseline models, swarms orbiting 10–100 $M_\oplus$ planets have cross-sectional areas at 100–400 Myr comparable to the observed cross-sectional area of Fomalhaut b. In these models, $x_d = 0.01$ and $r_{min} = 100$ μm. Smaller x_d and larger r_{min} allow swarms orbiting somewhat more massive planets to match observations of Fomalhaut b. Calculations with smaller r_{min} require swarms around somewhat less massive planets. Changing the initial size distribution of satellites has little impact on these conclusions. Modifying the binding energy and the algorithm for distributing debris in smaller mass bins generally lowers the cross-sectional area, requiring swarms around more massive planets to match Fomalhaut b.

Aside from discussing the impact of these calculations on our understanding of planet formation theory (§5.1), we derive predictions for (i) irregular satellites in the solar system and (ii) Fomalhaut b and satellites swarms in other exoplanetary systems. Identifying 0.1–1 km irregular satellites orbiting Jupiter would set interesting constraints on coagulation models. In Fomalhaut b, we predict a detectable trail of small particles within a few AU of the nominal orbit of the planet candidate. For exoplanetary systems with ages of 1–10 Myr, detectable satellite swarms orbiting 30–300 $M_\oplus$ planets provide a way to estimate the frequency of sub-Jupiter mass planets at 50–150 AU around 1–2 $M_\odot$ stars.

We acknowledge generous allotments of computer time on the NASA 'discover' cluster. Comments and suggestions from M. Geller, G. Kennedy, and an anonymous referee improved our discussion. Portions of this project were supported by the *NASA Astrophysics Theory* and *Origins of Solar Systems* programs through grant NNX10AF35G and the *NASA Outer Planets Program* through grant NNX11AM37G.

A. Appendix

To test the algorithms used in *Orchestra*, we compare numerical results with analytic solutions to the coagulation equation (Kenyon & Luu 1998; Kenyon & Bromley 2015) and published results from other investigators (Kenyon & Bromley 2001; Bromley & Kenyon 2006; Kenyon & Bromley 2008; Bromley & Kenyon 2011; Kenyon & Bromley 2015). Here, we examine how *Orchestra* performs for collisional cascades in spherical swarms of satellites orbiting a massive planet.

The accuracy of all coagulation calculations depends on the mass spacing parameter between adjacent mass bins, $\delta_k = m_{k+1}/m_k$ (e.g., Wetherill 1990; Kenyon & Luu 1998; Kenyon & Bromley 2015). At the start of our calculations, we fix the typical mass m_k and the boundaries $m_{k-1/2}$ and $m_{k+1/2}$ of each mass bin. The initial average mass within each bin is $\bar{m}_k = M_k/N_k$; typically $\bar{m}_k \approx m_k$. As each calculation proceeds, collisions add

and remove mass from all bins; the average mass $\bar{m}_k$ and the average physical radius of particles $\bar{r}_k = (3\bar{m}_k/4\pi\rho_p)^{1/3}$ then change with time.

To illustrate how the evolution of satellite swarms changes with δ, we consider the baseline model described in the main text. An ensemble of satellites with $x_d = 0.01$, $r_{max} =$ 100 km, and $r_{min} = 100$ μm orbit a planet with $M_p = 10$ $M_\oplus$. The initial size distribution is a power law with $n(r) \propto r^{-q}$ and $q = 3.5$ between r_{min} and r_{max}.

Fig. 28 shows the time-variation of r_{max} for five different values of δ. In the figure, all curves have the same general shape: a brief, $\sim 10^5 - 10^6$ yr period where r_{max} is roughly constant, followed by a gradual decrease in r_{max} with time. Tracks with larger δ decline faster.

Along each track, the decline consists of a gradual reduction in r_{max} interspersed with occasional small jumps to larger r_{max} and large jumps to smaller r_{max}. In this example, collisions between equal mass objects with $r \approx r_{max}$ increase the mass of the merged pair. These collisions produce jumps to larger r_{max}. Cratering collisions – where somewhat smaller objects gradually chip away at the mass of larger objects – produce continuous mass loss from the largest objects. Thus, the average mass in the largest mass bin falls with time. Eventually, this mass falls below the mass boundary between adjacent bins (e.g., $\bar{m}_k < m_{k-1/2}$). Objects in bin k are then placed into bin $k-1$. Averaging the mass of the 'old' objects in bin $k-1$ with the 'new' objects from bin k yields a new average mass $\bar{m}_{k-1}$ which is smaller than the average mass of bin k. Thus, the size of the largest object jumps downward. Because the spacing of mass bins scales with δ, calculations with larger δ have larger jumps than those with smaller δ.

Although the mass loss rate from the grid is fairly insensitive to δ, the mass of the largest object clearly declines faster in calculations with larger δ. Cratering collisions are responsible for this difference. For all δ, these collisions are rare. Thus, only a few of the largest objects suffer substantial mass loss from cratering collisions every time step. When δ is small (1.05–1.10), these objects are placed into the next smallest mass bin; the average mass of the remaining objects in the mass bin is unchanged. When δ is large (1.41–2.00), the amount of mass loss is not sufficient to place objects into the next smallest mass bin; the average mass of all objects in the bin then decreases. As a result, the average mass of the largest objects declines faster when $\delta = 2$ than when $\delta = 1.05$.

Despite this difference, other aspects of the evolution are fairly insensitive to δ. Fig. 29 shows snapshots of the relative size distributions at 100 Myr. Each curve follows a standard pattern, with a steep power law at 0.1 mm to 10 cm, a minimum at $\sim$ 30 cm, a rise from 1 m to 100 m, a wavy pattern from 100 m to 50 km, and then an abrupt decline at the largest

sizes. When $\delta = 2$, the fluctuations about a reference model with $\delta = 1.05$ are large. For other δ, deviations from the reference model are minimal.

Fig. 30 illustrates the evolution of the relative surface area for two different baseline models as a function of δ. When $M_p = 10\ M_\oplus$, the relative area declines from roughly 10^2 at 100–1000 yr to roughly 0.1 at 1 Gyr. When $\delta = 1.05$, the decline is smooth, with a minor change in slope at roughly 10^4 yr. Adjustments from the initial power law to the non-power law equilibrium size distribution (e.g., Fig. 29) cause this change in slope. Evolution with $\delta = 2$ is more ragged, with modest fluctuations relative to the reference model with $\delta = 1.05$. As δ declines, the evolution of the relative area follows the reference model more closely.

When $M_p = 100\ M_\oplus$, the initial relative area for models with $x_d = 0.01$ is a factor of ten larger. The long term evolution is similar: a slow decline with an inflection point around 10^4 yr. Once again, the evolution of the relative area is somewhat more ragged in calculations with $\delta = 2$ than in calculations with smaller δ.

Although there are clear differences in the evolution as a function of δ, the ability of an initial set of model parameters to match the observations rarely depends on δ. For these two examples, all of the 100 M_p calculations pass through the target box for Fomalhaut b. All of the 10 M_p calculations graze the lower edge of the target box.

For swarms of satellites in a spherical shell around a massive planet, calculations with $\delta \lesssim 1.2$ yield a better understanding of the long term evolution of r_{max} and the size distribution. Evolution of the total mass and relative surface area are fairly insensitive to δ. Single annulus calculations with $\delta = 1.2$ run quickly, with execution times of 25 cpu hours for 1 Gyr evolution times using 10 μm to 1000 km particles. Thus, we perform most calculations with $\delta = 1.2$ and use occasional calculations with smaller δ to verify interesting features of the evolution.

REFERENCES

A'Hearn, M. F. 2011, ARA&A, 49, 281

Alexandersen, M., Gladman, B., Veillet, C., Jacobson, R., Brozović, M., & Rousselot, P. 2012, AJ, 144, 21

Arakawa, M. 1999, Icarus, 142, 34

Arakawa, M., Leliwa-Kopystynski, J., & Maeno, N. 2002, Icarus, 158, 516

Asphaug, E., & Benz, W. 1996, Icarus, 121, 225

Benz, W., & Asphaug, E. 1999, Icarus, 142, 5

Beust, H., et al. 2014, A&A, 561, A43

Biller, B. A., et al. 2013, ApJ, 777, 160

Bottke, W. F., Nesvorný, D., Vokrouhlický, D., & Morbidelli, A. 2010, AJ, 139, 994

Bromley, B. C., & Kenyon, S. J. 2006, AJ, 131, 2737

—. 2011, ApJ, 731, 101

—. 2013, ApJ, 764, 192

Brozović, M., Jacobson, R. A., & Sheppard, S. S. 2011, AJ, 141, 135

Burchell, M. J., Leliwa-Kopystyński, J., & Arakawa, M. 2005, Icarus, 179, 274

Burns, J. A., Lamy, P. L., & Soter, S. 1979, Icarus, 40, 1

Campo Bagatin, A., Cellino, A., Davis, D. R., Farinella, P., & Paolicchi, P. 1994, Planet. Space Sci., 42, 1079

Currie, T., Cloutier, R., Debes, J. H., Kenyon, S. J., & Kaisler, D. 2013, ApJ, 777, L6

Currie, T., et al. 2012, ApJ, 760, L32

Davis, D. R., Chapman, C. R., Weidenschilling, S. J., & Greenberg, R. 1985, Icarus, 63, 30

Dohnanyi, J. S. 1969, J. Geophys. Res., 74, 2531

Dominik, C., & Decin, G. 2003, ApJ, 598, 626

Durda, D. D., Bottke, W. F., Enke, B. L., Merline, W. J., Asphaug, E., Richardson, D. C., & Leinhardt, Z. M. 2004, Icarus, 170, 243

Durda, D. D., Bottke, W. F., Nesvorný, D., Enke, B. L., Merline, W. J., Asphaug, E., & Richardson, D. C. 2007, Icarus, 186, 498

Galicher, R., Marois, C., Zuckerman, B., & Macintosh, B. 2013, ApJ, 769, 42

Gáspár, A., Psaltis, D., Rieke, G. H., & Özel, F. 2012, ApJ, 754, 74

Gaspar, H. S., Winter, O. C., & Vieira Neto, E. 2013, MNRAS, 433, 36

Gault, D. E., Shoemaker, E. M., & Moore, H. J. 1963, NASA Tech. Note, D-1767

Giblin, I., Davis, D. R., & Ryan, E. V. 2004, Icarus, 171, 487

Gomes-Júnior, A. R., et al. 2015, ArXiv e-prints

Hamilton, D. P., & Burns, J. A. 1992, Icarus, 96, 43

Hamilton, D. P., & Krivov, A. V. 1997, Icarus, 128, 241

Holsapple, K. A. 1994, Planet. Space Sci., 42, 1067

Holsapple, K. A., & Housen, K. R. 2007, Icarus, 191, 586

Housen, K. R., & Holsapple, K. A. 1999, Icarus, 142, 21

—. 2003, Icarus, 163, 102

—. 2011, Icarus, 211, 856

Jacobson, R., Brozović, M., Gladman, B., Alexandersen, M., Nicholson, P. D., & Veillet, C. 2012, AJ, 144, 132

Janson, M., Carson, J. C., Lafrenière, D., Spiegel, D. S., Bent, J. R., & Wong, P. 2012, ApJ, 747, 116

Janson, M., Quanz, S. P., Carson, J. C., Thalmann, C., Lafrenière, D., & Amara, A. 2015, A&A, 574, A120

Jewitt, D., & Haghighipour, N. 2007, ARA&A, 45, 261

Kalas, P., Graham, J. R., Fitzgerald, M. P., & Clampin, M. 2013, ArXiv e-prints

Kalas, P., et al. 2008, Science, 322, 1345

Kasper, M., Apai, D., Janson, M., & Brandner, W. 2007, A&A, 472, 321

Kennedy, G. M., & Wyatt, M. C. 2010, MNRAS, 405, 1253

—. 2011, MNRAS, 412, 2137

Kennedy, G. M., Wyatt, M. C., Su, K. Y. L., & Stansberry, J. A. 2011, MNRAS, 417, 2281

Kenyon, S. J., & Bromley, B. C. 2001, AJ, 121, 538

—. 2004, AJ, 127, 513

—. 2005, AJ, 130, 269

—. 2008, ApJS, 179, 451

—. 2010, ApJS, 188, 242

—. 2012, AJ, 143, 63

—. 2014, AJ, 147, 8

—. 2015, ApJ

Kenyon, S. J., Currie, T., & Bromley, B. C. 2014, ApJ, 786, 70

Kenyon, S. J., & Luu, J. X. 1998, AJ, 115, 2136

—. 1999, AJ, 118, 1101

Kobayashi, H., & Tanaka, H. 2010, Icarus, 206, 735

Koch, F. E., & Hansen, B. M. S. 2011, MNRAS, 416, 1274

Kral, Q., Thébault, P., & Charnoz, S. 2013, A&A, 558, A121

Krivov, A. V., Löhne, T., & Sremčević, M. 2006, A&A, 455, 509

Lagrange, A.-M., et al. 2010, Science, 329, 57

Lawler, S. M., Greenstreet, S., & Gladman, B. 2015, ApJ, 802, L20

Leinhardt, Z. M., & Stewart, S. T. 2009, Icarus, 199, 542

—. 2012, ApJ, 745, 79

Leinhardt, Z. M., Stewart, S. T., & Schultz, P. H. 2008, in The Solar System Beyond Neptune, ed. Barucci, M. A., Boehnhardt, H., Cruikshank, D. P., & Morbidelli, A. (University of Arizona Press, Tucson, AZ), 195–211

Löhne, T., Krivov, A. V., & Rodmann, J. 2008, ApJ, 673, 1123

Love, S. G., & Ahrens, T. J. 1996, Icarus, 124, 141

Mamajek, E. E. 2012, ApJ, 754, L20

Mamajek, E. E., & Bell, C. P. M. 2014, MNRAS, 445, 2169

Marengo, M., Stapelfeldt, K., Werner, M. W., Hora, J. L., Fazio, G. G., Schuster, M. T., Carson, J. C., & Megeath, S. T. 2009, ApJ, 700, 1647

Martin, R. G., & Lubow, S. H. 2011, MNRAS, 413, 1447

Matthews, B. C., Krivov, A. V., Wyatt, M. C., Bryden, G., & Eiroa, C. 2014, ArXiv e-prints

Morbidelli, A., Bottke, W. F., Nesvorný, D., & Levison, H. F. 2009, Icarus, 204, 558

Najita, J. R., & Kenyon, S. J. 2014, MNRAS, 445, 3315

Nesvorný, D., Vokrouhlický, D., & Deienno, R. 2014, ApJ, 784, 22

Nilsson, R., Liseau, R., Brandeker, A., Olofsson, G., Risacher, C., Fridlund, M., & Pilbratt, G. 2009, A&A, 508, 1057

O'Brien, D. P., & Greenberg, R. 2003, Icarus, 164, 334

Poelchau, M. H., Kenkmann, T., Hoerth, T., Schäfer, F., Rudolf, M., & Thoma, K. 2014, Icarus, 242, 211

Poppe, A., & Horányi, M. 2011, Planet. Space Sci., 59, 1647

Quillen, A. C., Hasan, I., & Moore, A. 2012, MNRAS, 425, 2507

Rebull, L. M., et al. 2008, ApJ, 681, 1484

Richardson, J. E., Melosh, H. J., Lisse, C. M., & Carcich, B. 2007, Icarus, 190, 357

Riviere-Marichalar, P., et al. 2014, A&A, 565, A68

Ryan, E. V., Davis, D. R., & Giblin, I. 1999, Icarus, 142, 56

Schneider, A., Melis, C., & Song, I. 2012, ApJ, 754, 39

Schneider, G., et al. 2014, AJ, 148, 59

Shen, Y., & Tremaine, S. 2008, AJ, 136, 2453

Shimaki, Y., & Arakawa, M. 2012, Icarus, 218, 737

Skorov, Y., & Blum, J. 2012, Icarus, 221, 1

Spaute, D., Weidenschilling, S. J., Davis, D. R., & Marzari, F. 1991, Icarus, 92, 147

Stern, S. A., & Colwell, J. E. 1997, AJ, 114, 841

Svetsov, V. 2011, Icarus, 214, 316

Tamayo, D. 2013, ArXiv e-prints

Tanaka, H., Inaba, S., & Nakazawa, K. 1996, Icarus, 123, 450

Thébault, P., Augereau, J. C., & Beust, H. 2003, A&A, 408, 775

Toth, I. 1999, Icarus, 141, 420

Weidenschilling, S. J. 2010, ApJ, 722, 1716

Wetherill, G. W. 1990, Icarus, 88, 336

Wetherill, G. W., & Stewart, G. R. 1993, Icarus, 106, 190

Williams, D. R., & Wetherill, G. W. 1994, Icarus, 107, 117

Wyatt, M. C. 2008, ARA&A, 46, 339

Wyatt, M. C., & Dent, W. R. F. 2002, MNRAS, 334, 589

Wyatt, M. C., Smith, R., Greaves, J. S., Beichman, C. A., Bryden, G., & Lisse, C. M. 2007a, ApJ, 658, 569

Wyatt, M. C., Smith, R., Su, K. Y. L., Rieke, G. H., Greaves, J. S., Beichman, C. A., & Bryden, G. 2007b, ApJ, 663, 365

Yasui, M., Hayama, R., & Arakawa, M. 2014, Icarus, 233, 293

Zuckerman, B., Rhee, J. H., Song, I., & Bessell, M. S. 2011, ApJ, 732, 61

Zuckerman, B., Song, I., Bessell, M. S., & Webb, R. A. 2001, ApJ, 562, L87

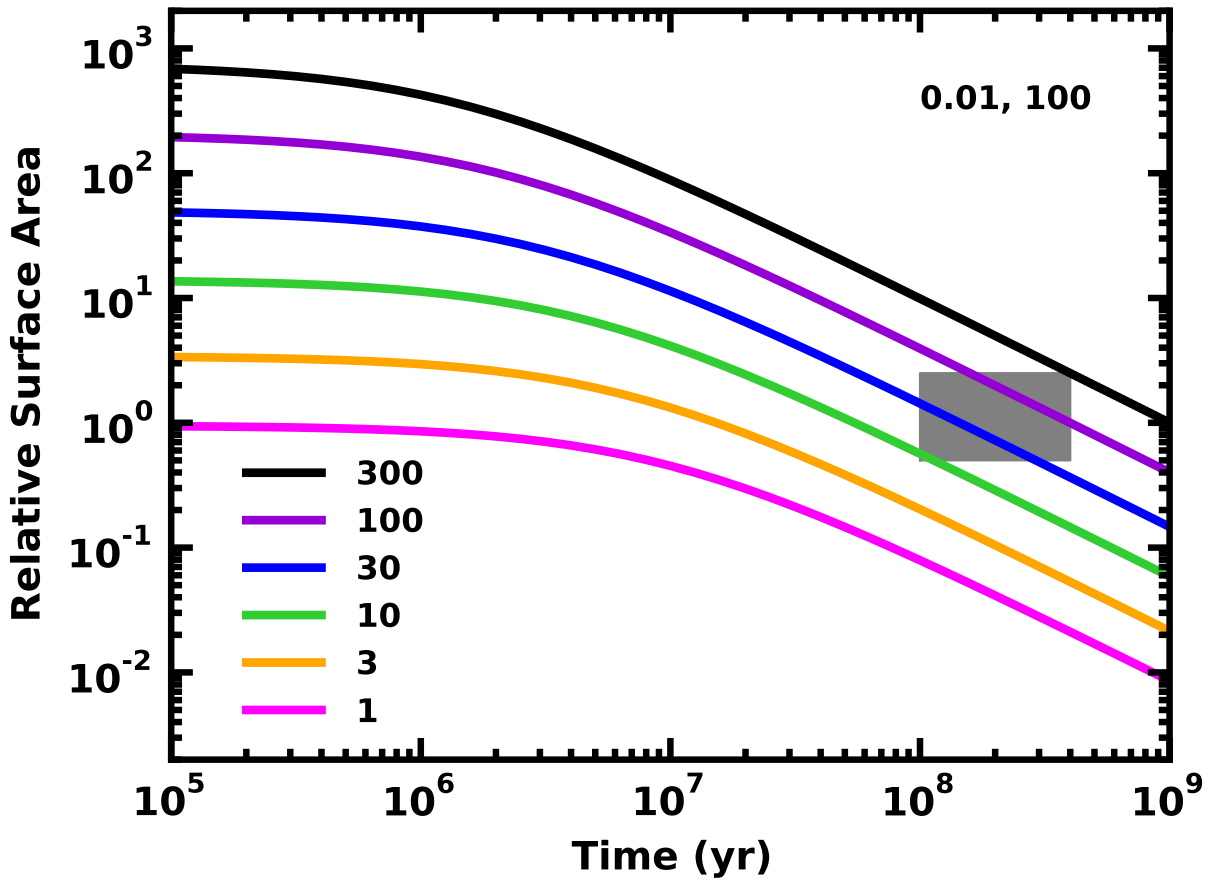

Fig. 1.— Time evolution of the relative surface area for the analytic model with $\alpha = 1$ described in the text. The legend in the lower left indicates M_p the mass of the planet in $M_\oplus$ for each solid curve. The legend in the upper right indicates x_d the mass of circumplanetary material relative to the mass of the planet and r_{max} the radius (in km) of the largest object in the swarm. Eq. 8 sets values for r_{min} the radius (in μm) of the smallest particle in the swarm. The grey shaded box indicates the locus of allowed points for Fomalhaut b, using the surface area derived from the measured brightness, the age of Fomalhaut, and 1σ errors. For the adopted combination of x_d and r_{max}, clouds orbiting planets with $M_p \approx 30$–100 $M_\oplus$ match the observations. Models with $M_p = 10$ $M_\oplus$ and 300 $M_\oplus$ barely miss the shaded box; those with $M_p = 1$ $M_\oplus$ have too little surface area at all times.

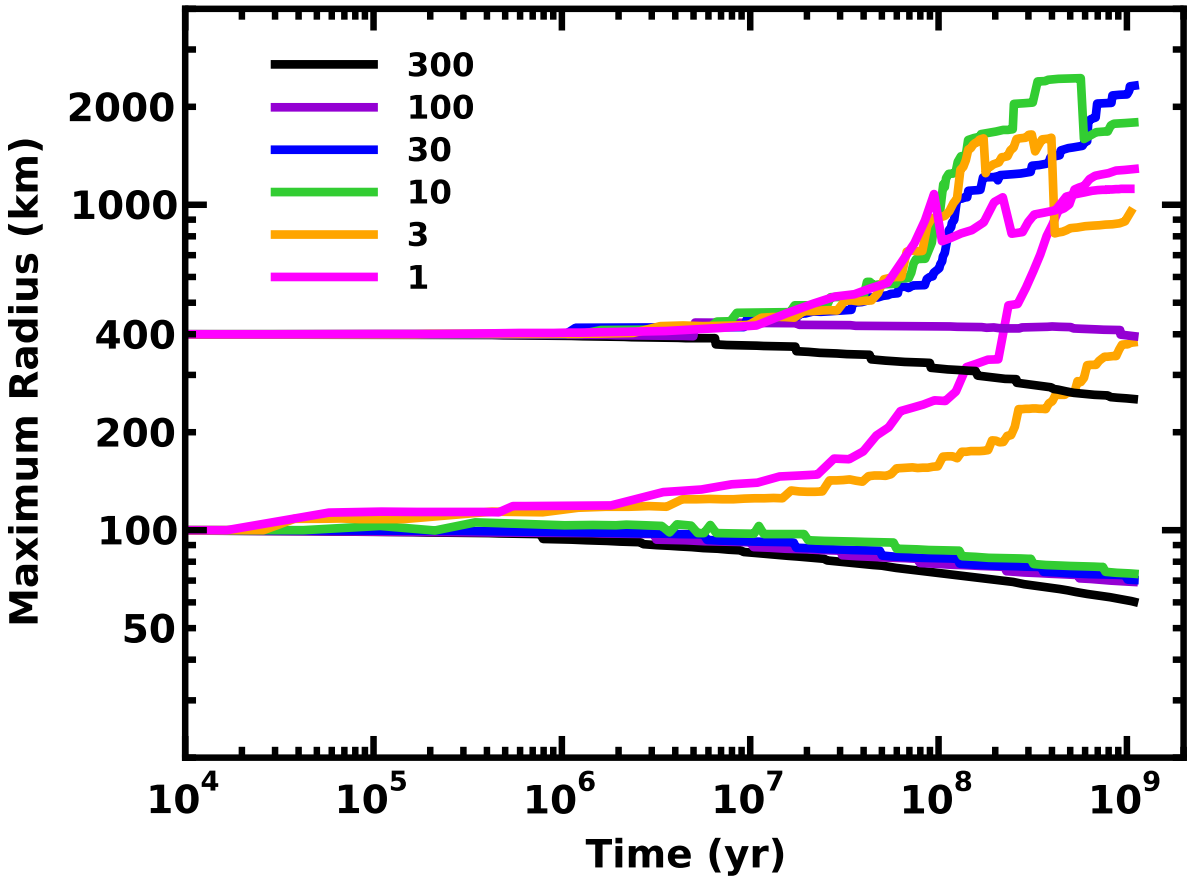

Fig. 2.— Time evolution of the radius of the largest object derived from coagulation calculations of circumplanetary clouds of particles with the nominal fragmentation parameters, $x_d = 0.01$, $r_{min} = 100$ μm, $m_{l,0} = 0.2$, and $b_l = 0.0$. The legend in the upper left indicates M_p for each solid curve. For calculations with massive planets, the size of the largest object smoothly declines with time. When the mass of the planet is smaller, the largest objects sweep up small particles and grow into much larger objects. In calculations where r_{max} is 400 km (50 km), the largest objects are more (less) likely to grow with time.

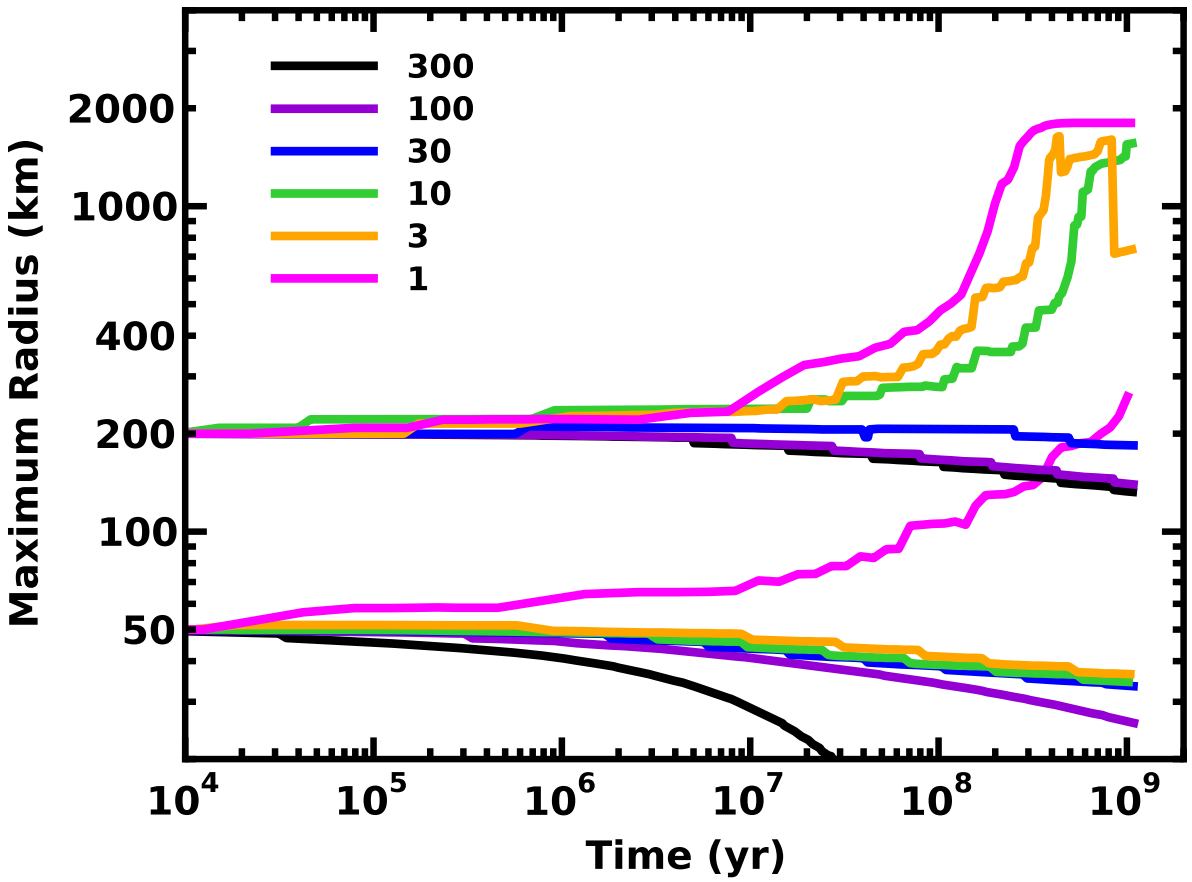

Fig. 3.— As in Fig. 2 for calculations starting with r_{max} = 50 km and 200 km. When M_p is large, the collisional cascade gradually destroys the largest objects. Around lower mass planets, the largest objects grow with time.

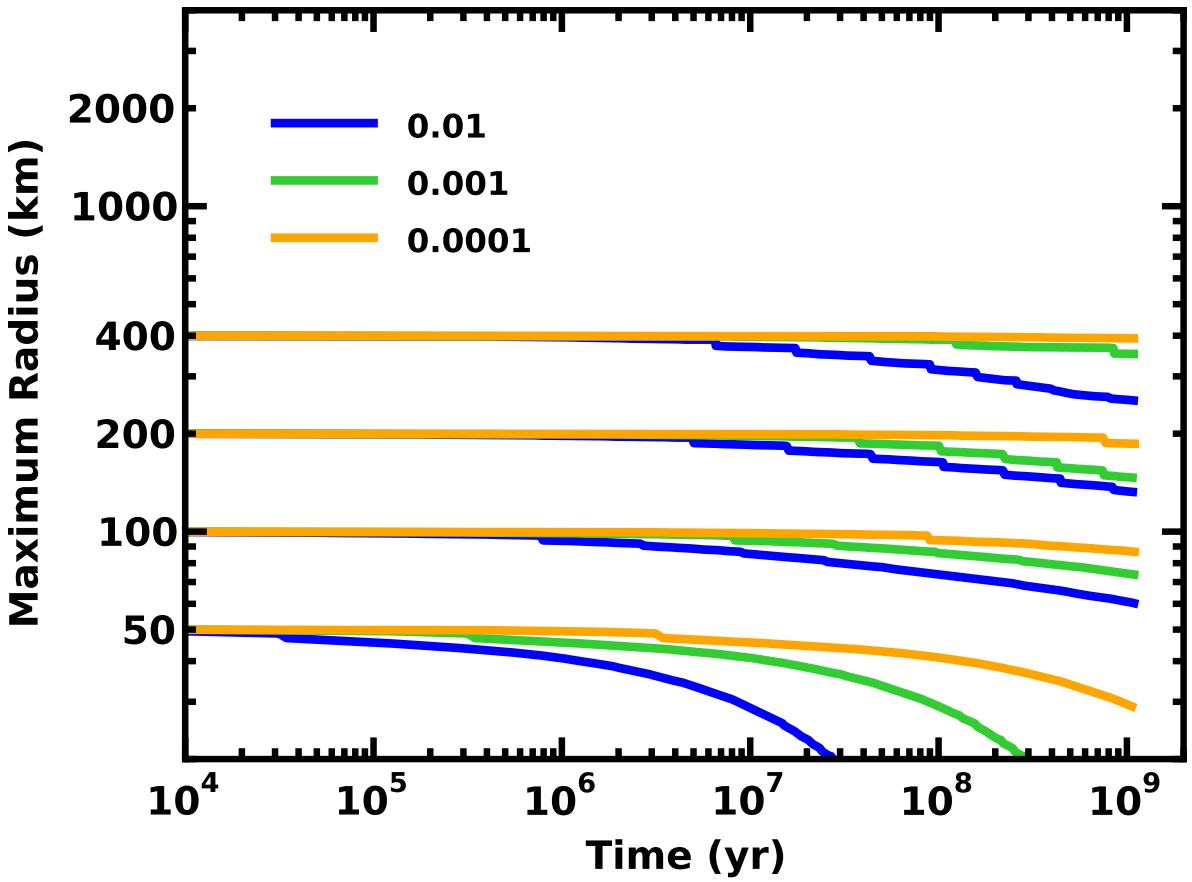

Fig. 4.— As in Figs. 2–3 for calculations with $M_p = 300\ M_\oplus$ and x_d as indicated in the legend. When the mass of the cloud is smaller, the radius of the largest object changes more slowly.

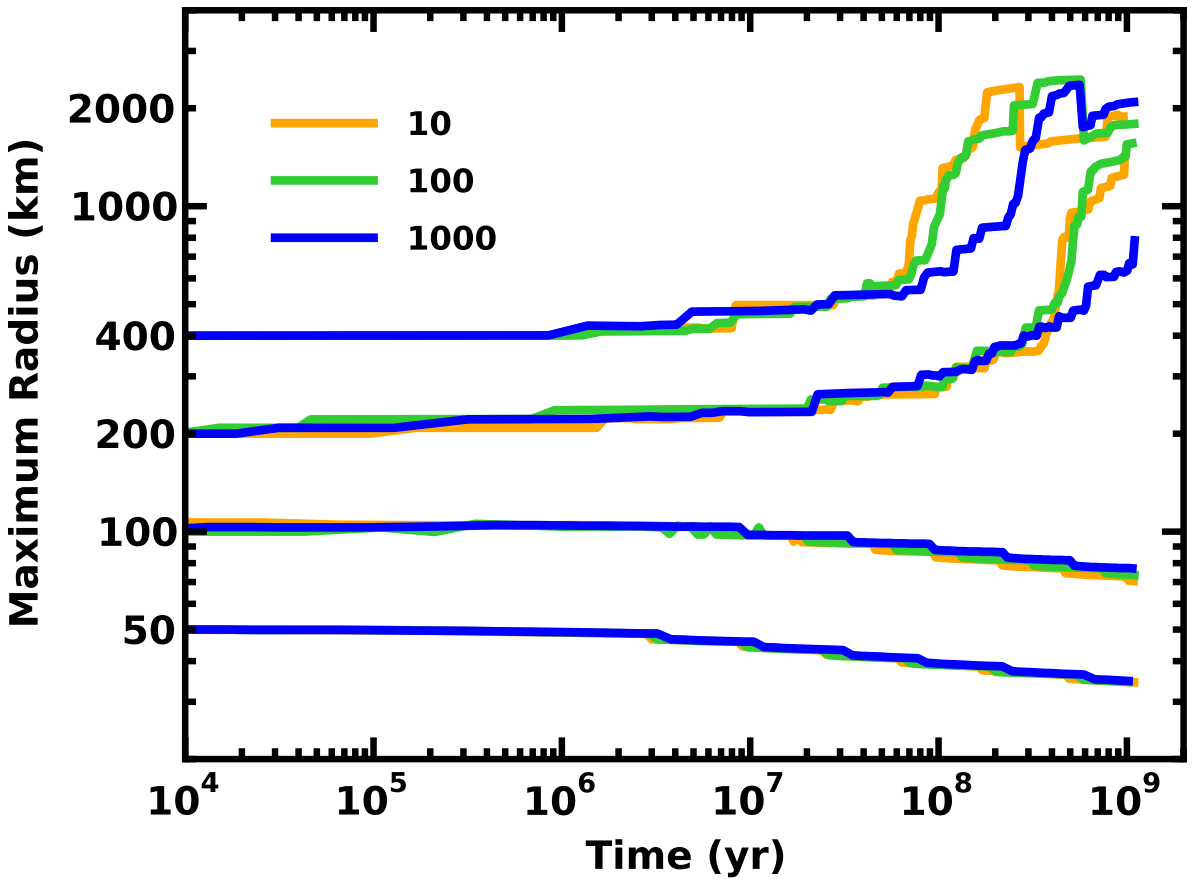

Fig. 5.— As in Figs. 2–3 for calculations with $M_p = 10\ M_\oplus$ and $r_{min} = 10\ \mu$m (orange curves), $r_{min} = 100\ \mu$m (green curves), and $r_{min} = 1000\ \mu$m (1 mm; blue curves). The growth of large objects is fairly independent of the size of the smallest particles in the grid.

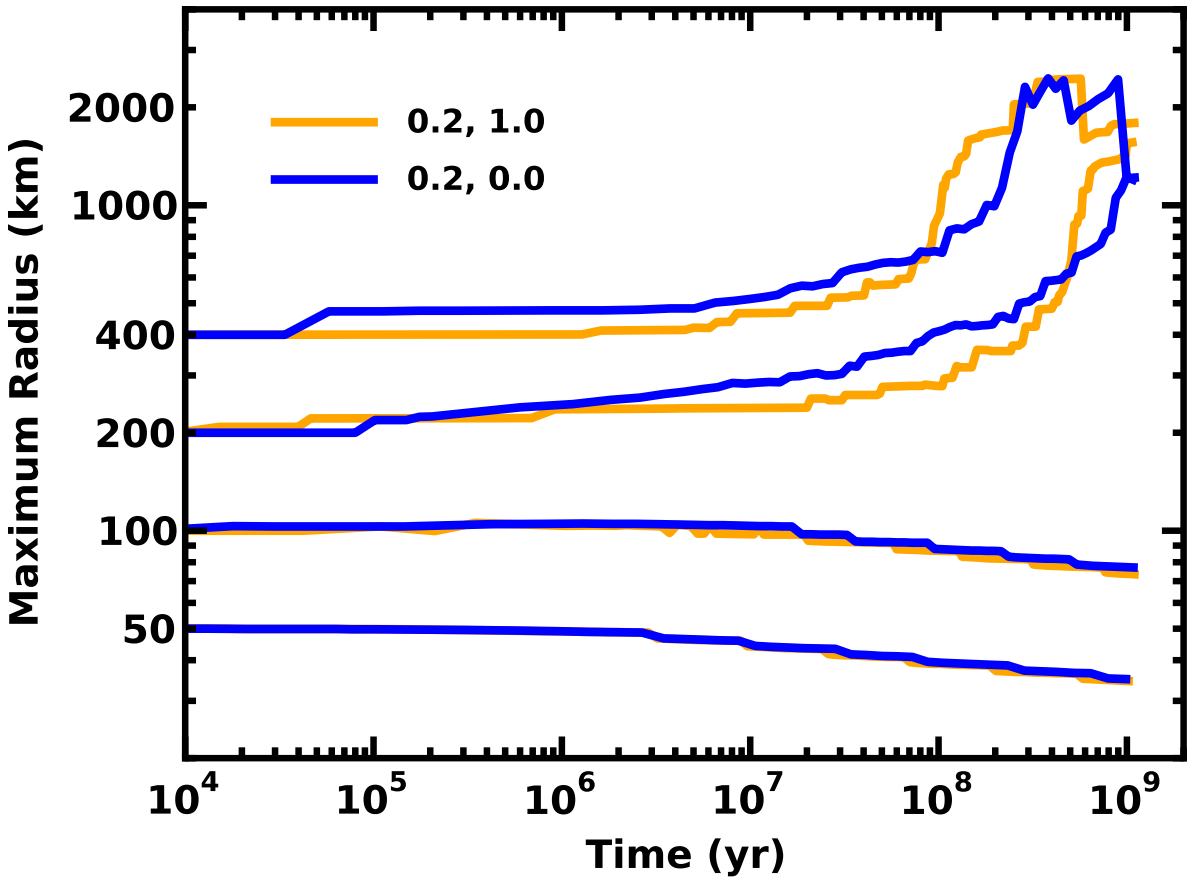

Fig. 6.— As in Figs. 2–3 for calculations with $M_p = 10\ M_\oplus$, $m_{L,0} = 0.2$, and either $b_l = 0.0$ (blue curves) or $b_l = 1.0$ (orange curves). The growth of large objects is fairly independent of the exponent in the relation between the mass of the largest object and the collision energy.

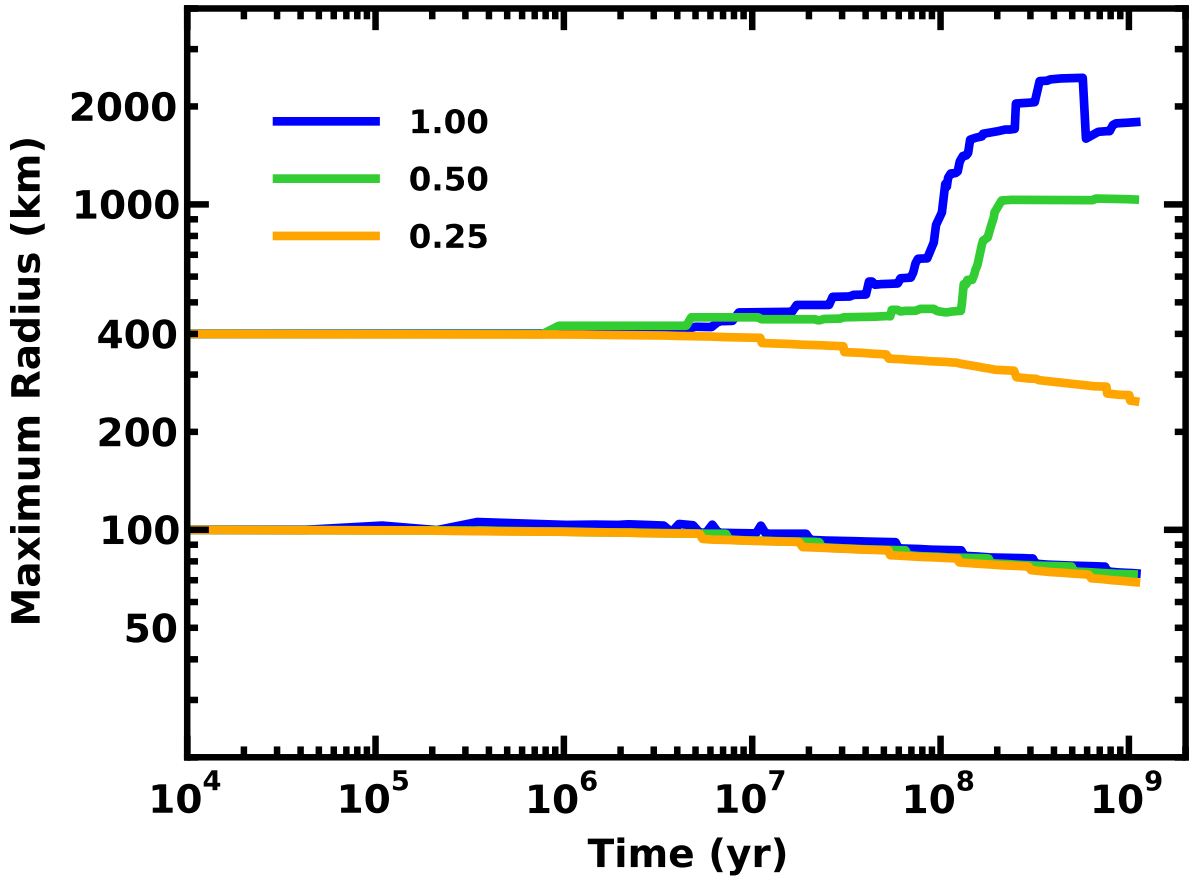

Fig. 7.— As in Figs. 2–3 for calculations with $M_p = 10\ M_\oplus$ and different $Q_D^\star$. The legend indicates the value of $Q_D^\star$ relative to the nominal fragmentation parameters listed in the main text.

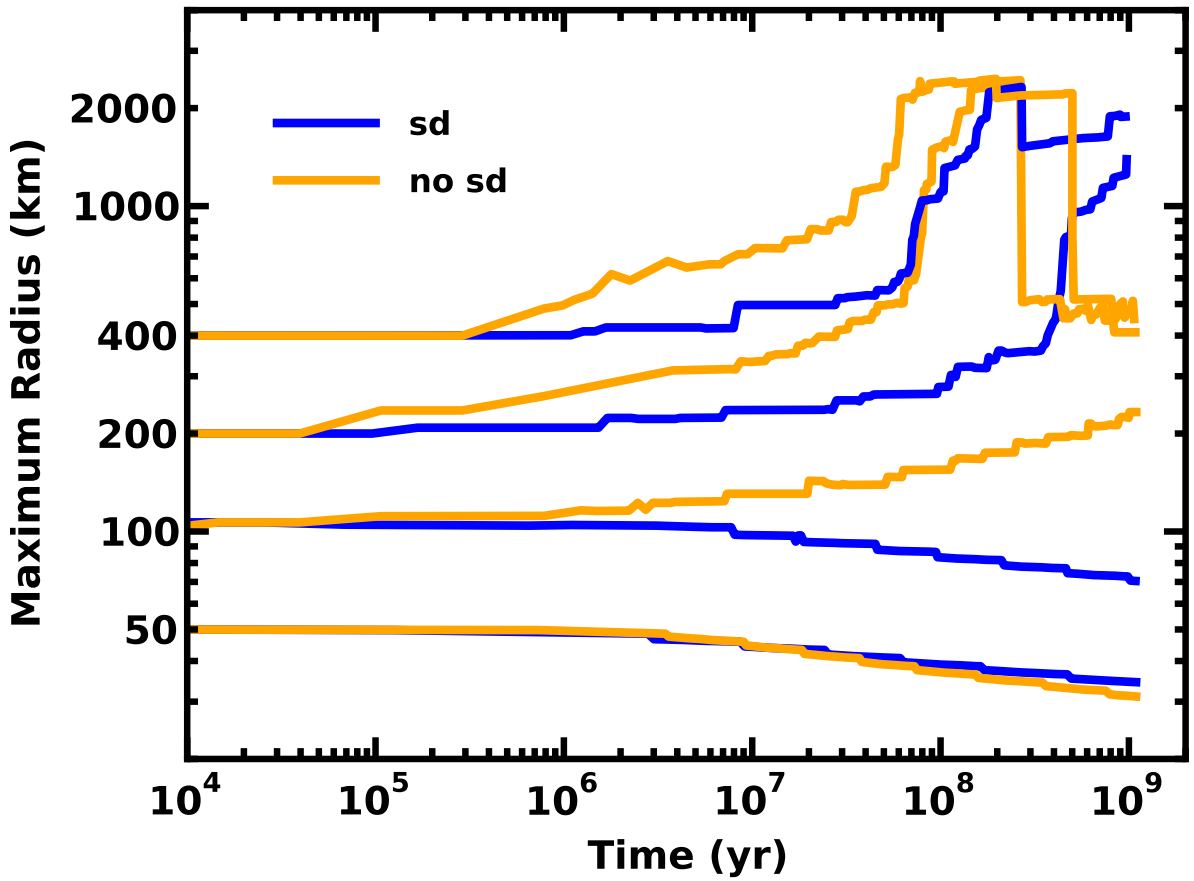

Fig. 8.— As in Figs. 2–3 for calculations with $M_p = 10\ M_\oplus$ and different initial size distributions. The legend indicates whether the calculation starts with a mono-disperse set of satellites (no sd) or a power law size distribution. When the initial population is mono-disperse, satellites grow faster.

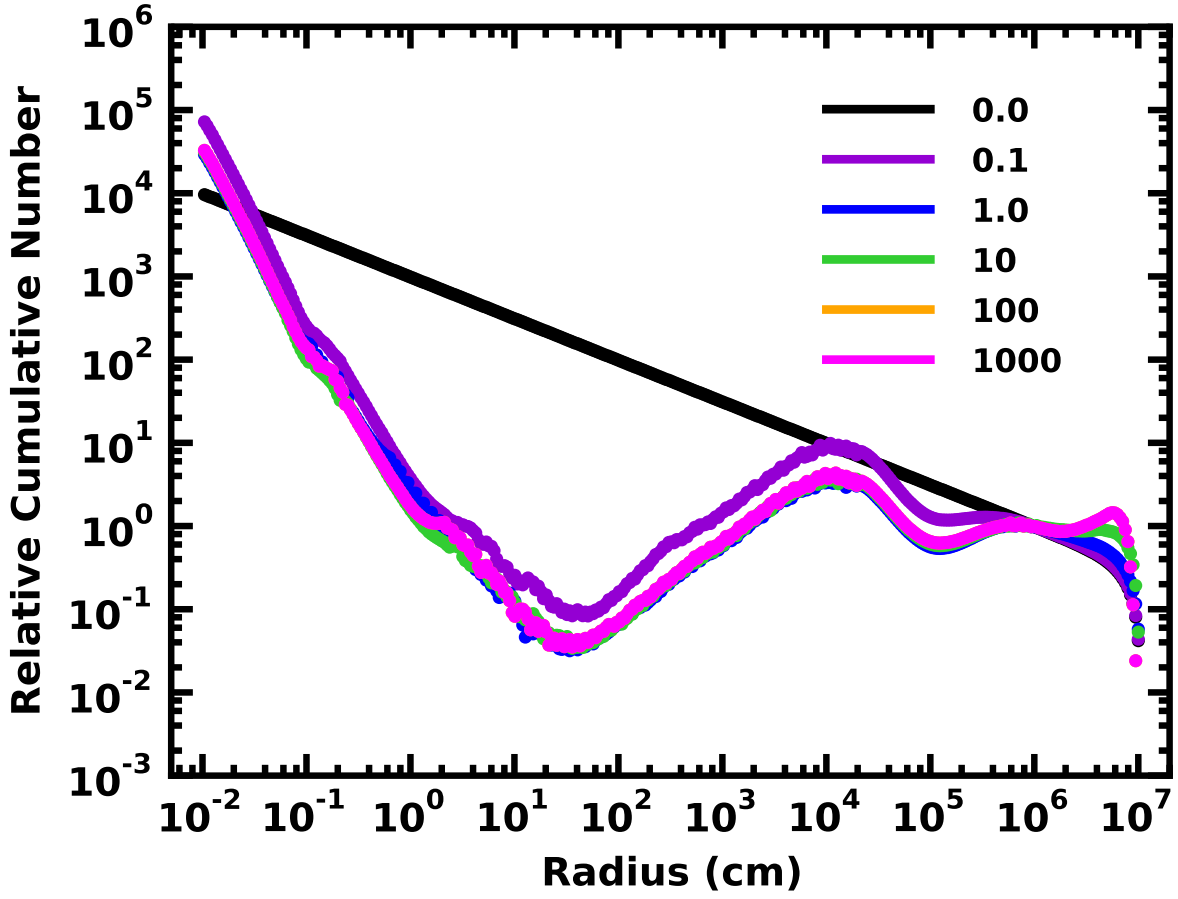

Fig. 9.— Snapshots evolution of the relative cumulative size distribution for calculations with $M_p = 10\ M_\oplus$, $x_d = 0.01$, $r_{max} = 100$ km, $r_{min} = 100\ \mu$m, $m_{l,0} = 0.2$, and $b_l = 0.0$. The legend in the upper right indicates the evolution time in Myr. Within roughly 1 Myr, collisions produce several distinct features in the relative size distribution: (i) a steep rise at the largest sizes ($r \gtrsim 50$ km), (ii) a shallower rise which approximately follows the original power law, (iii) a sharp drop at intermediate sizes ($r \approx 30$ cm to 0.1 km), and (iv) a steep rise at the smallest sizes ($r \approx 0.1$ mm to 30 cm).

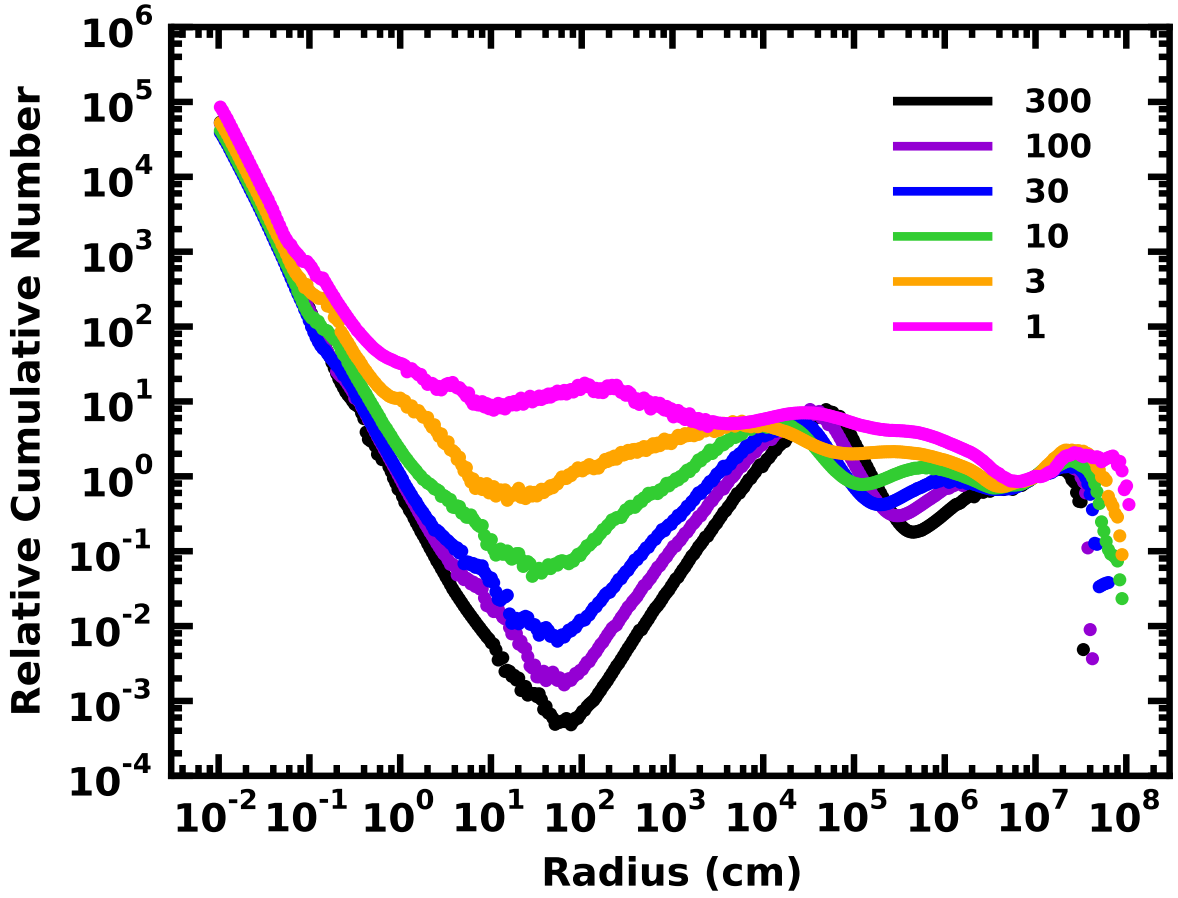

Fig. 10.— As in Fig. 9 for a range of masses for the central planet at $t = 100$ Myr. The legend in the upper right indicates the mass of the planet in $M_\oplus$. For all M_p, the size distribution is very steep for particle sizes $r \approx 0.1$ mm to 1–30 cm. The depth of the minimum at 10–30 cm grows with the mass of the planet. For $r \gtrsim 0.1$ km, fluctuations about the original power law grow with the mass of the planet.

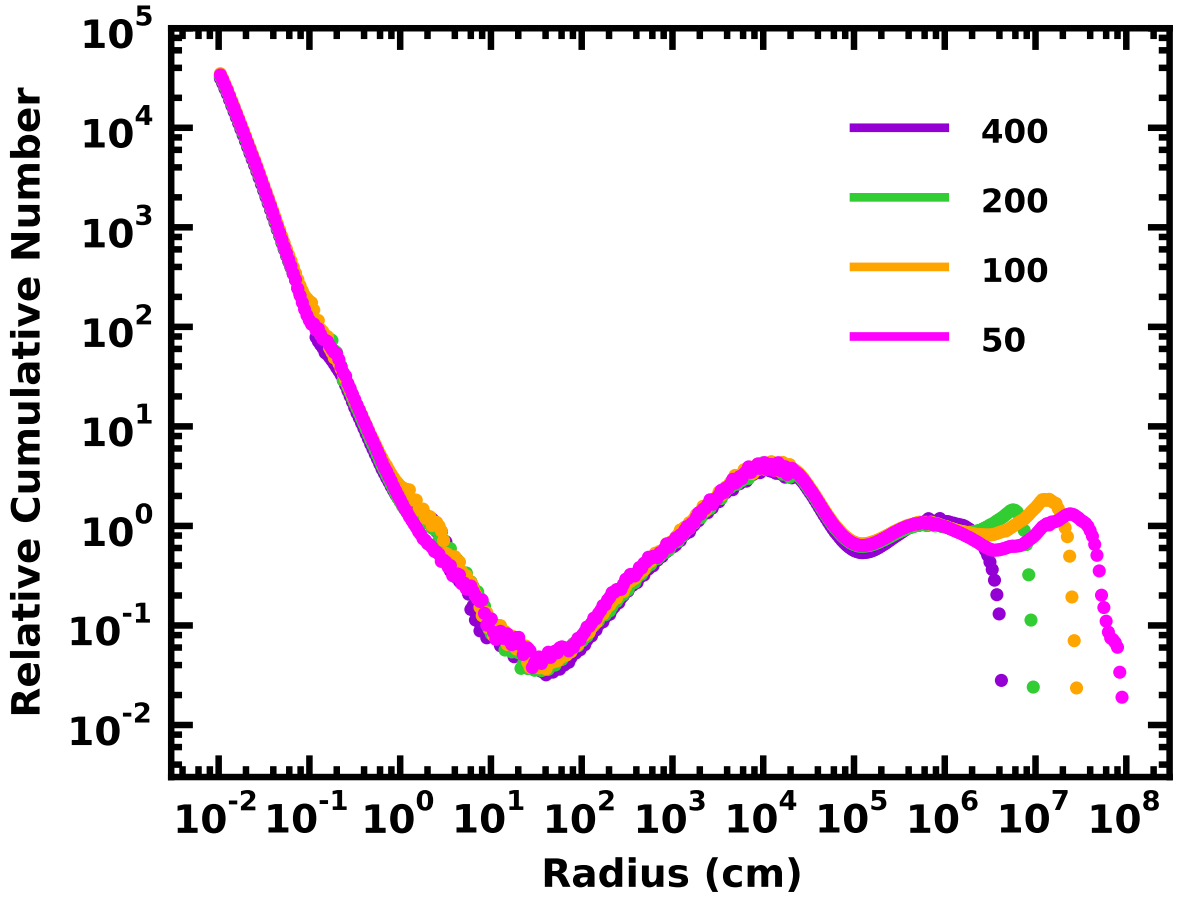

Fig. 11.— As in Fig. 10 for $M_p = 10\ M_\oplus$ and various initial r_{max} as indicated in the legend. Aside from differences at $r \approx r_{max}$, the relative size distribution at 100 Myr is independent of initial r_{max}.

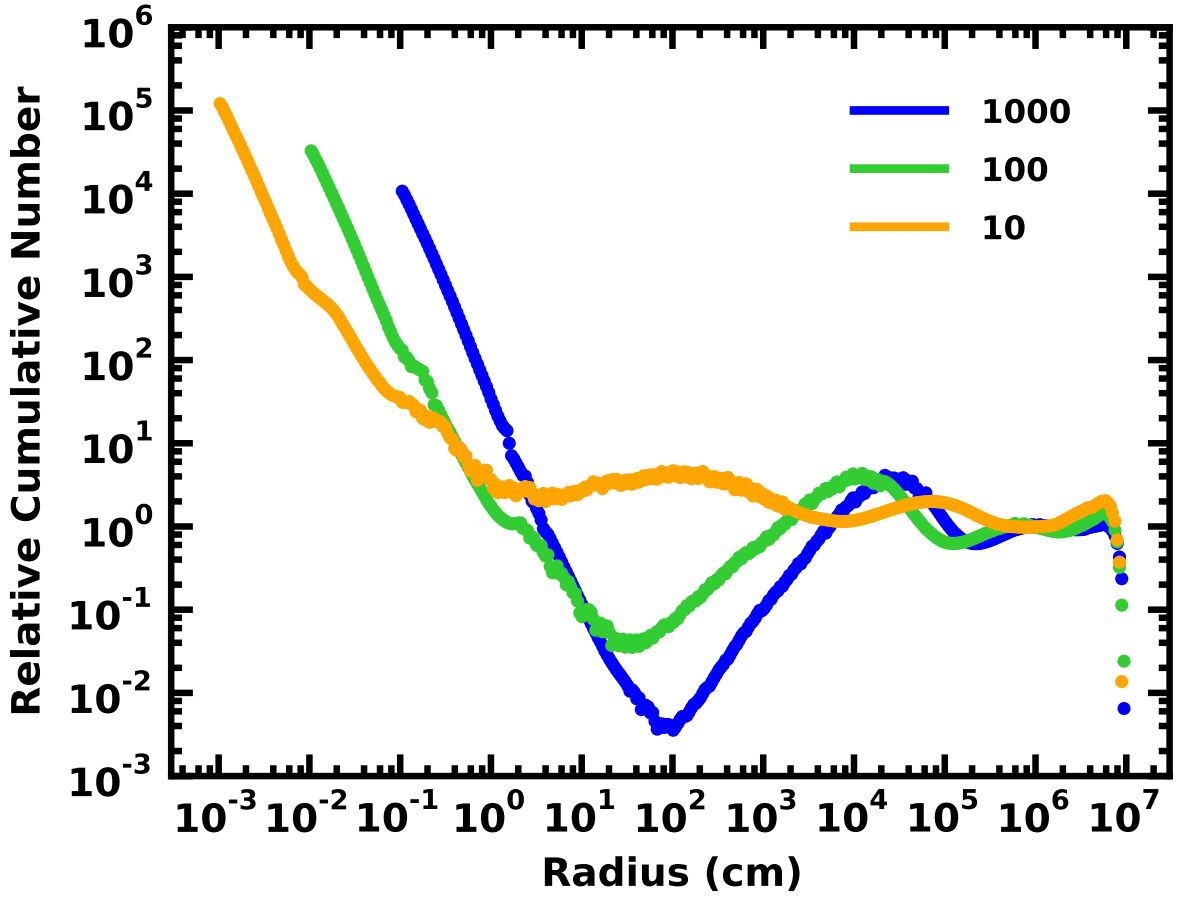

Fig. 12.— As in Fig. 11 for r_{max} = 100 km and various r_{min} as indicated in the legend. When r_{min} is smaller, the relative size distribution is closer to a single power law for $r \gtrsim$ 1 cm and has a smaller deficit of particles at 10–1000 cm.

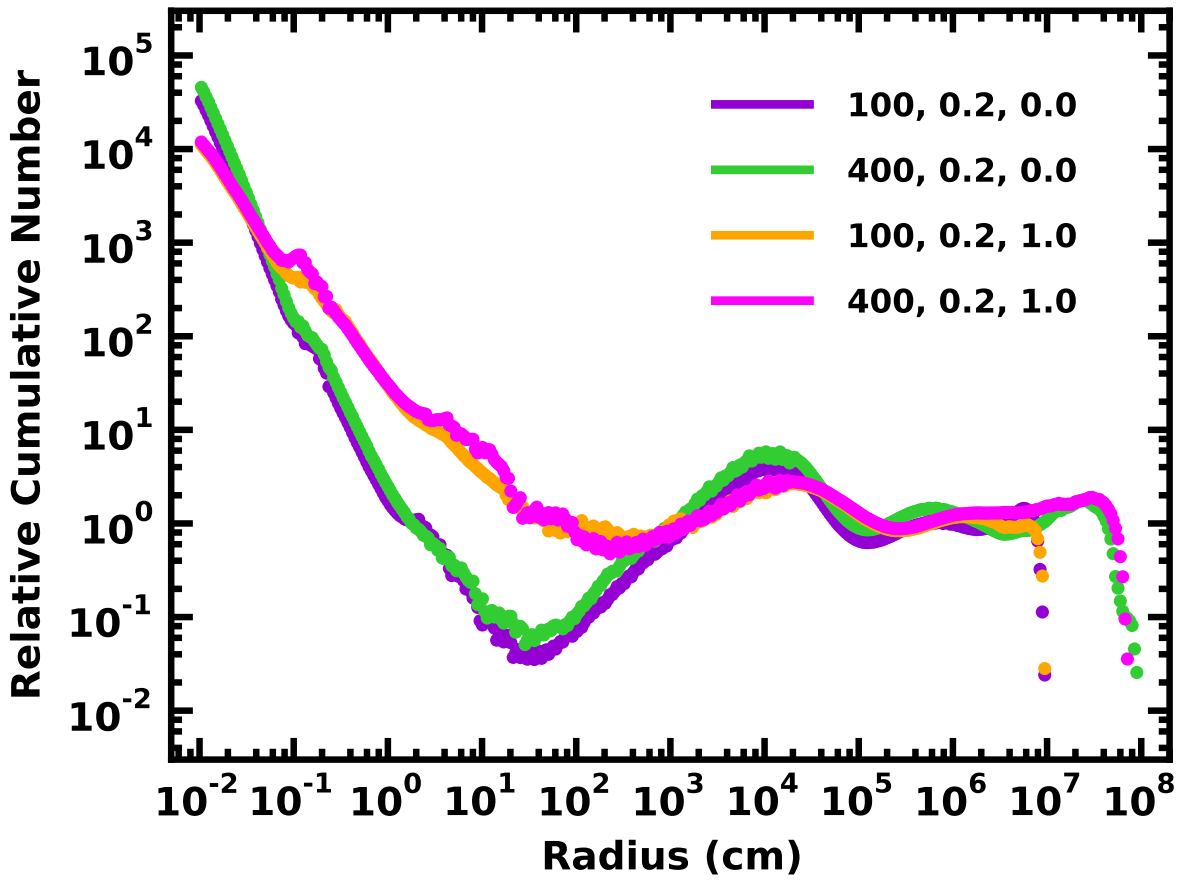

Fig. 13.— As in Fig. 10 for $M_p = 10\ M_\oplus$ and various combinations of r_{max}, $m_{L,0}$, and b_L as indicated in the legend. For $r \gtrsim 10^3$ cm, the relative size distribution is fairly independent of b_L. Among smaller particles, calculations with $b_L = 1$ yield a shallower size distribution than those with $b_L = 0$.

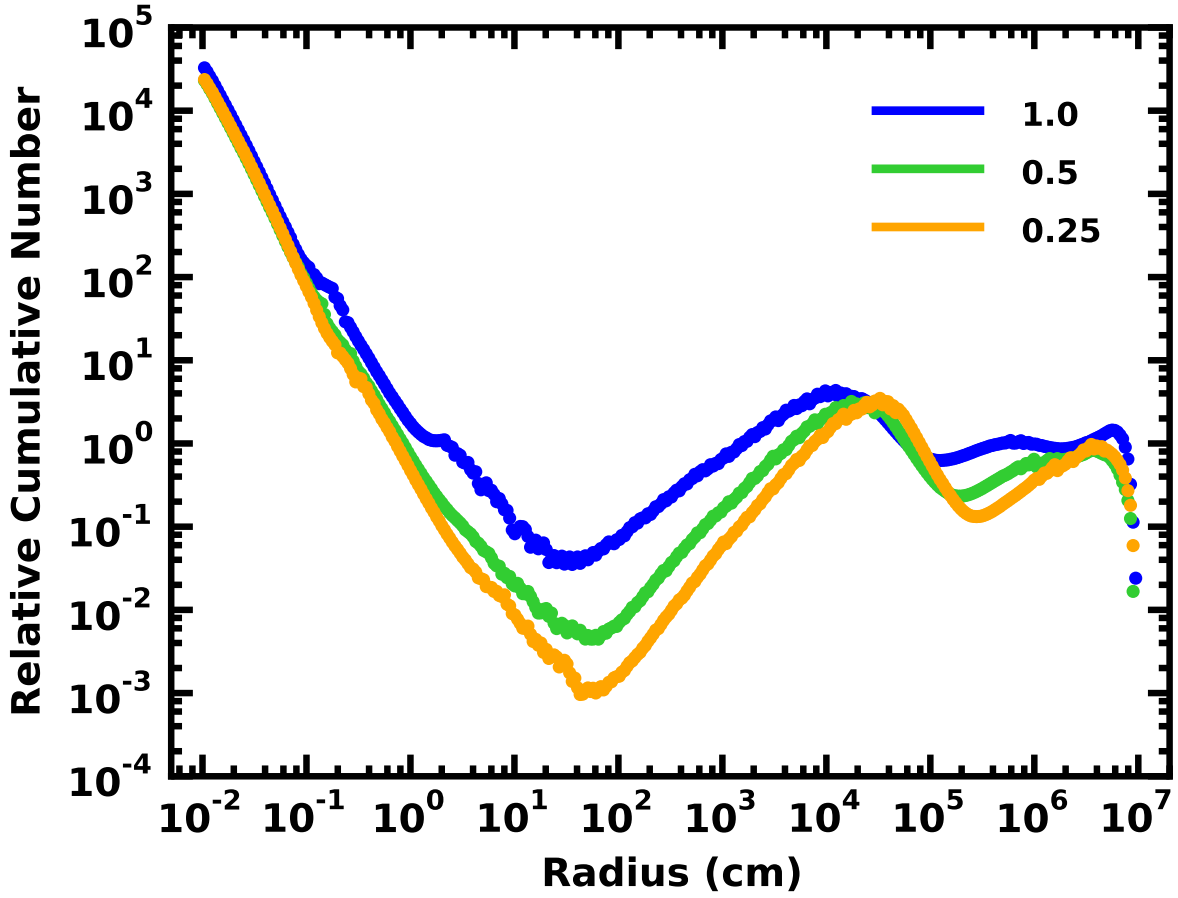

Fig. 14.— As in Fig. 11 for $r_{max} = 100$ km, $r_{min} = 100$ μm, and different values for $Q_D^\star$. The legend indicates the value of $Q_D^\star$ relative to the nominal fragmentation parameters listed in the main text.

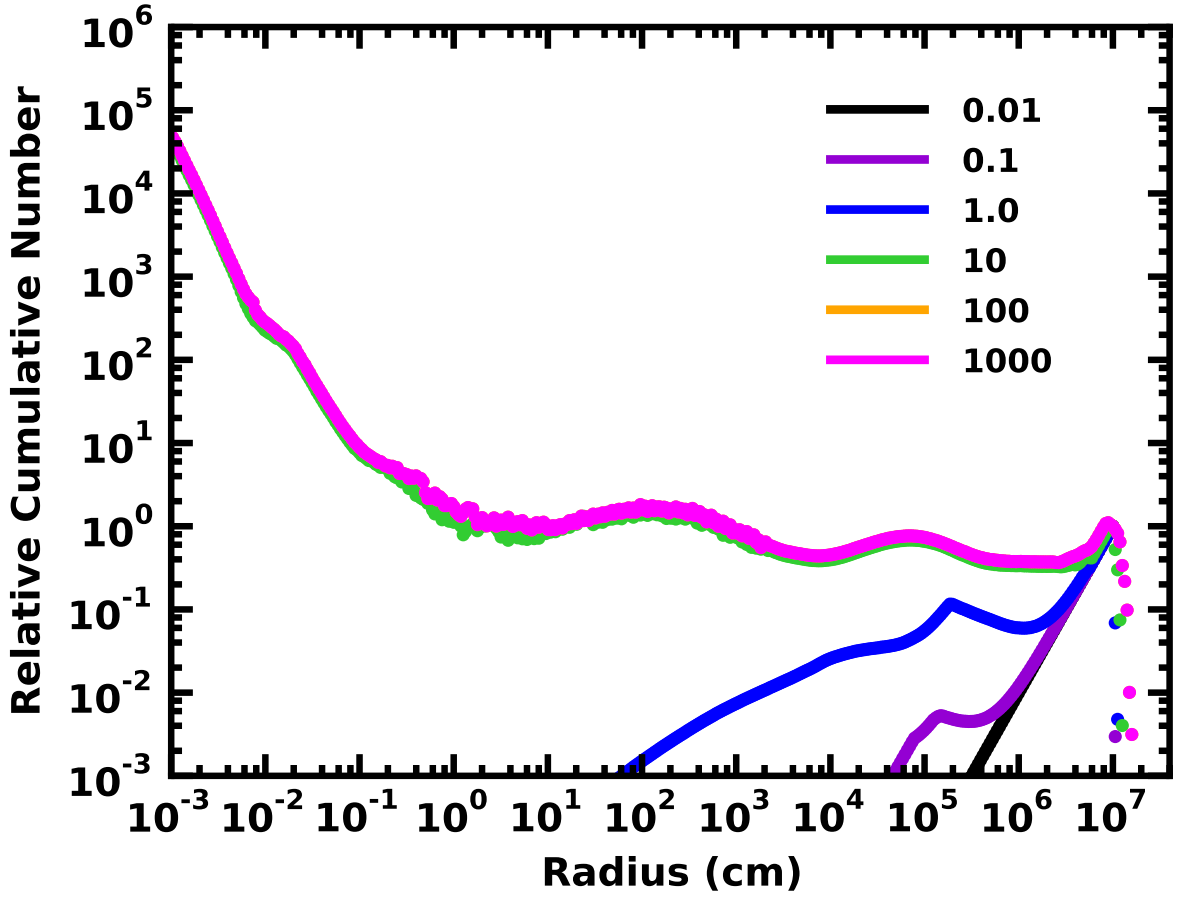

Fig. 15.— As in Fig. 9 for calculations starting with a mono-disperse set of particles. The legend indicates the evolution time in Myr. At early times, collisions among 100 km objects produce a small amount of debris populating the small size end of the size distribution. After 10 Myr, debris from these collisions and the debris from collisions of smaller objects yields a smooth equilibrium size distribution from 10 μm to roughly 100 km.

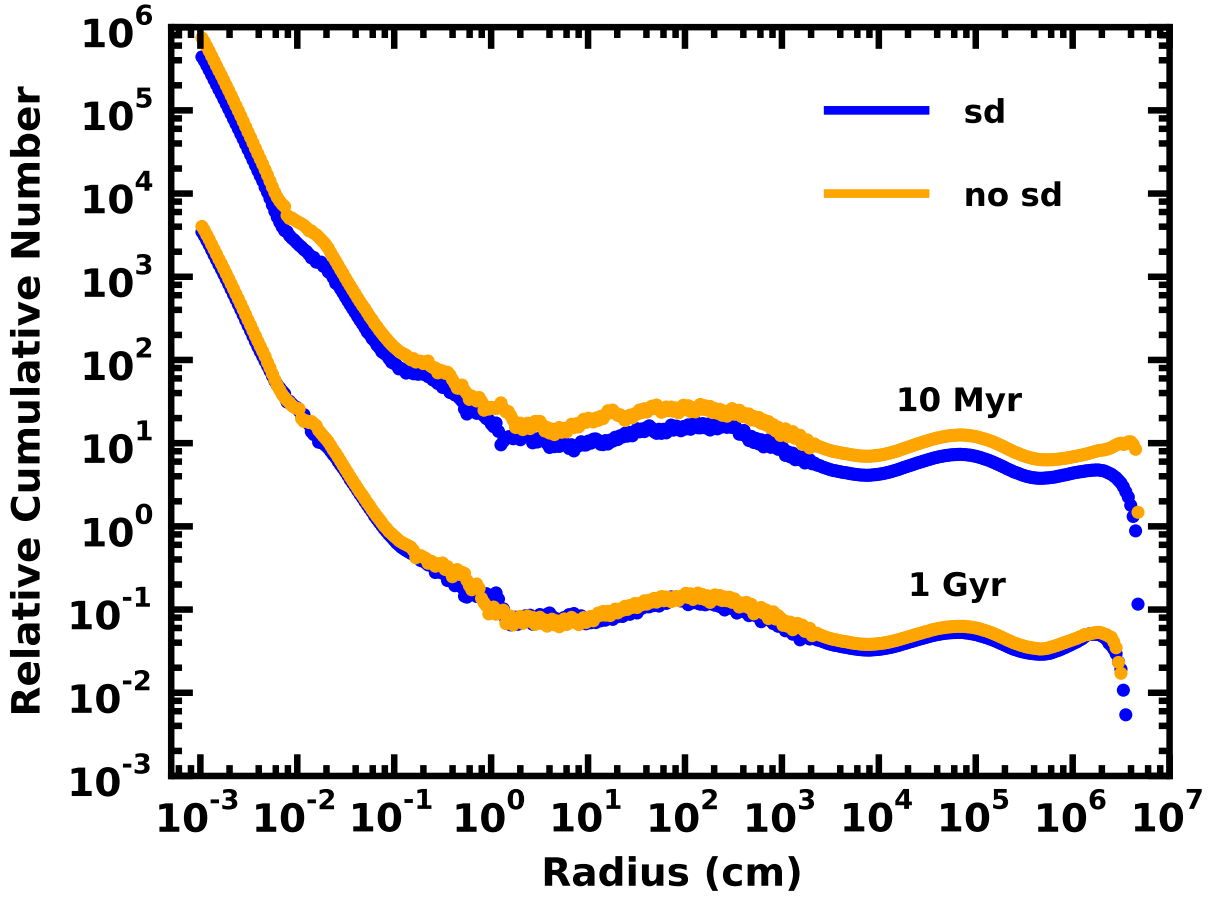

Fig. 16.— Comparison of model relative size distributions for calculations starting from an initial power law size distribution of particles ('sd') and a mono-disperse set of particles ('no sd') at 10 Myr (upper set of curves) and at 1 Gyr (lower set of curves). Aside from minor deviations at the largest sizes, the two sets of calculations yield identical size distributions.

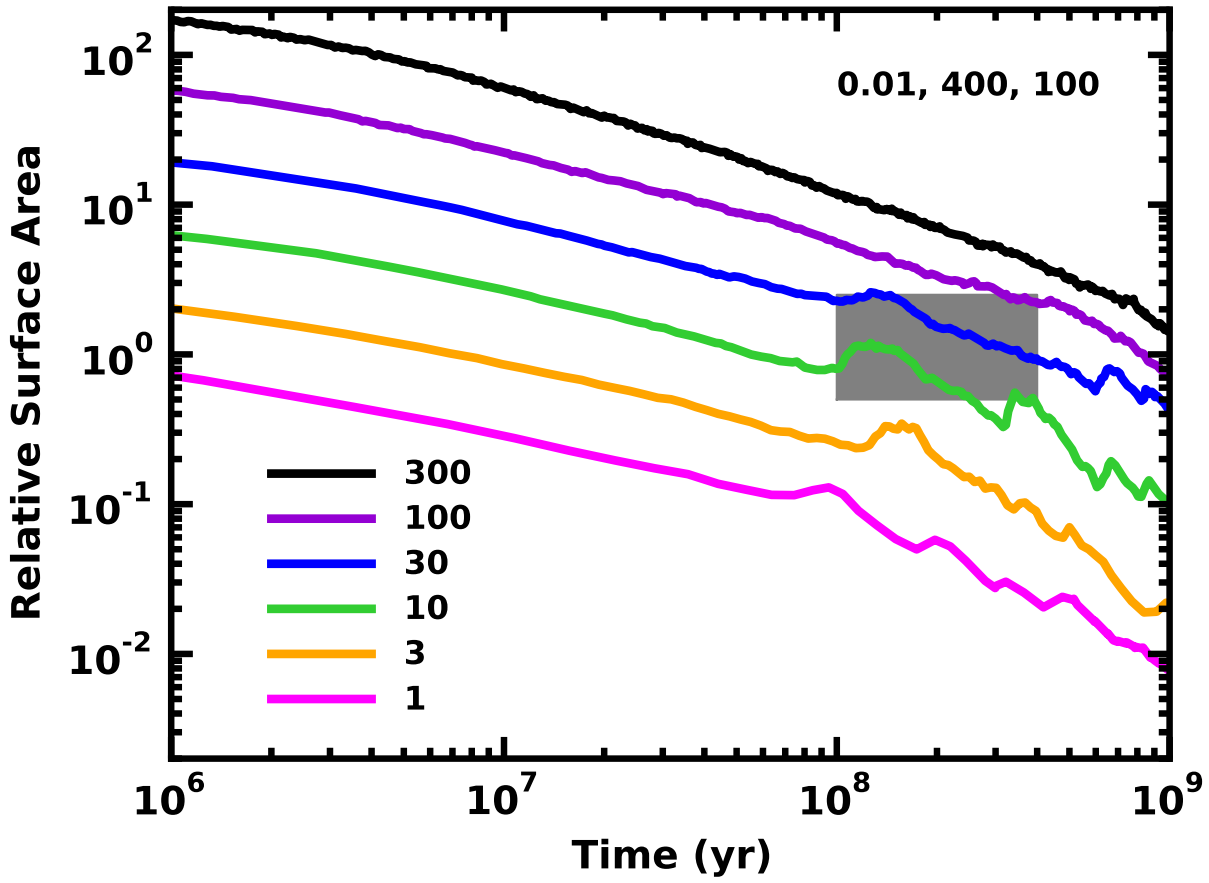

Fig. 17.— Time evolution of the relative surface area derived from coagulation calculations of circumplanetary clouds of particles with the nominal fragmentation parameters, $m_{l,0}$ = 0.2, and b_l = 0.0. The legend in the upper right indicates the initial x_d, r_{max} (in km), and r_{min} (in μm). The legend in the lower left indicates the mass of the central planet. When the largest object does not grow (M_p = 100, 300 $M_\oplus$), the relative surface area declines smoothly with time. At late times in simulations with growing satellites, the surface area fluctuates about a gradual decline.

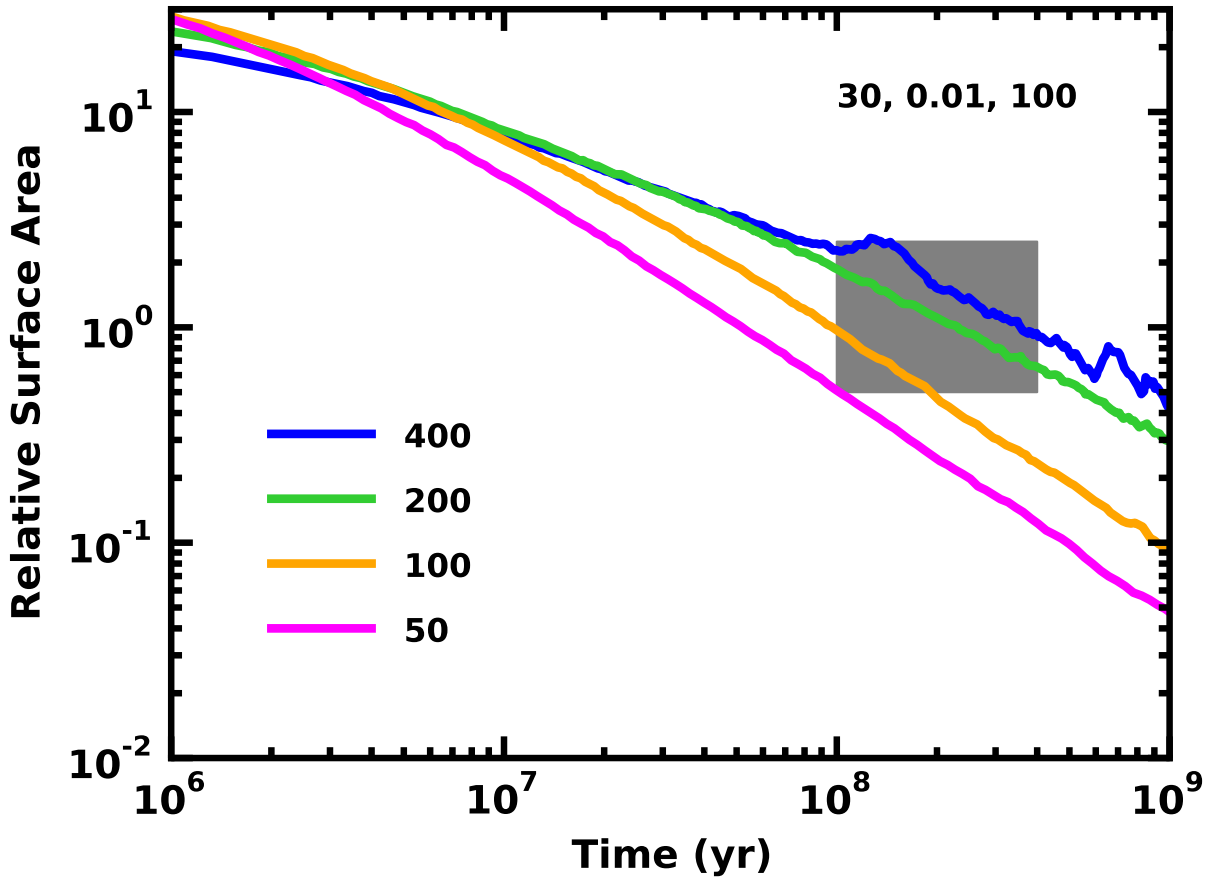

Fig. 18.— As in Fig. 17 for the M_p, x_d, and r_{min} indicated in the upper right corner for the range of r_{max} (in km) indicated in the lower left corner. The slow decline of the relative surface area is smoother for smaller r_{max}.

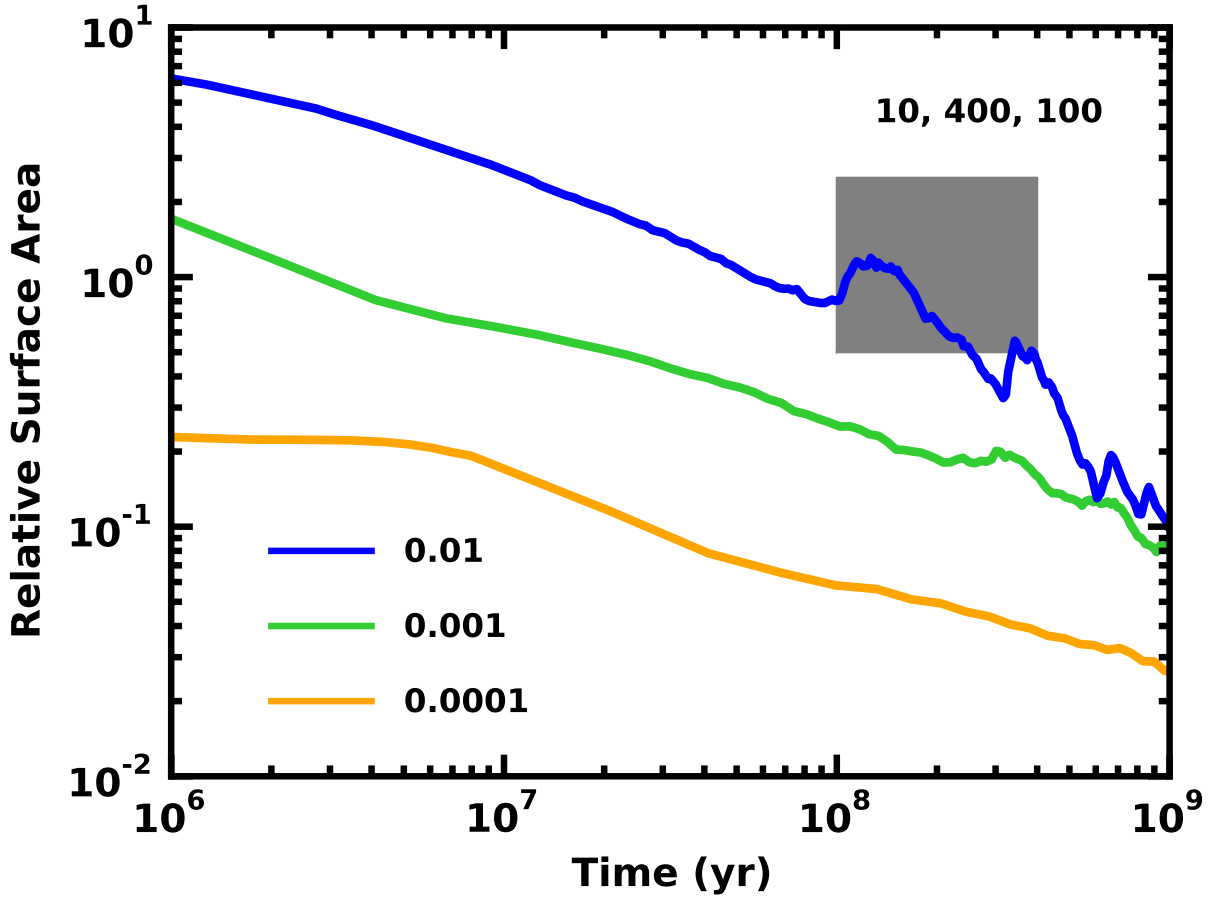

Fig. 19.— As in Fig. 17 for the M_p, r_{max}, and r_{min} indicated in the upper right corner for various x_d as indicated in the lower left corner. Lower mass clouds have smaller relative surface areas.

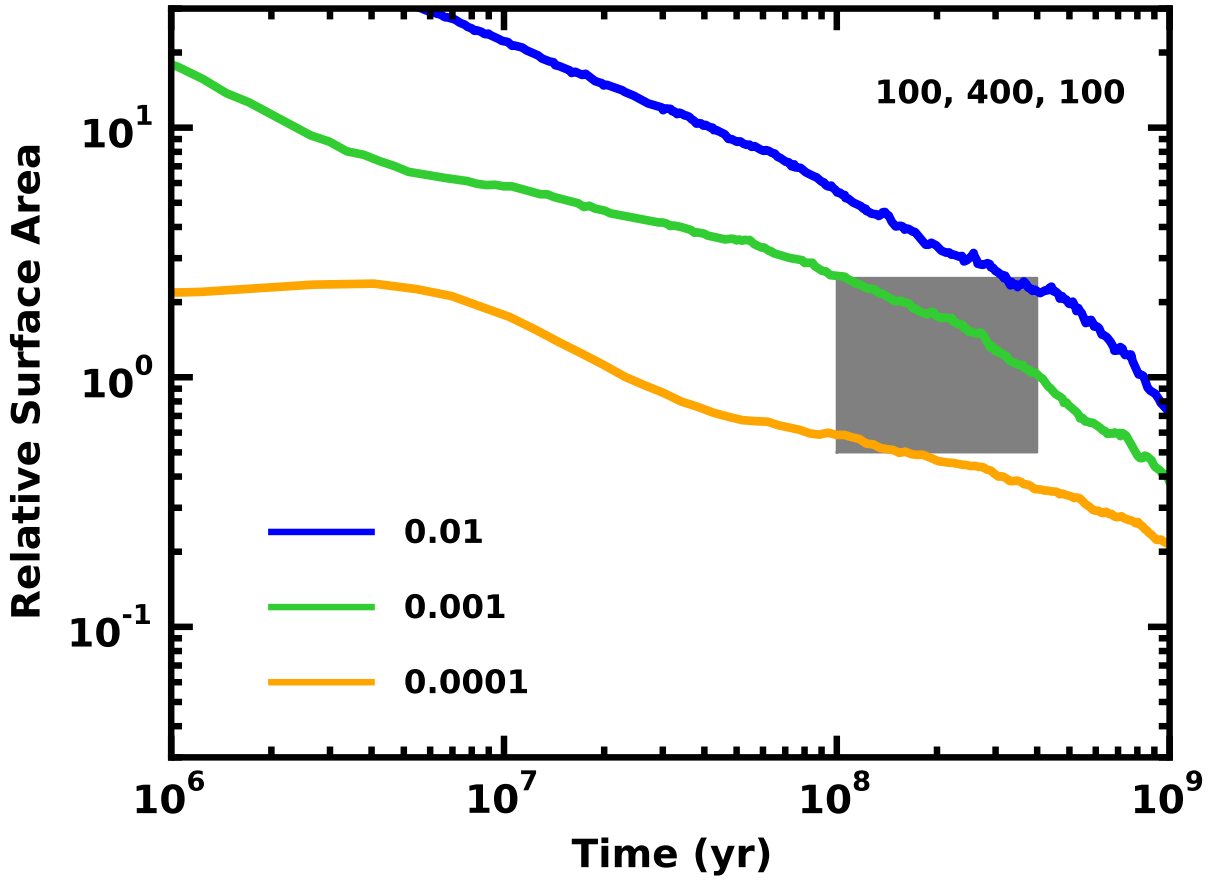

Fig. 20.— As in Fig. 19 for $M_p = 100\ M_\oplus$.

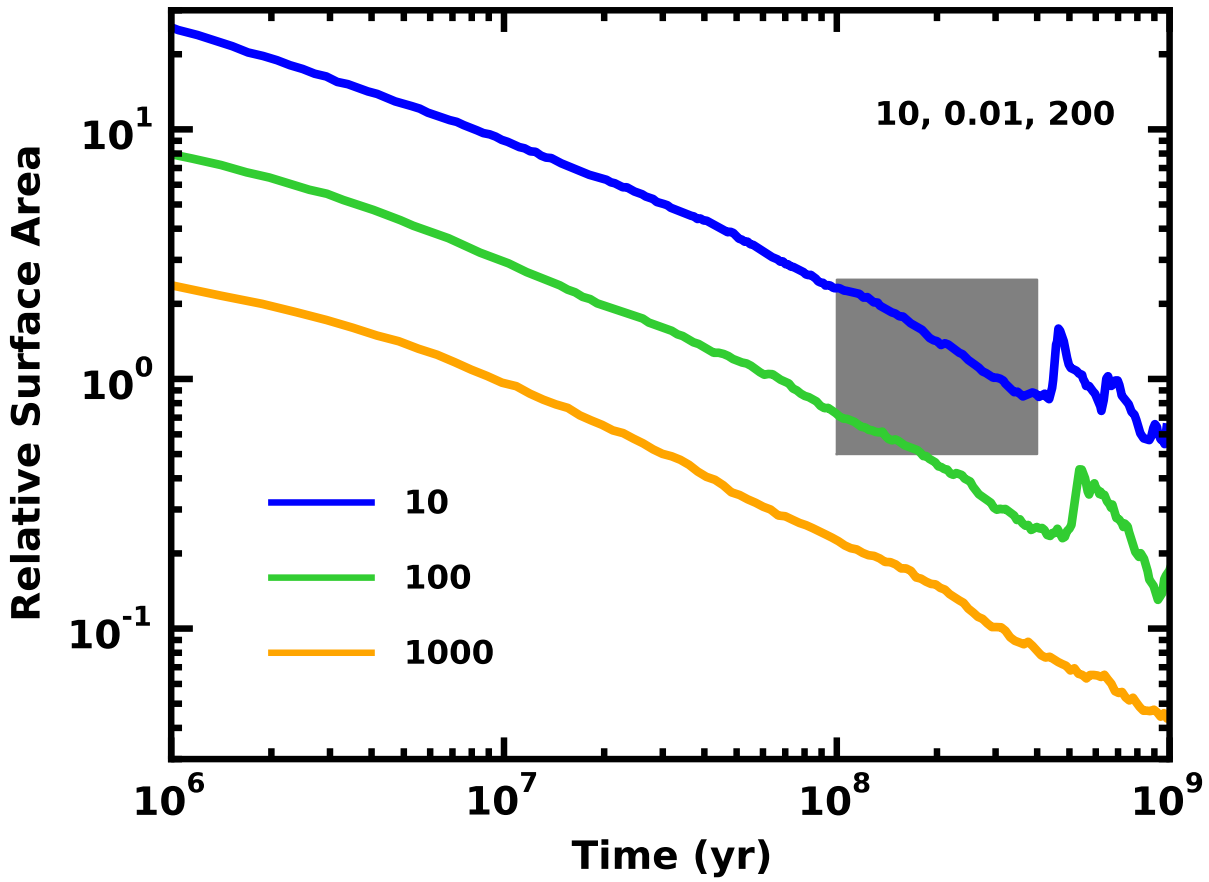

Fig. 21.— As in Fig. 17 for the M_p, x_d, and r_{max} summarized in the upper right corner for the r_{min} listed in the lower left corner. Calculations with smaller r_{min} have more small particles and larger relative surface area.

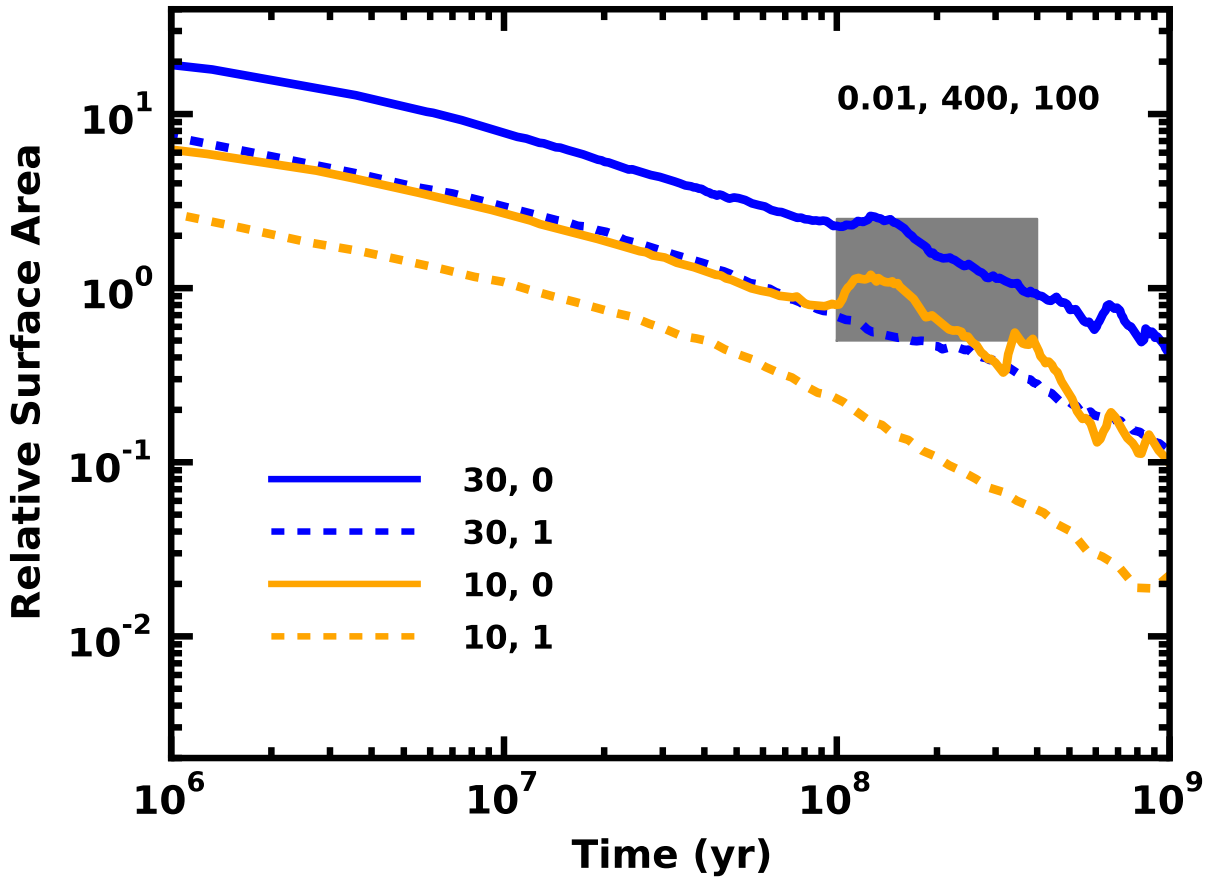

Fig. 22.— As in Fig. 21 for the x_d, r_{max}, and r_{min} listed in the upper right corner and various M_p and b_L as listed in the lower right corner. Calculations with $b_L = 1$ have smaller relative surface area than those with $b_L = 0$.

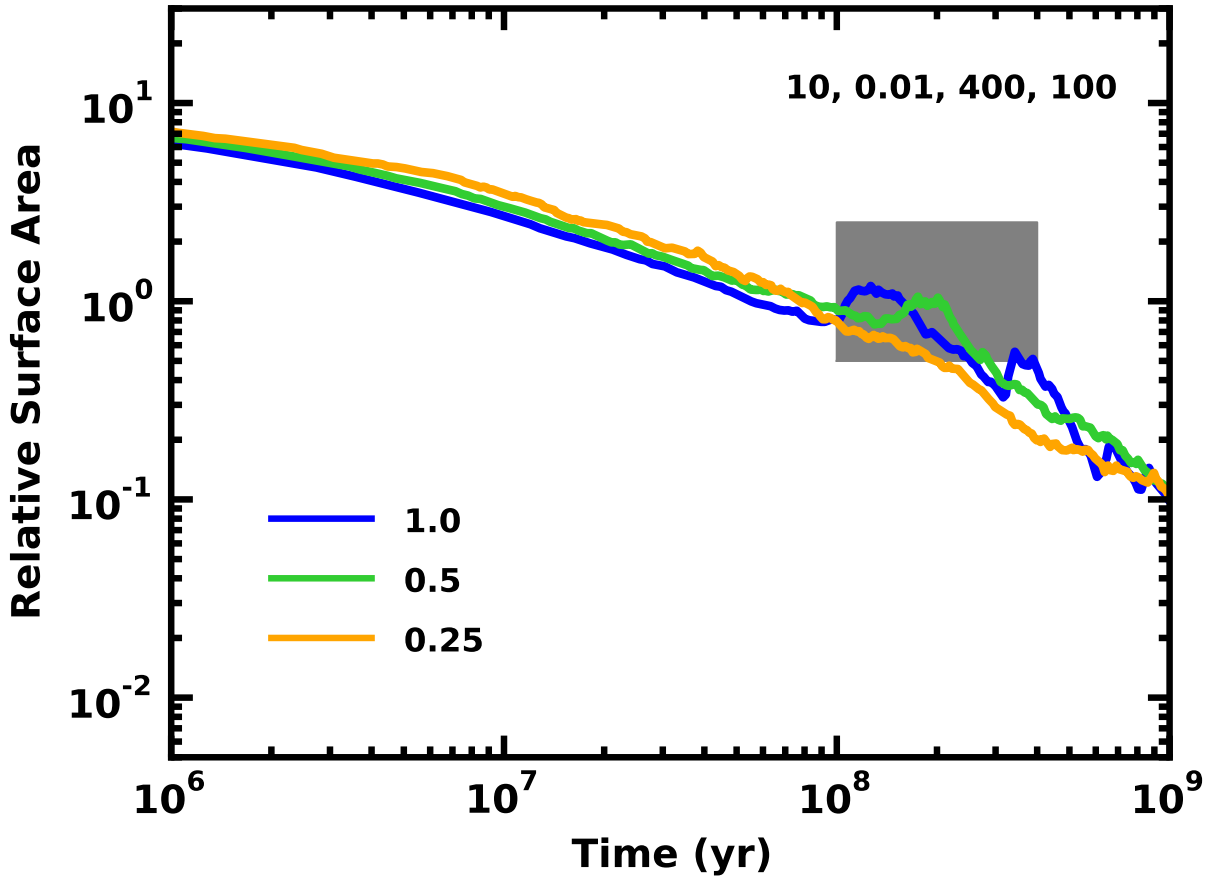

Fig. 23.— As in Fig. 17 for the M_p, x_d, r_{max}, and r_{min} listed in the upper right corner and various $Q_D^\star$. The legend in the lower left corner indicates the value of $Q_D^\star$ relative to the nominal value.

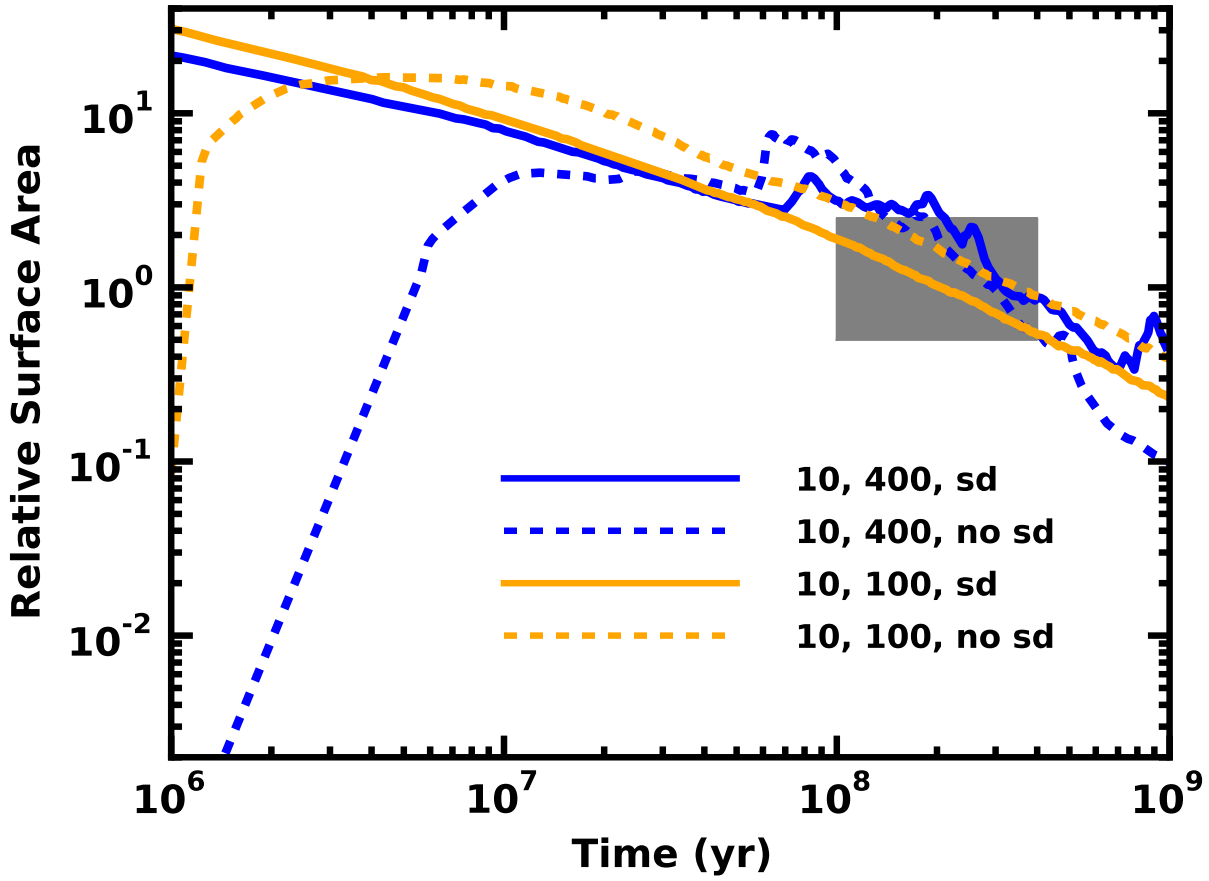

Fig. 24.— As in Fig. 17 for calculations with (sd) and without (no sd) an initial power law size distribution of solid particles. The legend indicates M_p, r_{max}, and the initial size distribution for each model curve.

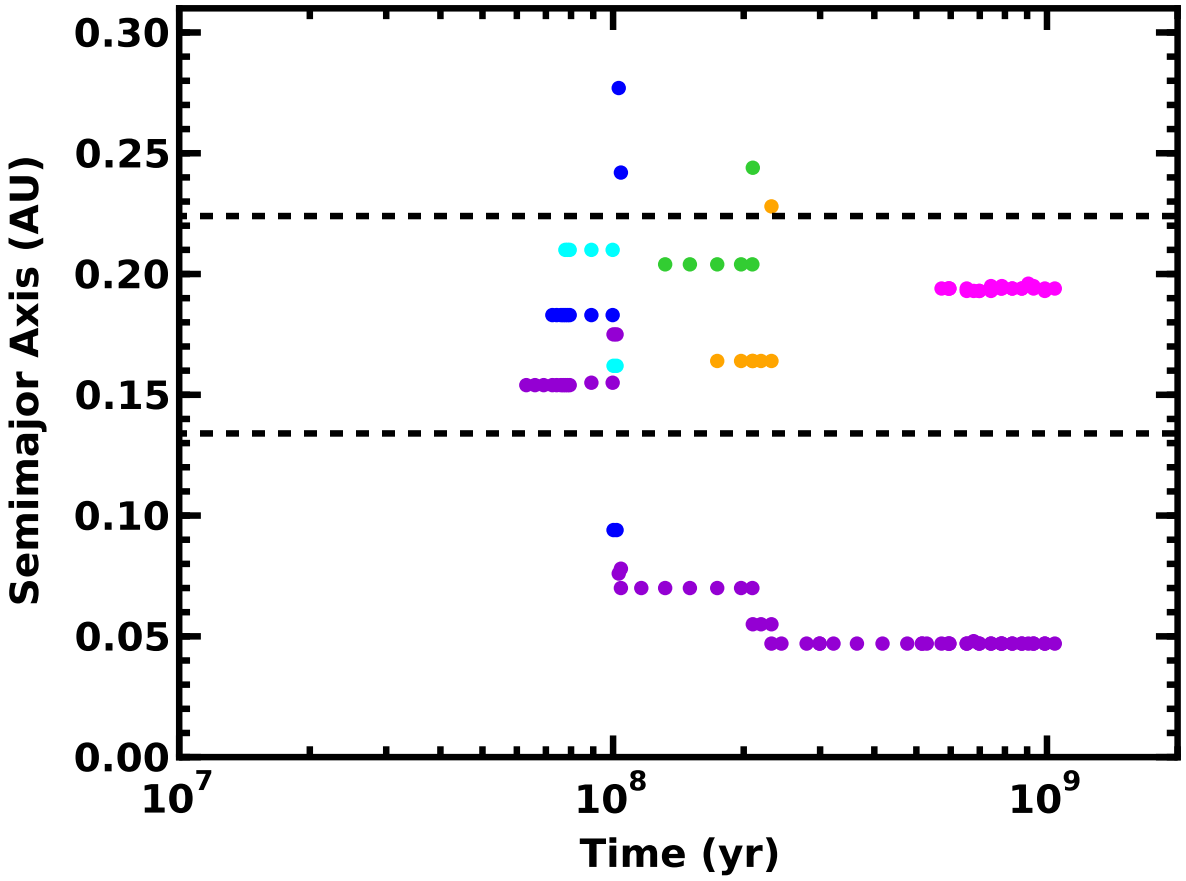

Fig. 25.— Evolution of semimajor axis for massive (n-body) satellites orbiting a 1 $M_\oplus$ planet. The dashed lines indicate the extent of the satellite swarm within the coagulation code. Tracks for individual n-bodies are coded by color. At 70–100 Myr, the coagulation code promotes three objects into the n-body code. After several minor encounters, strong interactions lead to a single object on an $e = 0.6$ orbit at smaller a and the ejection of two n-bodies. Somewhat later ($\sim$ 200 Myr), interactions between a second pair of n-bodies leads to a second set of ejections and a modest contraction of the orbit of the original n-body. At late times, promotion of a sixth n-body leaves the system with a single relatively low mass object on a fairly circular orbit at 0.20 AU and a more massive satellite on an eccentric orbit at 0.05 AU.

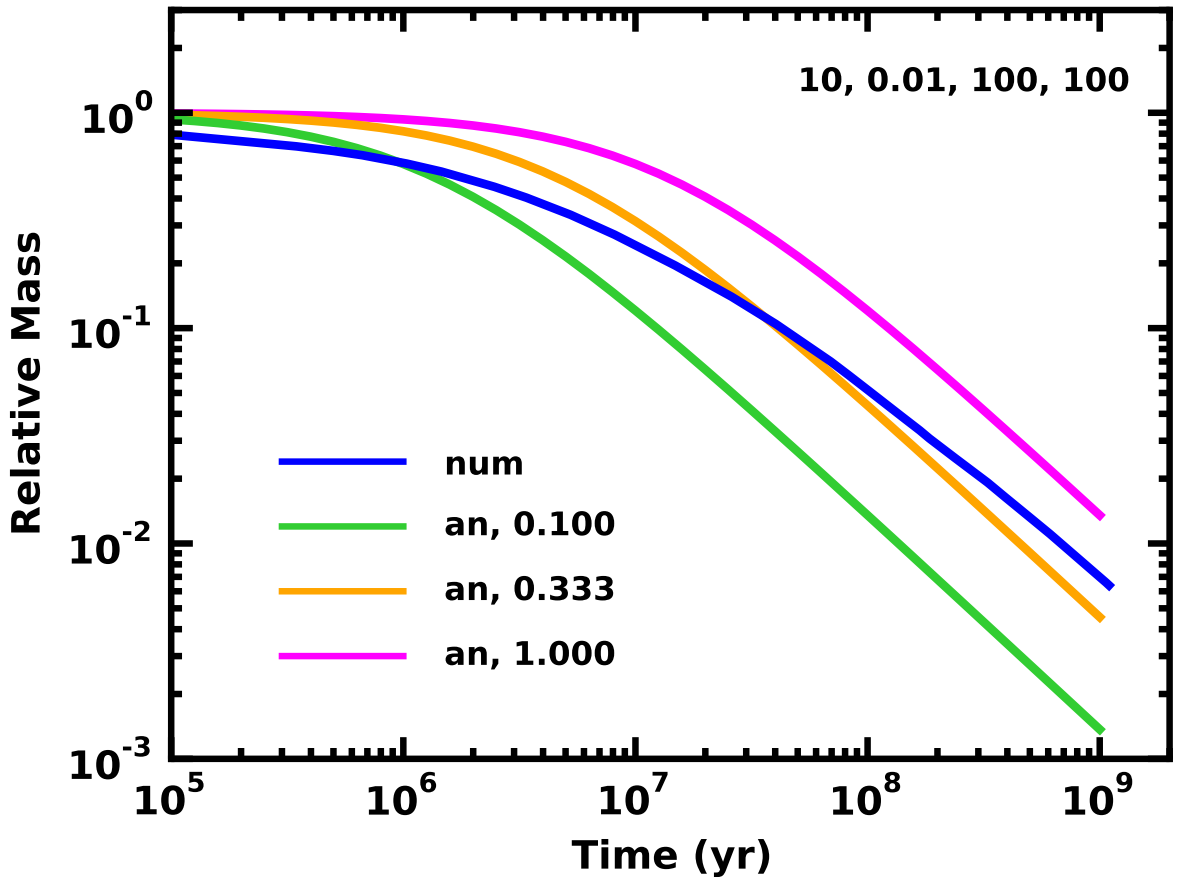

Fig. 26.— Evolution of the mass of satellite swarms relative to their initial mass for the baseline numerical model ('num') and analytic models ('an') with three values of α as listed in the legend. As indicated in the upper right corner, the baseline model has $M_p = 10\ M_\oplus$, $x_d = 0.01$, $r_{max} = 100$ km, and $r_{min} = 100\ \mu$m. The evolution of an analytic model with $\alpha \approx 1$ provides a reasonable match to the numerical model.

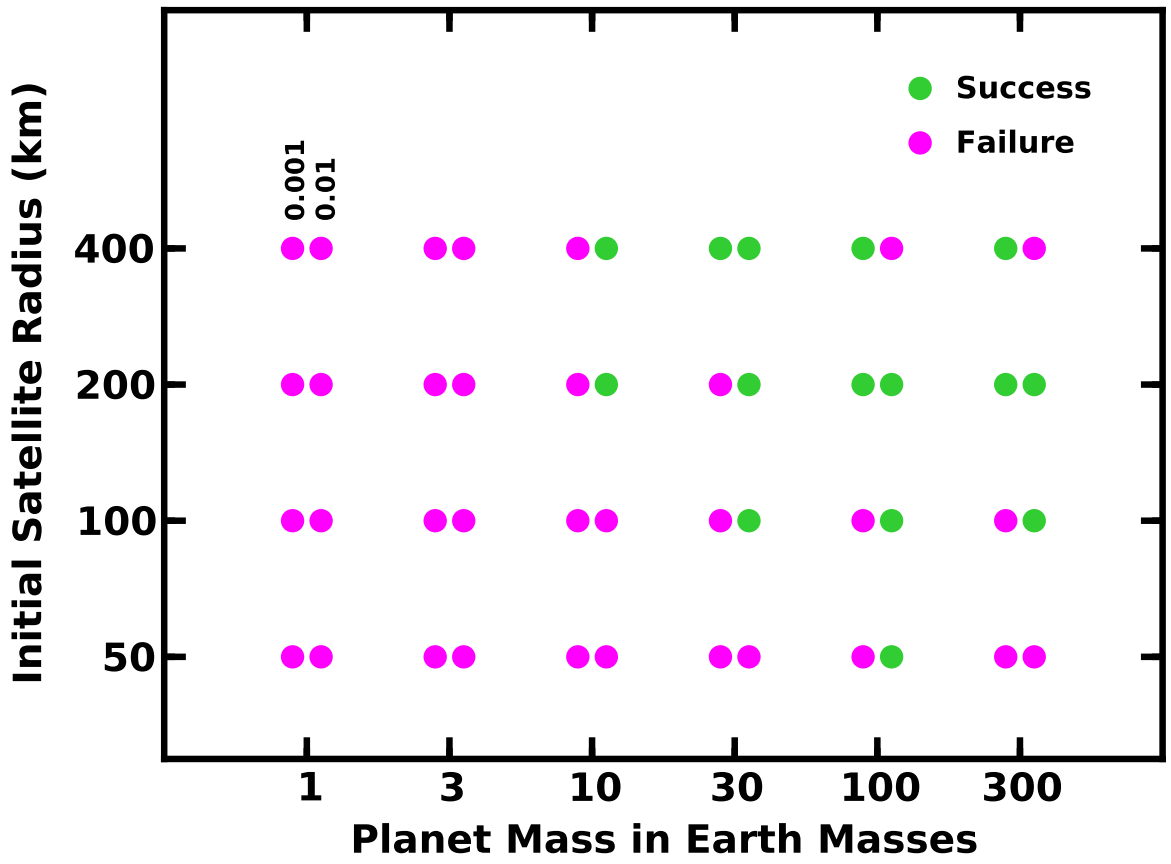

Fig. 27.— Grid of outcomes for satellites swarms in Fomalhaut b. For initial relative cloud mass $x_d = 0.001$ and 0.01 (as indicated above the first column of points), green (red) points indicate models which match (do not match) the observed surface area of Fomalhaut b at 100–400 Myr.

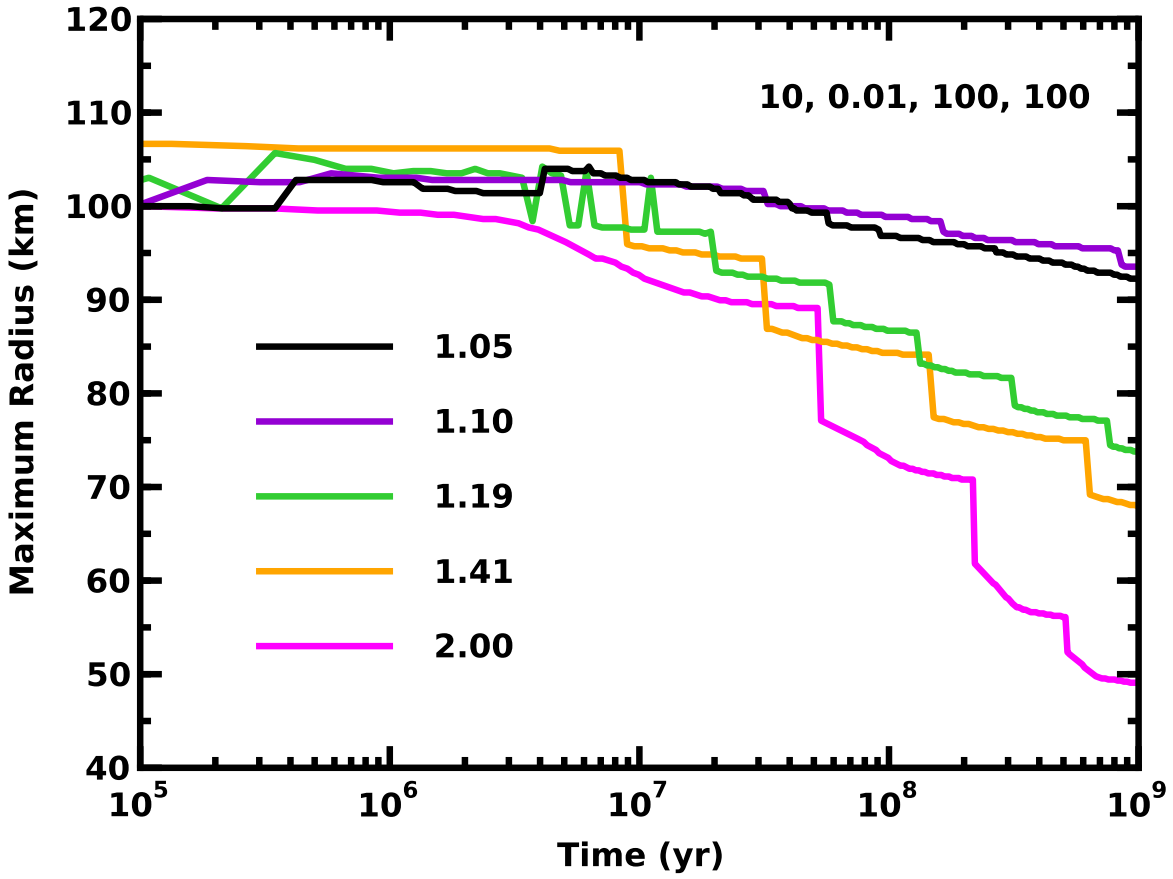

Fig. 28.— Time evolution of the radius of the largest object for different mass spacing factors δ as listed in the legend. The satellite swarm – $x_d = 0.01$, $r_{max} = 100$ km, $r_{min} = 100$ μm – orbits a planet with $M_p = 10$ $M_\oplus$.

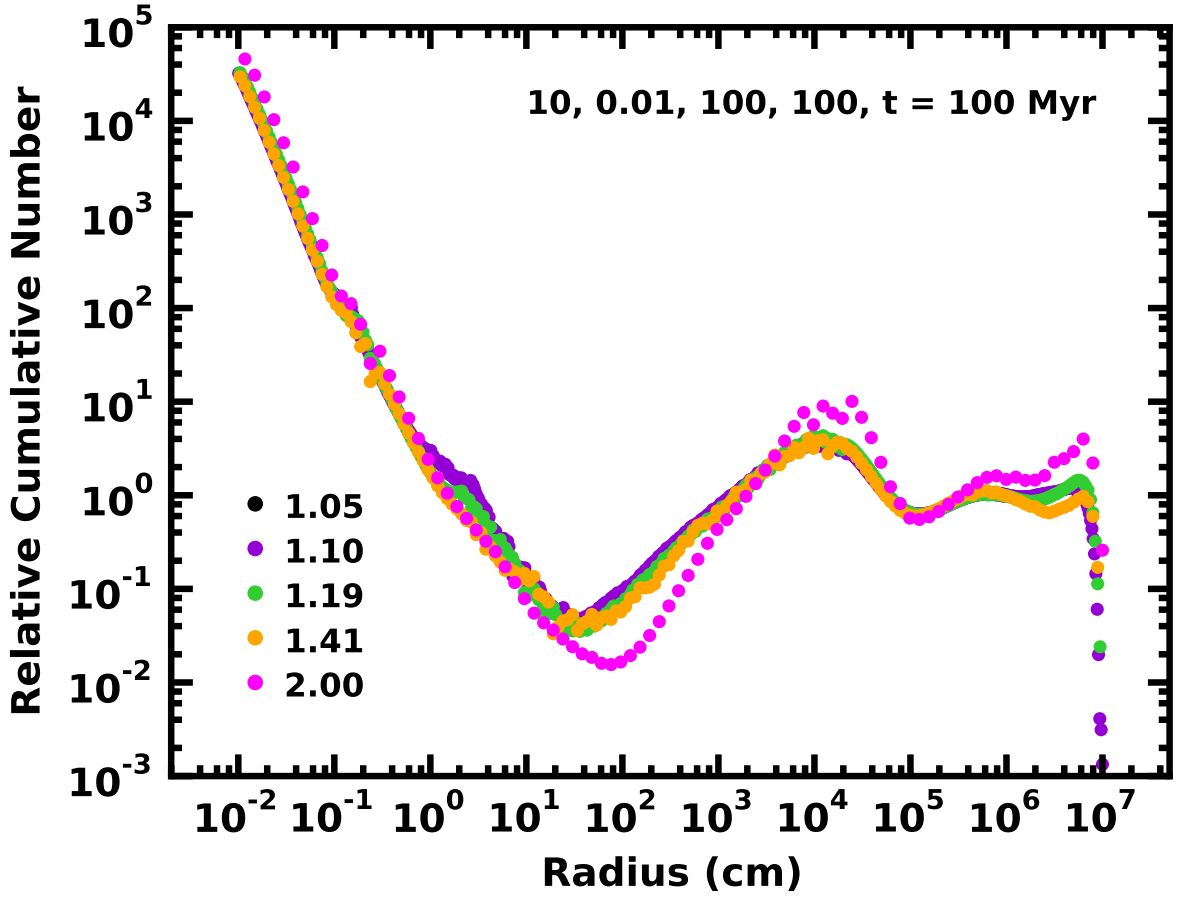

Fig. 29.— Snapshot of the size distribution for the baseline models in Fig. 28 at 100 Myr. Solutions for $\delta = 2$ have more waviness than those with smaller δ. Solutions for $\delta = 1.05$–1.4 are nearly identical.

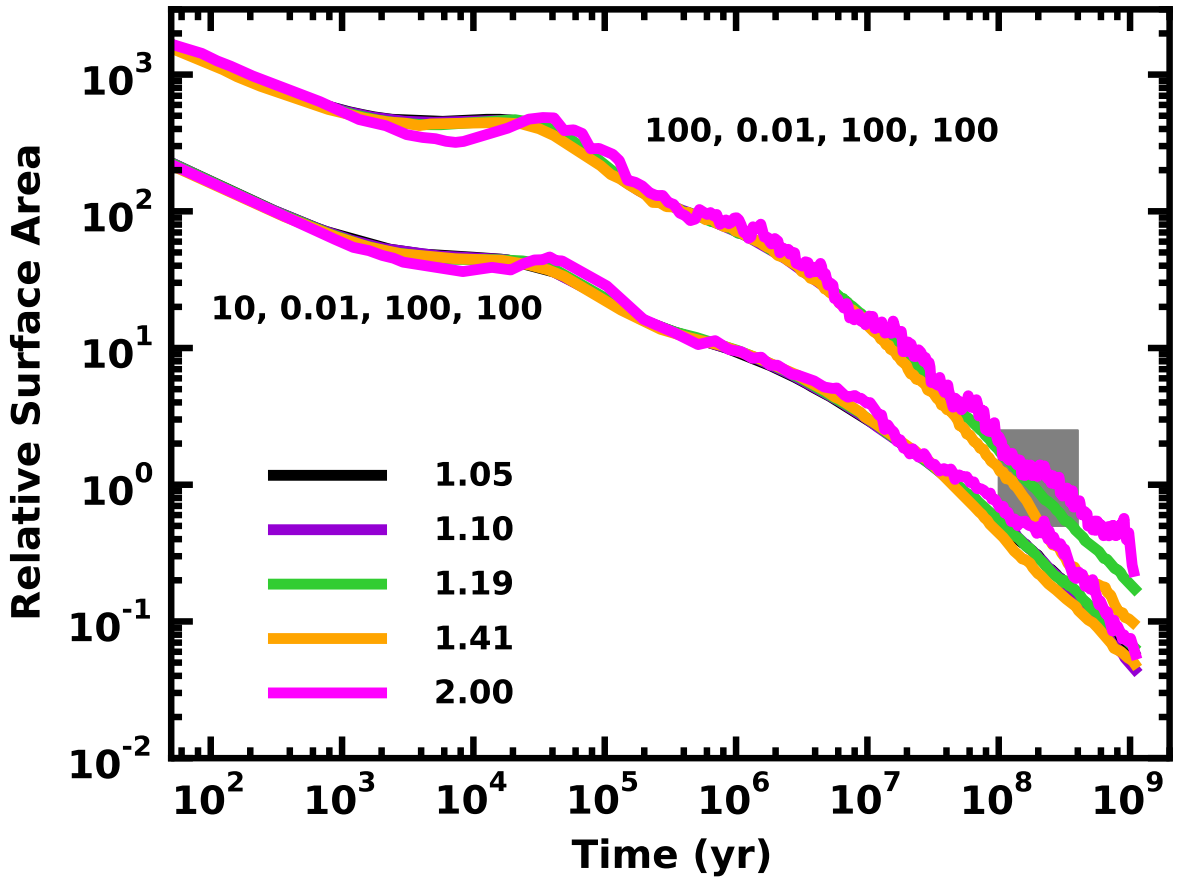

Fig. 30.— Time evolution of the cross-sectional area for two baseline models as a function of δ (as listed in the legend). For the upper (lower) set of curves, $M_p = 100\ M_\oplus$ ($10\ M_\oplus$); in both, $x_d = 0.01$, $r_{max} = 100$ km, and $r_{min} = 100\ \mu$m. The surface area is not a strong function of δ.